

Measurement of the Ratio of the Neutron to Proton Structure Functions, and the Three-Nucleon
EMC Effect in Deep Inelastic Electron Scattering Off Tritium and Helium-3 Mirror Nuclei

Hanjie Liu

Submitted in partial fulfillment of the
requirements for the degree of
Doctor of Philosophy
in the Graduate School of Arts and Sciences

COLUMBIA UNIVERSITY

2020

© 2020

Hanjie Liu

All Rights Reserved

Abstract

Measurement of the Ratio of the Neutron to Proton Structure Functions, and the Three-Nucleon EMC Effect in Deep Inelastic Electron Scattering Off Tritium and Helium-3 Mirror Nuclei

Hanjie Liu

The proton and neutron structure functions F_2^p and F_2^n , respectively are fundamental to understanding many studies in nuclear physics. They provide important information about quark distributions. For example, the ratio F_2^n/F_2^p is one of the best measurements to find the ratio of d quark over u quark distribution inside the proton. While the calculations of structure functions and quark distributions are non-perturbative, they can be determined by the parameterization of experimental data. The understanding of F_2^n/F_2^p and d/u as $x \rightarrow 1$ has a large influence on global fits and parameterization, and can be used to distinguish the non-perturbative models which give different predictions. However, F_2^n/F_2^p measured using deuteron and hydrogen targets has large nuclear uncertainties at large x , because the nuclear effects in the deuteron become significant at large x . The MARATHON experiment, which ran in spring 2018 using the upgraded 11 GeV Jefferson Lab electron beam, employs a novel method. It performed deep inelastic scattering off tritium and helium-3 mirror nuclei to measure F_2^n/F_2^p over the range $x = 0.17$ to $x = 0.82$. Since tritium and helium-3 are mirror nuclei, theoretical uncertainties largely cancel out in the ratio. The extracted F_2^n/F_2^p has much smaller uncertainties compared with previous experiments at large x . The MARATHON experiment also provided results on the EMC effect for tritium and helium-3 nuclei. The results are considered essential for understanding the EMC effect. This thesis describes the MARATHON experiment, and presents results for F_2^n/F_2^p , and the EMC effect for tritium and helium-3.

Table of Contents

List of Tables	v
List of Figures	vi
Acknowledgements	xi
Chapter 1: Introduction	1
1.1 Deep inelastic scattering	2
1.1.1 Kinematics	2
1.1.2 Bjorken scaling	4
1.2 Quark-parton model	5
1.3 Running coupling and asymptotic freedom	7
1.4 QCD improved parton model	9
1.4.1 DGLAP evolution	12
1.4.2 High twist and target mass correction	13
Chapter 2: F_2^n/F_2^p and EMC effect	15
2.1 F_2^n/F_2^p and d/u	15
2.1.1 d/u at large x	16
2.1.2 F_2^n from deuteron data	18

2.2	The EMC effect	22
2.2.1	Theoretical models of the EMC effect	22
2.3	The MARATHON experiment	29
Chapter 3: Experimental Setup		31
3.1	Introduction	31
3.2	Accelerator	31
3.3	Hall A overview	35
3.4	Hall A arc and beam line	35
3.4.1	Beam energy measurement	36
3.4.2	Beam Current Monitor	37
3.4.3	Raster and Beam Position Monitor	38
3.5	Target	40
3.6	Hall A High Resolution Spectrometers	42
3.6.1	Scattering angle and momentum measurement	43
3.6.2	Coordinate systems and optics matrix	45
3.6.3	Optics calibrations	49
3.7	Detector package	50
3.7.1	Vertical Drift Chamber (VDC)	51
3.7.2	Scintillators	53
3.7.3	Gas Cherenkov Detector	54
3.7.4	Shower detectors	55
3.8	Data acquisition	58

3.8.1	Triggers	59
Chapter 4:	Data Analysis	61
4.1	Introduction	61
4.2	DAQ and detector efficiencies	63
4.2.1	DAQ dead time	63
4.2.2	Trigger efficiency	64
4.2.3	VDC efficiency	65
4.2.4	PID efficiency	66
4.2.5	Acceptance	67
4.3	Boiling effect correction	69
4.4	Background subtraction	71
4.4.1	Pion contamination	72
4.4.2	End cap contamination	73
4.4.3	Charge symmetric background	75
4.4.4	Tritium decay	76
4.5	Radiative corrections	78
4.5.1	Cross section model	82
4.6	Coulomb correction	84
4.7	Bin centering and combination of kinematics	84
4.8	Experimental uncertainties	86
4.9	Cross section ratios	89
Chapter 5:	Results	96

5.1	F_2^n/F_2^p results	96
5.1.1	F_2^n/F_2^p extraction	96
5.1.2	Normalization	100
5.1.3	F_2^n/F_2^p results	102
5.2	EMC effect	104
5.2.1	Isoscalar correction	104
5.2.2	^3He EMC effect	105
5.2.3	^3H EMC effect	107
5.3	Conclusions	109
Chapter 6: Future project and experiments		110
6.1	An alternative data analysis method	110
6.2	The BONUS12 experiment	112
6.3	d/u from proton PVDIS	112
References		115
Appendix A: Cross Section Model Comparison		120
Appendix B: Cross Section Ratio Data		123
Appendix C: F_2^n/F_2^p and EMC results		127

List of Tables

Table 3.1	The kinematics of the MARATHON experiment	33
Table 3.2	A list of targets used in MARATHON	41
Table 4.1	Systematic uncertainties on the cross section ratios	89
Table 5.1	The normalization on nuclei structure function ratios	102
Table B.1	$\sigma(^2\text{H})/\sigma(^1\text{H})$ results	123
Table B.2	$\sigma(^3\text{He})/\sigma(^2\text{H})$ results	124
Table B.3	$\sigma(^3\text{H})/\sigma(^2\text{H})$ results	125
Table B.4	$\sigma(^3\text{H})/\sigma(^3\text{He})$ results	126
Table C.1	F_2^n/F_2^p results. The 2.4% normalization on $\sigma(^3\text{He})$ is applied.	128
Table C.2	The EMC ratio for ^3He results with isoscalar correction. The 2.4% normalization on $\sigma(^3\text{He})$ is applied.	129
Table C.3	The EMC ratio for ^3H results with isoscalar correction. The 1.12% normalization uncertainty of $\sigma(^3\text{H})/\sigma(^2\text{H})$ is not included.	130

List of Figures

Figure 1.1	Electron scattering	3
Figure 1.2	The spectra of electron-nucleon scattering and electron-nucleus scattering	4
Figure 1.3	An early observation of scaling: νW_2 for the proton as a function of q^2 for $W > 2$ GeV, at $\omega = 4$	5
Figure 1.4	Loop corrections to the gluon propagator	8
Figure 1.5	Feynman diagrams for gluon radiation from quarks in DIS	10
Figure 1.6	The proton F_2^p at two Q^2 values showing the Bjorken scaling violation	11
Figure 1.7	Feynman diagrams for boson-gluon fusion in DIS	12
Figure 2.1	The ratio F_2^n/F_2^p extracted from deuteron and proton data using different models	19
Figure 2.2	The ratio $F_2(Fe)/F_2^d$ averaged over Q^2 as a function of x	20
Figure 2.3	The F_2^n/F_2^p ratio together with the uncertainties induced by nuclear effects models	21
Figure 2.4	The typical EMC effect of a nucleus	23
Figure 2.5	Comparison between EMC effect data and the pion enhancement models	25
Figure 2.6	Comparison between EMC effect data and the quark cluster model	26
Figure 2.7	Comparison between EMC effect data and the dynamic scaling model	28
Figure 2.8	The short range correlations and the EMC effect.	29

Figure 3.1	W^2 vs. x distribution in the MARATHON experiment	32
Figure 3.2	Q^2 vs. x distribution in the MARATHON experiment	32
Figure 3.3	CEBAF 12 GeV upgrade schematic	34
Figure 3.4	CEBAF overview	34
Figure 3.5	Hall A configuration during the MARATHON experiment	35
Figure 3.6	Hall A arc section	37
Figure 3.7	Beam Current Monitors	39
Figure 3.8	Rastered beam y vs. beam x	39
Figure 3.9	Superharp design	40
Figure 3.10	Target ladder	41
Figure 3.11	Tritium target cell design	42
Figure 3.12	The layout of a HRS (side view)(the numbers in the plot are out of date)	43
Figure 3.13	Main design characteristics of the HRS.	44
Figure 3.14	Hall coordinate system (top view)	46
Figure 3.15	Target coordinate system (top view)	46
Figure 3.16	Detector coordinate system	47
Figure 3.17	Transport coordinate system (side view)	48
Figure 3.18	Focal plane (rotated) coordinate system (side view)	48
Figure 3.19	The sieve slit collimator	50
Figure 3.20	Detector package in MARATHON	51
Figure 3.21	Schematic layout of VDCs	52
Figure 3.22	A nominal track in a wire plane	53
Figure 3.23	A single wire drift-time spectrum in common-stop mode	54

Figure 3.24	Scintillators	55
Figure 3.25	Front view and side view of Gas Cherenkov Detector	56
Figure 3.26	The configurations of shower detectors in LHRS and RHRS	56
Figure 3.27	LHRS trigger setup	60
Figure 3.28	RHRS trigger setup	60
Figure 4.1	T2(T5) dead time correction factor of each target for each kinematic setting	64
Figure 4.2	T1/T4 trigger efficiency	65
Figure 4.3	Detection efficiency of LHRS U1 wires	66
Figure 4.4	VDC efficiency for LHRS and RHRS at kin0, kin1 and kin2	67
Figure 4.5	Cherenkov sum distribution and E/P distribution	68
Figure 4.6	The $^2\text{H}/^1\text{H}$ acceptance function ratio	69
Figure 4.7	The ^3H density change as a function of current	70
Figure 4.8	The boiling correction factor ratio for various target combinations	71
Figure 4.9	The E/P distribution	72
Figure 4.10	The π/e ratio	73
Figure 4.11	The vertex z distribution at target	74
Figure 4.12	End cap contamination correction factor on ratios	75
Figure 4.13	E/P distribution of positrons with nominal cuts applied	76
Figure 4.14	Charge symmetric background correction factor	77
Figure 4.15	^3He contamination in ^3H target during the MARATHON experiment	79
Figure 4.16	Feynman diagrams in internal radiative correction	80
Figure 4.17	Schematic representation of the processes that contribute to the DIS radiative cross section	81

Figure 4.18 Radiative correction factors applied to the cross section ratios as a function of x	82
Figure 4.19 ^3H Born cross section σ_{model}^{born} and radiative cross section σ_{model}^{rad} from model with $Q^2 = 14x$	83
Figure 4.20 $\sigma(^2\text{H})/\sigma(^1\text{H})$ for each kinematic setting	90
Figure 4.21 $\sigma(^3\text{He})/\sigma(^2\text{H})$ for each kinematic setting	90
Figure 4.22 $\sigma(^3\text{H})/\sigma(^2\text{H})$ for each kinematic setting	91
Figure 4.23 $\sigma(^3\text{H})/\sigma(^3\text{He})$ for each kinematic setting	91
Figure 4.24 $\sigma(^2\text{H})/\sigma(^1\text{H})$ result as a function of x	92
Figure 4.25 $\sigma(^3\text{He})/\sigma(^2\text{H})$ as a function of x	93
Figure 4.26 $\sigma(^3\text{H})/\sigma(^2\text{H})$ as a function of x	94
Figure 4.27 $\sigma(^3\text{H})/\sigma(^3\text{He})$ as a function of x	95
Figure 5.1 The EMC-type ratios for ^2H , ^3He and ^3H from the KP model	97
Figure 5.2 F_2^n/F_2^p extracted from $F_2^{^3\text{H}}/F_2^{^3\text{He}}$ and $F_2^{^2\text{H}}/F_2^{^1\text{H}}$	98
Figure 5.3 The ratios between EMC-type ratios from KP model	99
Figure 5.4 F_2^n/F_2^p extracted from $F_2^{^3\text{H}}/F_2^{^3\text{He}}$, $F_2^{^2\text{H}}/F_2^{^1\text{H}}$, $F_2^{^3\text{H}}/F_2^{^2\text{H}}$ and $F_2^{^3\text{He}}/F_2^{^2\text{H}}$ at low x	101
Figure 5.5 F_2^n/F_2^p after normalizing the nuclei structure function ratios	102
Figure 5.6 F_2^n/F_2^p extracted from renormalized $^3\text{H}/^3\text{He}$ using CJ model	103
Figure 5.7 F_2^n/F_2^p result after normalization	104
Figure 5.8 Comparison between the F_2^n/F_2^p from the MARATHON experiment and the SLAC experiments	105
Figure 5.9 ^3He EMC ratio result	106
Figure 5.10 ^3H EMC ratio result	107

Figure 5.11 Comparison between ${}^3\text{H}$ EMC ratio and ${}^3\text{He}$ EMC ratio. The 2.4% normalization on $\sigma({}^3\text{He})$ is applied.	108
Figure 6.1 Comparison on (a) Super-ratio \mathcal{R} , (b) the ratio $F_2^{3\text{He}}/F_2^{3\text{H}}$	111
Figure 6.2 The BONUS12 projected F_2^n/F_2^p results	113
Figure 6.3 Projected d/u results from the MARATHON experiment, the BONUS12 experiment and the SoLID PVDIS experiment.	114
Figure A.1 F_2 Structure functions from different models	120
Figure A.2 F_2^n/F_2^p from different models with $Q^2 = 14x \text{ GeV}^2$	121
Figure A.3 EMC ratio from different models	122

Acknowledgements

When one thing is almost completed, you will somehow feel the result seems to come naturally, and forget how difficult it was during the process. But the fulfillment of accomplishing a science project and the confidence gotten from all the work done are the most valued things I got from graduate school. Without those nice people around me, I wouldn't be able to reach here. My advisor, Prof. Emlyn Hughes, is very professional and interesting. Besides his expertise in particle and nuclear physics, he's very easy to talk with, like a friend. I would like to thank him for encouraging me to finish my PhD quickly and move on to more challenging projects. While I spent two thirds of my time in Jefferson Lab, i'm especially thankful to the staff in Columbia who helped me deal with all kinds of things so I can focus on my research in Newport News. Bob Michaels, Alex Camsonne and Jianping Chen are the people I firstly worked with in JLab. I learned a lot about DAQ from Bob and Alex, and their patient instruction makes me enjoy working on DAQ. The long talks with JP are always encouraging and helped me clear my mind. Douglas Higinbotham and Dave Meekins put lots of their effort in the tritium experiments and they always care about the students. Makis Petratos and Mina Katramatou were always there in the counting house monitoring the data quality and brought cakes for us. Javier Gomez paid a lot of attention on the MARATHON experiment running. I always asked him when I had questions on data analysis. He is very patient and helpful. The postdocs, Evan McClellan, Florian Hauenstein and Marco Carmignotto, led the preparation for the experiment running and the data analysis. With their effort, everything is well organized. We MARATHON colleagues, Tong Su, Mike Nycz, Tyler Kutz, Tyler Hague and Jason Bane, make a good team to take care of the experiment and fill in the shifts. Without everyone, the experiment wouldn't go so smoothly. And I enjoy those dinners with them after a day long collaboration meeting. All those activities with my friends Shujie Li, Dien Nguyen, Tong Su, Qian Zhang, Mike Nycz, Jia Shuo and Longwu Ou makes my life much more interesting in Newport News. Also, Dave Mack is very friendly with our international students. Thanks to him for all the small talks and persimmons. Talks with other people in JLab, like Cynthia Keppel, Jianwei Qiu, Nobuo Sato and Wally Melnitchouk, are always inspired. My thesis committee, Ernst Sichtermann,

William Zajc, Brian Cole and Alfred Mueller, took a rigorous attitude towards my thesis, which makes me think more about my analysis and what I should improve in the future. Thanks also to my boyfriend Cameron Clarke for the company in my last year in graduate school. He makes my life much more enjoyable. At the end, I'd like to thank my parents. I know they will always be there when I need them.

Chapter 1: Introduction

Among the many great successes of the Standard Model of particle physics, today we understand that fundamental particles – quarks and gluons – make up the fundamental substructure of the neutron and proton. Back in the 1950s, electron-proton elastic scattering experiments at the High Energy Physics Laboratory (HEPL) at Stanford found that the proton was not point-like, but instead had an extended internal structure. However, the information from the elastic scattering suggested that the hadron’s extended structure was comprised of “soft” charge and magnetic moment distributions with no underlying point-like constituents. Quarks, introduced in the early 1960s, were able to explain the low-energy properties of the hadrons, but met serious theoretical problems when considered as the physical constituents of nucleons in high energy scattering [1]. The quark model was not taken seriously until the first deep inelastic electron scattering experiment was performed at the Stanford Linear Accelerator Center (SLAC) [2]. In Chapter 1, the idea of deep inelastic scattering will be introduced, as well as the basic knowledge of parton distribution functions (PDFs) and nucleon structure functions in Quantum Chromodynamics (QCD).

Traditionally, the structure function ratio between neutron and proton, F_2^n/F_2^p , is measured using the hydrogen and deuterium targets. However, since the nuclear corrections applied to the deuteron data have large model dependence when $x > 0.6$, the ratio F_2^n/F_2^p extracted has big uncertainty at large x . In the MARATHON experiment, the nuclear effect model dependence is minimized by performing electron deep inelastic scattering on the mirror nuclei ^3H and ^3He . The EMC effect of ^3H and ^3He are also measured. The details about the MARATHON experiment motivation and the nuclear effects are given in Chapter 2.

The MARATHON experiment was performed at Jefferson Lab in the spring of 2018. The experiment kinematics and the experimental setup are described in Chapter 3. The data analysis procedure for the cross section ratio measurement is introduced in Chapter 4. The method to extract

F_2^n/F_2^p and the EMC effect ratios from data and their results are given in Chapter 5. In Chapter 6, future projects that might have comparable or improved results compared to the MARATHON experiment are introduced.

1.1 Deep inelastic scattering

1.1.1 Kinematics

When using the electron as a probe to study the structure of the nucleus, in an inclusive process, only incident electrons and scattered electrons are detected, as shown in Fig.1.1a. Assuming single photon exchange, the first order Feynman diagram for deep inelastic scattering (DIS) is shown in Fig.1.1b. The incident electron has incoming and outgoing four momentum of k and k' , and a four-momentum transfer given by $q = k - k'$, where the energy transfer is $\nu = E - E'$. Two invariants are commonly used to describe the scattering process. One is the negative square of the four-momentum transfer (neglecting the electron mass):

$$Q^2 := -q^2 = 4EE' \sin^2 \frac{\theta}{2}, \quad (1.1)$$

where θ is the electron scattering angle in the laboratory system. The other is the square of the invariant mass for the final hadron system:

$$W^2 = (p + q)^2 = M^2 + 2M\nu - Q^2, \quad (1.2)$$

where M is the mass of the hadron. Another important kinematic variable is Bjorken x , where $x = \frac{Q^2}{2M\nu}$. Its physics meaning will be introduced later.

Limited by the uncertainty principle, the spatial resolution that a virtual photon with momentum Q can reach is about \hbar/Q . With increasing beam energy E , the smaller structure inside the nucleus can be "seen" by the electron. Electron scattering is divided into four categories according to the particles involved in the scattering:

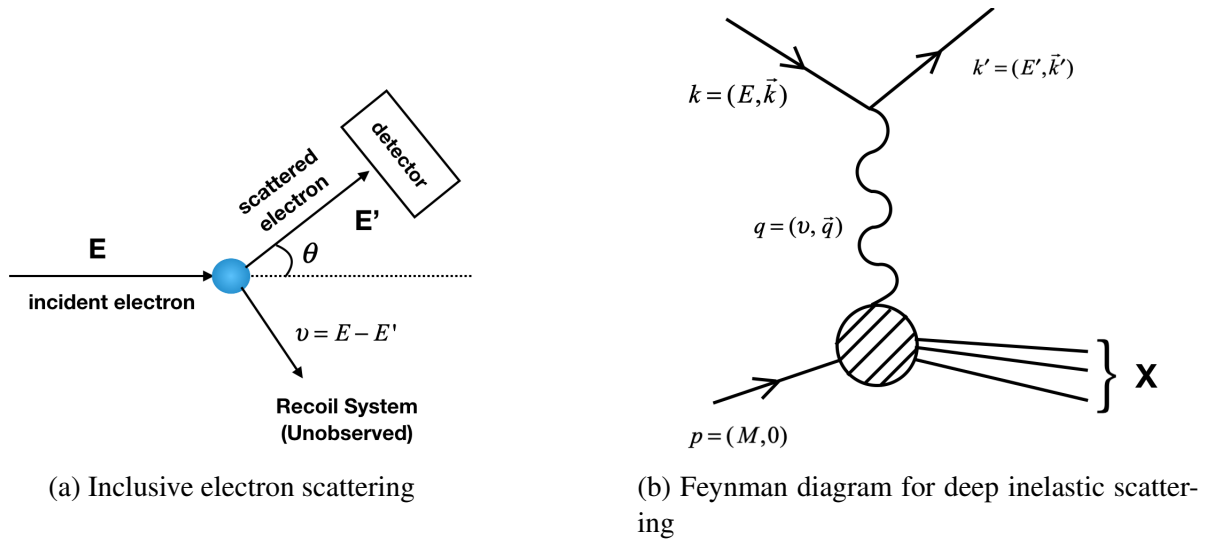


Figure 1.1: Electron scattering

Elastic scattering During elastic scattering, the nucleus stays intact. The electron scatters on the entire nucleus. The W^2 of the final hadron system is equal to the mass of the nucleus.

Quasi-elastic scattering When the energy transfer is bigger than the nuclear binding energy, the electron scattering probes the nucleons inside the nucleus. Since nucleons have Fermi motion, the quasi-elastic peak is wider than the elastic peak. The invariant mass W^2 is equal to the mass of an individual nucleon.

Resonance With increasing beam energy, one or more of the nucleons inside the nucleus can form excited states, called “nuclear resonances”. Also, with increased energy and momentum transfer, the individual nucleons form “resonances” with different spin or angular states. The invariant mass W^2 of the final hadron system is near the mass of the resonance.

Deep inelastic scattering As the incident electron energy continues to increase, one can probe the nucleon constituents. The scattering cross section becomes continuous. This is called deep inelastic scattering (DIS). In the MARATHON experiment, a cut of $W^2 > 3 \text{ GeV}^2$ is applied to distinguish DIS from resonances.

The cross section of electron scattering as a function of $\omega = 1/x$ is shown in Fig.1.2 for

electron-nucleon scattering and electron-nucleus scattering.

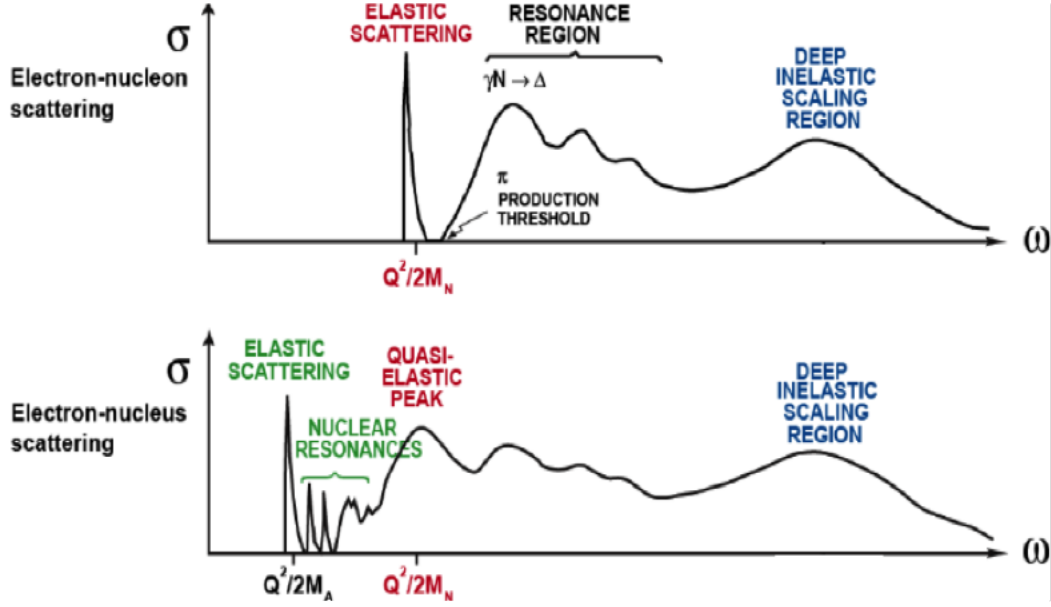


Figure 1.2: The spectra of electron-nucleon scattering and electron-nucleus scattering [3]

1.1.2 Bjorken scaling

The first electron DIS scattering experiment was performed at SLAC. Two unexpected features at that time appear in the data [1]. First, the measured cross section showed weak dependence on Q^2 , which was different from the behavior of elastic scattering. Furthermore, the nucleon structure functions W_1 and W_2 , which were extracted as analogs to the elastic form factors, have a scaling feature. The structure functions are related to the cross section by [4]:

$$\frac{d^2\sigma}{d\Omega dE'} = \sigma_{Mott}(W_2 + 2W_1 \tan^2 \frac{\theta}{2}). \quad (1.3)$$

In general, W_1 and W_2 are expected to be a function of both ν and Q^2 . However, as suggested by Bjorken, in the limit when $\nu \rightarrow \infty$, $Q^2 \rightarrow \infty$, νW_2 and W_1 become dependent on only one variable, x :

$$MW_1(\nu, Q^2) \rightarrow F_1(x) \quad , \quad \nu W_2(\nu, Q^2) \rightarrow F_2(x). \quad (1.4)$$

The data, indeed, displayed an approximate scaling behavior, as shown in Fig.1.3 [1].

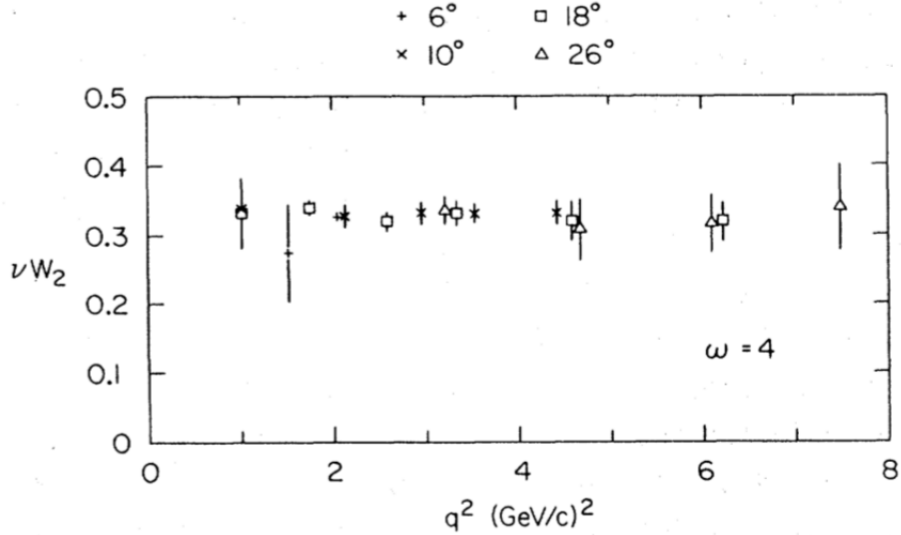


Figure 1.3: An early observation of scaling: νW_2 for the proton as a function of q^2 for $W > 2$ GeV, at $\omega = 4$

These two features catalyzed the excitement towards developing theoretical explanations. A number of non-constituent models were put forward, but none of them could describe the data over the full kinematic range. On the other hand, the scaling concept inferred from current algebra and its roots in the quark theory indicated that there are point-like, charged structures within the nucleon. The constituent model, *the parton model*, developed by Feynman with the assumption of point-like partons inside nucleons, automatically gave the scaling behavior [1]. While Feynman did not specify what the partons were, the quark model where the nucleons are composite of three valence quarks, a sea of quark-antiquark pairs and neutral gluons, was eventually confirmed by extensive electron DIS measurements and neutrino deep inelastic scattering in the 1970s [1].

1.2 Quark-parton model

The quark-parton model (QPM) interprets electron inelastic scattering on a hadron as an incoherent sum of the electron elastic scattering on the point-like partons inside the hadron. Suppose a parton of type i with momentum $P_i = x_i P$, where P is the three-momentum of the nucleon, and charge e_i scatters the electron in the range $d^3 k'$. In the $P \rightarrow \infty$ limit (with fixed q^2 and ν), the

cross section for this elementary elastic scattering is given by [5]:

$$d\sigma_i(x_i) \rightarrow \frac{P}{M} 8\alpha^2 q^{-4} e_i^2 \frac{x_i}{\nu} \delta(x_i - x) d^3 k'. \quad (1.5)$$

The probability of finding the type i parton with momentum $x_i P$ is $q_i(x_i)$. Then the DIS cross section of a nucleon is obtained by integrating over x_i and summing over all types of partons:

$$d\sigma(x) = \sum_i \int dx_i q_i(x_i) d\sigma_i(x_i) \rightarrow \sum_i \frac{P}{M} 8\alpha^2 q^{-4} e_i^2 \frac{x}{\nu} q_i(x) d^3 k'. \quad (1.6)$$

The cross section is proportional to q^{-4} . As the $Q^2 (= -q^2)$ of DIS is normally bigger than 2 GeV^2 , this explains the weak Q^2 dependence observed in the DIS cross section data. The Bjorken scaling variable x represents the fraction of nucleon momentum carried by the struck quark.

Another quantum field method to calculate the electron-nucleon DIS cross section in the fixed-target frame is done by introducing a hadronic tensor $W^{\mu\nu}$ in analogy to the leptonic tensor $L_{\mu\nu}^e$:

$$d\sigma \propto L_{\mu\nu}^e W^{\mu\nu} \quad (1.7)$$

For the $P \rightarrow \infty$ limit, the scattering angle is small ($\theta \rightarrow 0$), which makes W_2 the leading term kept in the asymptotic expression [5]:

$$d\sigma \rightarrow \frac{P}{M} 8\alpha^2 q^{-4} W_2(q^2, \nu) d^3 k'. \quad (1.8)$$

Comparing Eq.(1.6) and Eq.(1.8) relates the structure function W_2 to the quark momentum distributions by:

$$\nu W_2(q^2, \nu) = x \sum_i e_i^2 q_i(x) \quad (1.9)$$

On the other hand, W_1 is the dominant term when calculating the asymptotic limits for backward scattering $\theta = \pi$:

$$d\sigma \rightarrow \frac{1}{4} e^4 q^{-4} \frac{8\pi}{k \cdot P} Q^2 M W_1(q^2, \nu) \frac{d^3 k'}{(2\pi)^3 2E'}. \quad (1.10)$$

And for the same limit, the cross section for the electron-quark elastic scattering becomes:

$$d\sigma_i(x_i) \rightarrow \frac{1}{4} e^4 q^{-4} \frac{4\pi}{k \cdot P} Q^2 e_i^2 \delta(x_i - x) \frac{d^3 k'}{(2\pi)^3 2E'}. \quad (1.11)$$

Similarly, from Eq.(1.10) and Eq.(1.11), W_1 is related to the quark distribution by:

$$MW_1(q^2, \nu) = \frac{1}{2} \sum_i e_i^2 q_i(x) \quad (1.12)$$

As can be seen in Eq.(1.9) and Eq.(1.12), the QPM successfully predicts the Bjorken scaling behavior of structure functions. In the hadron infinite momentum frame, the momentum distribution of partons are “frozen” when the electron passes through the partons. In addition, in order to account for the difference between the experiment measured sum rules and the theoretical predictions, the QPM assumes the existence of the neutral partons (gluons) inside the nucleon. Even though the quark-parton model was tested to be successful by various experiments, there is one serious inconsistency between the model and the data. The quark-parton model is based on the impulse approximation which assumes that the quarks weakly interact with each other. As a result, single quark should be freed from the proton in the scattering process. But this is found not to be true in experiments. The quantum chromodynamics (QCD) theory developed afterwards eliminated this paradox.

1.3 Running coupling and asymptotic freedom

The perturbative expansion of scattering amplitudes beyond leading order is usually divergent. For example, in QCD, when introducing loop corrections to the gluon propagator as shown in Fig.1.4, the loop diagrams and other higher order diagrams are divergent since there is no restriction on the momentum flowing over the loop. These divergences are resolved by renormalization. For a dimensionless physical quantity R given by a perturbation series in the coupling $\alpha_s = g^2/4\pi$ (defined in analogy to the fine structure constant of QED), the divergence is removed by subtracting the renormalized R at some scale μ^2 . Then R in general depends on the ratio Q^2/μ^2 and the

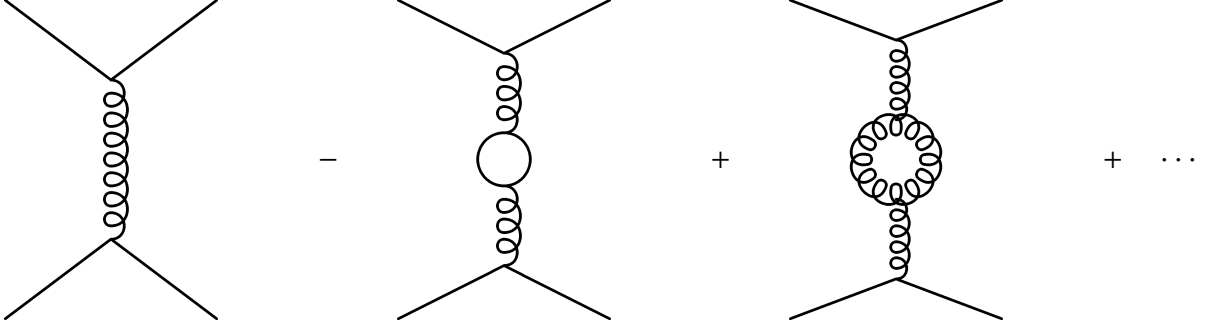


Figure 1.4: Loop corrections to the gluon propagator

coupling $\alpha_s(\mu^2)$. However, as the scale μ^2 is an arbitrary choice, the physical quantities should not depend on it, that is, the derivative of R on μ^2 is 0 [6]:

$$\mu^2 \frac{d}{d\mu^2} R(Q^2/\mu^2, \alpha_s) = \left[\mu^2 \frac{\partial}{\partial \mu^2} + \mu^2 \frac{\alpha_s}{\partial \mu^2} \frac{\partial}{\partial \alpha_s} \right] R = 0 \quad (\alpha_s \equiv \alpha_s(\mu^2)) \quad (1.13)$$

By introducing the notation $t = \ln(\frac{Q^2}{\mu^2})$ and $\beta(\alpha_s) = \mu^2 \frac{\partial \alpha_s}{\partial \mu^2}$, Eq.(1.13) can be rewritten as:

$$\left[-\frac{\partial}{\partial t} + \beta(\alpha_s) \frac{\partial}{\partial \alpha_s} \right] R(e^t, \alpha_s) = 0, \quad (1.14)$$

While R can be anything, this differential equation is solved if t satisfies:

$$t = \int_{\alpha_s(\mu^2)}^{\alpha_s(Q^2)} \frac{dx}{\beta(x)} \quad (1.15)$$

where $\alpha_s(Q^2)$ is defined as the running coupling. By differentiating Eq.(1.15), we get:

$$\frac{\partial \alpha_s(Q^2)}{\partial t} = \beta(\alpha_s(Q^2)) \quad , \quad \frac{\partial \alpha_s(Q^2)}{\partial \alpha_s(\mu^2)} = \frac{\beta(\alpha_s(Q^2))}{\beta(\alpha_s(\mu^2))} \quad (1.16)$$

Therefore $R(1, \alpha_s(Q^2))$ is a solution to Eq.(1.14). This shows that the scale dependence in R is absorbed into the coupling α_s by running it to the scale Q^2 .

In QCD, the β function has the perturbative expansion coming from the higher-order corrections shown in Fig.1.4 [6]:

$$\beta(\alpha_s) = -b\alpha_s^2(1 + O(\alpha_s)) \quad (1.17)$$

where

$$b = \frac{33 - 2n_f}{12\pi} \quad (1.18)$$

and n_f is the number of active light flavours. From Eq.(1.16), the $\alpha_s(Q^2)$ given by the first term of β is:

$$\alpha_s(Q^2) = \frac{\alpha_s(\mu^2)}{1 + \alpha_s(\mu^2)bt}. \quad (1.19)$$

As b is positive for $n_f < 17$, the coupling α_s logarithmically decreases when Q^2 increases, which is the opposite behavior compared to QED. This is the property referred to as asymptotic freedom. Inside a nucleus, at short distance (large Q^2) when α_s is close to zero, the partons are almost free from neighboring interactions. But at long distance (small Q^2), the coupling is so strong that it is impossible to isolate a free quark, since quark-antiquark pairs are created. This explains the remaining paradox in the QPM.

1.4 QCD improved parton model

The key feature of QPM remains in QCD that the DIS cross section can be factorized into a probability of finding a parton and the probability of a hard scattering on the parton. The difference is that in QCD, the parton density is non-perturbative, as the parton can have very small transverse momentum (which corresponds to a long-distance strong interaction), so only the hard scattering part is calculable by perturbation theory.

For the hard scattering process, higher order gluonic interactions are included. Firstly, the gluon radiation through the process $\gamma^*q \rightarrow qg$ is added to the zeroth order QPM process, as shown in Fig.1.5. The resulting structure function is given by [6]:

$$F_2(x, Q^2) = x \sum_{q, \bar{q}} e_q^2 [q_0(x) + \frac{\alpha_s}{2\pi} \int_x^1 \frac{d\xi}{\xi} q_0(\xi) \{P_{qq}(\frac{x}{\xi}) \ln \frac{Q^2}{\kappa^2} + C(\frac{x}{\xi})\} + \dots] \quad (1.20)$$

where ξ is the momentum fraction that a quark carries, $q_0(\xi)$ is regarded as the unmeasurable, "bare" distribution of a quark in the nucleon, and κ is an arbitrary cutoff introduced to regulate the

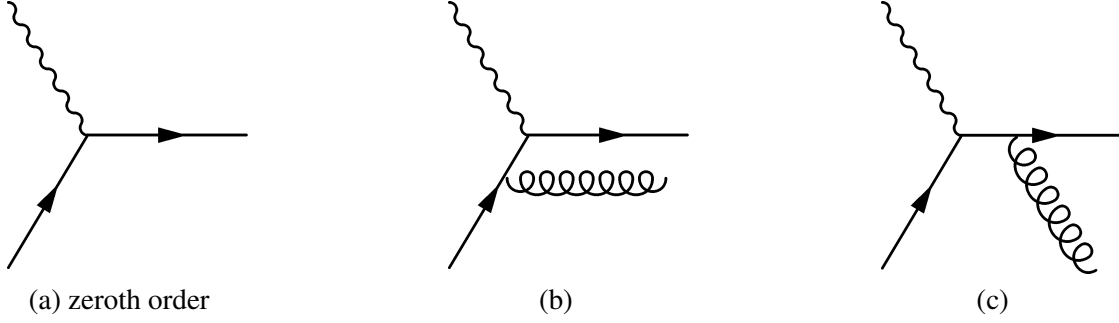


Figure 1.5: Feynman diagrams for gluon radiation from quarks in DIS

singularity which arises when the emitted gluon is parallel to the quark. P_{qq} , called the splitting function, represents the probability distribution for $q \rightarrow q(z)g(1-z)$, where the bracket () indicates the fractions of initial quark momentum. Both P_{qq} and C are calculable. Gluon radiation introduces a $\ln Q^2/\kappa^2$ scaling violation in the structure function. This has been observed in the data as shown in Fig.1.6. The dependence on the cutoff κ^2 is removed by introducing a “factorization scale” μ , so that the singularity is absorbed into the parton density $q(x, \mu^2)$:

$$q(x, \mu^2) = q_0(x) + \frac{\alpha_s}{2\pi} \int_x^1 \frac{d\xi}{\xi} q_0(\xi) \left\{ P_{qq}\left(\frac{x}{\xi}\right) \ln \frac{\mu^2}{\kappa^2} + C\left(\frac{x}{\xi}\right) \right\} + \dots \quad (1.21)$$

and Eq.(1.20) becomes:

$$F_2(x, Q^2) = x \sum_{q, \bar{q}} e_q^2 \int_x^1 \frac{d\xi}{\xi} q(\xi, \mu) \left\{ \delta\left(1 - \frac{x}{\xi}\right) + \frac{\alpha_s}{2\pi} P_{qq}\left(\frac{x}{\xi}\right) \ln \frac{Q^2}{\mu^2} + \dots \right\} \quad (1.22)$$

The factorization scale and the renormalization scale mentioned in the previous section are usually chosen to be the same. $q(x, \mu^2)$ can not be calculated in perturbation theory since it includes the long-distance strong interaction.

The other gluonic process that changes the quark momentum distribution is $\gamma^* g \rightarrow q\bar{q}$ as shown in Fig.1.7. The contribution to the structure function from this process is given by:

$$F_2^g(x, Q^2) = x \sum_{q, \bar{q}} e_q^2 \left[\frac{\alpha_s}{2\pi} \int_x^1 g_0(\xi) \left\{ P_{qg}\left(\frac{x}{\xi}\right) \ln \frac{Q^2}{\kappa^2} + C_g\left(\frac{x}{\xi}\right) \right\} + \dots \right], \quad (1.23)$$

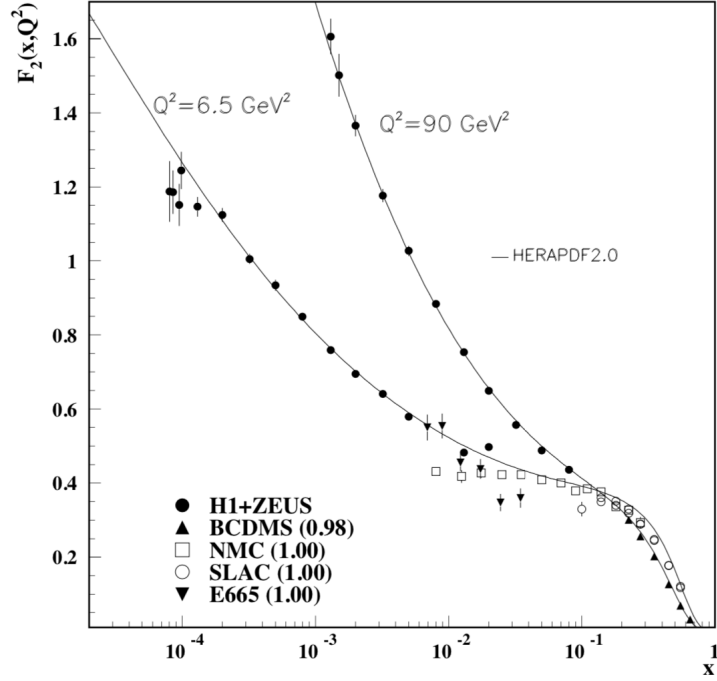


Figure 1.6: The proton F_2^p at two Q^2 values showing the Bjorken scaling violation [7]

where $g_0(\xi)$ is the “bare” momentum distribution of gluons in the nucleon, and P_{qg} is the splitting function for $g \rightarrow q(z)\bar{q}(1-z)$. Similarly, the $\kappa^2 \rightarrow 0$ singularity is handled by the factorization that it is absorbed by the gluon density $g_0(x) \rightarrow g(x, \mu^2)$. By adding Eq.(1.23) to Eq.(1.22), the quark distribution becomes:

$$q(x, \mu^2) = q_0(x) + \frac{\alpha_s}{2\pi} \int_x^1 \frac{d\xi}{\xi} q_0(\xi) \left\{ P_{qq}\left(\frac{x}{\xi}\right) \ln \frac{\mu^2}{\kappa^2} + C_q\left(\frac{x}{\xi}\right) \right\} \\ + \frac{\alpha_s}{2\pi} \int_x^1 \frac{d\xi}{\xi} g_0(\xi) \left\{ P_{qg}\left(\frac{x}{\xi}\right) \ln \frac{\mu^2}{\kappa^2} + C_g\left(\frac{x}{\xi}\right) \right\} + \dots$$

The exact definition of parton densities depends on the renormalization and factorization schemes. In the DIS scheme, by absorbing the gluon contribution into the quark distribution, the structure function $F_2(x, Q^2)$ is given by:

$$F_2(x, Q^2) = x \sum_{q, \bar{q}} e_q^2 q(x, Q^2) \quad (1.24)$$



Figure 1.7: Feynman diagrams for boson-gluon fusion in DIS

which has the same form as QPM but with a Q^2 dependence.

1.4.1 DGLAP evolution

Even though the parton distribution is non-perturbative, its evolution along the factorization scale μ^2 can be calculated by the renormalization group methods and operator product expansion (OPE), which is known as the Dokshitzer-Gribov-Lipatov-Altarelli-Parisi (DGLAP) equation. The form of DGLAP equations are given by[8]:

$$\frac{\partial}{\partial \ln Q^2} \Sigma(x, Q^2) = \frac{\alpha_s(Q^2)}{2\pi} ([\Sigma \otimes P'_{qq}] + [g \otimes 2n_f P_{qg}]) \quad (1.25)$$

$$\frac{\partial}{\partial \ln Q^2} g(x, Q^2) = \frac{\alpha_s(Q^2)}{2\pi} ([\Sigma \otimes P'_{gq}] + [g \otimes 2n_f P_{gg}]) \quad (1.26)$$

$$\frac{\partial}{\partial \ln Q^2} q_i^\pm(x, Q^2) = \frac{\alpha_s(Q^2)}{2\pi} [q_i^\pm \otimes P_\pm] \quad (1.27)$$

where the convolution is defined as:

$$[q \otimes P](x, Q^2) \equiv \int_x^1 \frac{d\xi}{\xi} q(\xi, Q^2) P\left(\frac{x}{\xi}\right) = \int_x^1 \frac{d\xi'}{\xi'} q\left(\frac{x}{\xi'}, Q^2\right) P(\xi'). \quad (1.28)$$

$\Sigma(x, Q^2)$ is the singlet quark density: $\Sigma = \sum_i (q_i + \bar{q}_i)$, $q_i^- = q_i - \bar{q}_i$ and $q_i^+ = q_i + \bar{q}_i - \frac{1}{n_f} \Sigma$ are the non-singlet combinations. The splitting functions P are calculable as a power series in α_s . The leading-order splitting function $P_{ab}^{(0)}$ is regarded as the probability of finding a parton of type a in a parton of type b with a fraction x of the longitudinal momentum of the parent parton [6]. Once

the parton densities are known at a starting scale Q_0^2 , the DGLAP equation is able to calculate the parton densities at higher Q^2 from it. However, the parton densities at the starting scale Q_0^2 are non-perturbative. They can either be calculated by non-perturbative methods which are still under development [9], or by the parameterization of experimental data.

1.4.2 High twist and target mass correction

Technically, high twist is the $1/Q^2$ correction term to the leading order DGLAP for DIS structure functions. It rises up at lower Q^2 where the nucleon resonances dominate, or at high x where the elastic scattering limit dominates. So the assumption of incoherent scattering on the partons in DIS is no longer valid, and the interactions between partons have to be taken into consideration.

From the OPE, the moments of the structure function or parton densities can be expanded as power series in $1/Q^2$: $\sum(1/Q^2)^{\tau/2-1}C_\tau(Q^2)\dots$, where $\tau \geq 2$ is the twist. The twist is defined as the difference between the mass dimension and the spin of an operator [8]. At large Q^2 , the leading twist 2 terms give a good approximation for the moments, and the scaling violation dependence on $\ln Q^2$ is contained in $C_\tau(Q^2)$. However, at lower Q^2 or high x , the higher twist terms become large. The twist 4 terms need to be included. While these corrections are difficult to calculate, the twist-4 coefficients are determined by adding an additional term to the fitting function of F_2 data:

$$F_2^{HT}(x, Q^2) = F_2^{LT}(x, Q^2)[1 + C_{HT}(x, Q^2)/Q^2] \quad (1.29)$$

where F_2^{LT} is the leading twist contribution, C_{HT} is the contribution from twist-4.

The twist expansion from pQCD is derived in the limit that the mass of the hadron is negligible when compared with Q^2 . At finite Q^2 , where low energy fixed target experiments are performed, a target mass correction (TMC) is applied to account for the neglect of $O(m^2/Q^2)$ terms in the kinematic variables. The TMC can be absorbed into the leading twist term [10]. Then the F_2 fitting function becomes [9]:

$$F_2(x, Q^2) = O_{TMC}[F_2^{twist-2}(x, Q^2)][1 + C_{HT}(x, Q^2)/Q^2] \quad (1.30)$$

where O_{TMC} describes the inclusion of the TMC of the twist-2 contributions to the structure function.

Chapter 2: F_2^n/F_2^p and EMC effect

The nucleon structure functions measured, in fixed-target DIS experiments, provide precise constraints on the valence quark distributions. The proton structure function F_2^p is extracted using a hydrogen target. Since there is no free neutron target, the neutron structure function F_2^n is found using nuclear targets with $A \geq 2$. However, the discovery of the EMC effect shows that there is unexpected behavior implying the nuclear structure function is not simply the sum of the nucleon structure functions [11]. This led to the study of nuclear effects, which modifies the structure functions for nuclei. The motivation of the MARATHON experiment is to measure the cross section ratios at large x , so that the neutron to proton structure function ratio can be obtained at large x as well as the d quark over u quark ratio, and to understand the nuclear effects.

2.1 F_2^n/F_2^p and d/u

From the parton model, the F_2 structure function is related to the struck quark densities by $F_2(x) = x_i \sum_i e_i^2 q_i(x)$. The electric charges carried by u , d and s quark are $2/3$, $-1/3$ and $-1/3$. Therefore, the proton structure function F_2^p is given by:

$$F_2^p(x) = x \left[\left(\frac{2}{3}\right)^2 (u + \bar{u}) + \left(-\frac{1}{3}\right)^2 (d + \bar{d}) + \left(-\frac{1}{3}\right)^2 (s + \bar{s}) \right]. \quad (2.1)$$

Since the u/d quarks and proton/neutron are both isospin symmetric, the $u(d)$ quark in the proton has same distribution as the $d(u)$ quark in the neutron: $u^p(x) = d^n(x) \equiv u(x)$, $d^p(x) = u^n(x) \equiv d(x)$, and similarly for anti-quarks. The resulting neutron structure function F_2^n is expressed by:

$$F_2^n(x) = x \left[\left(\frac{2}{3}\right)^2 (d + \bar{d}) + \left(-\frac{1}{3}\right)^2 (u + \bar{u}) + \left(-\frac{1}{3}\right)^2 (s + \bar{s}) \right]. \quad (2.2)$$

From Eq.(2.1) and Eq.(2.2), F_2^n/F_2^p is given by:

$$\frac{F_2^n}{F_2^p} = \frac{4(d + \bar{d}) + (u + \bar{u}) + (s + \bar{s})}{4(u + \bar{u}) + (d + \bar{d}) + (s + \bar{s})} \quad (2.3)$$

Neglecting the strange quarks and anti-quarks, it becomes:

$$\frac{F_2^n}{F_2^p} = \frac{1 + 4d/u}{4 + d/u}, \quad (2.4)$$

here the $u(d)$ is the sum of the quarks and anti-quarks. Therefore, precise measurement of F_2^n/F_2^p can provide constraints on the d/u ratio.

2.1.1 d/u at large x

One of the factors that has a large impact on the parameterizations of PDFs is the assumption on d/u behavior as $x \rightarrow 1$. It is apparent from Eq.(1.25) to Eq.(1.28) that the quark distributions at $x = 1$ are invariant under evolution. When $x = 1$, the process becomes elastic scattering on the nucleon, and in the limit $Q^2 \rightarrow \infty$, the elastic form factors vanish. But what's more important is the rate at which the distribution functions vanish with x , since this can lead to a nonzero renormalization-scale-invariant distribution function ratio at $x = 1$ [9]. The predictions for d/u as $x \rightarrow 1$ from different models range from 0 to 0.5. Therefore, the experimental measured d/u at large x becomes a discriminator between models.

If SU(6) symmetry were exact, the wave function of a proton polarized in the $+z$ direction is given by [12]:

$$\begin{aligned} p \uparrow = & \frac{1}{\sqrt{2}} u \uparrow (ud)_{S=0} + \frac{1}{\sqrt{18}} u \uparrow (ud)_{S=1} - \frac{1}{3} u \downarrow (ud)_{S=1} \\ & - \frac{1}{3} d \uparrow (uu)_{S=1} - \frac{\sqrt{2}}{3} d \downarrow (uu)_{S=1}, \end{aligned} \quad (2.5)$$

where S denotes the total spin of the two-quark component. In this limit, the u quark and d quark in proton would be identical, and the distribution function of each valence quark should be equivalent,

which implies $u(x) = 2d(x)$ for all x . It gives the neutron to proton F_2 structure function ratio as:

$$\frac{F_2^n}{F_2^p} = \frac{2}{3} \quad , \quad \frac{d}{u} = \frac{1}{2} \quad [\text{SU(6) symmetry}] \quad (2.6)$$

However, the SU(6) symmetry is broken naturally as the masses of the nucleon and Δ are split by about 300 MeV. Furthermore, the experimental measured F_2^n/F_2^p drops well below $2/3$.

The correlations between the mass splitting of the nucleon and Δ and the large- x behavior of F_2^n/F_2^p was observed by Close [13] and Carlitz [14]. They assume the nucleon first breaks up into a quark which then interacts with the virtual photon, and the remaining nucleon constituents are regarded as a pair ‘‘diquark’’. The suppression of the ‘‘diquark’’ $S = 1$ state relative to $S = 0$ state can explain the symmetry breaking. When $x \rightarrow 1$, the ratio of the $S = 1$ state term over the $S = 0$ state term vanishes. The first term in Eq.(2.5) is dominant, so that F_2^p is essentially given by the single u quark distribution at $x = 1$, in which case:

$$\frac{F_2^n}{F_2^p} = \frac{1}{4} \quad , \quad \frac{d}{u} = 0 \quad [S = 0 \text{ dominance}] \quad (2.7)$$

The suppression of the $S = 1$ state can be understood in analogy to the atomic hyperfine splitting as a color hyperfine interaction. In the hyperfine-perturbed quark model [15], at lowest order, the Hamiltonian for the color-magnetic hyperfine interaction between two quarks is proportional to $\vec{S}_i \cdot \vec{S}_j$, where \vec{S}_i is the spin vector of quark i . This force is repulsive if the spins are parallel and is attractive when they are anti-parallel. Hence, it leads to the $S = 1$ state suppression, and results in the $d/u \rightarrow 0$ at $x = 1$.

Another suggestion on the SU(6) symmetry breaking is based on perturbative QCD from Farrar and Jackson [16]. They postulate at $x \approx 1$, the hadron structure functions can be calculated to $O(m^2/q^2)$ by lowest-order perturbation theory where the incoming quarks can be treated as free. The results of the calculation shows that when the spins of two quarks are aligned, only the exchange of a longitudinal gluon is allowed due to angular momentum conservation, so the contribution to the structure function from the aligned quarks is suppressed by $(1 - x)$ relative to

the anti-aligned quarks. That is to say, the “diquark” with the state $S_z = 0$ is dominant when $x \rightarrow 1$. Thus, the quark from which the virtual photon scatters has the same helicity as the nucleon itself. From Eq.(2.5), we can see the probability of the u quark having the same helicity as the proton is five times the probability of the d quark having the same helicity as the proton. This gives d/u and F_2^n/F_2^p as:

$$\frac{F_2^n}{F_2^p} = \frac{3}{7} \quad , \quad \frac{d}{u} = \frac{1}{5} \quad [S_z = 0 \text{ dominance}] \quad (2.8)$$

A later exposition from Brodsky *et al.* based on counting-rules gives a similar result [17]. It predicts that the helicity-parallel quark distribution $q^+(x)$ is enhanced relative to the helicity-anti-parallel quark distribution $q^-(x)$: $q^\pm(x) \sim (1-x)^{2n-1+2\Delta S_z}$, where n is the minimum number of spectator quarks and $\Delta S_z = 0$ for parallel quarks and $\Delta S_z = 1$ for anti-parallel quarks to the proton helicities. This leads to same prediction as Eq.(2.8).

In order to understand the dynamics of the quark distribution at large x , experimental measurements of d/u at large x are needed to examine these theoretical predictions.

2.1.2 F_2^n from deuteron data

The u quark distribution is well constrained by existing F_2^p data. The d quark is more sensitive to F_2^n which is normally extracted from the deuteron data. An uncertainty induced by the nuclear corrections applied to F_2^d limits the precision for the d quark distribution extraction. Before, only Fermi motion correction was considered to account for the binding effects for the deuteron. The extracted F_2^n/F_2^p goes to 1/4 and d/u goes to 0 as $x \rightarrow 1$. So most parameterizations set $d/u = 0$ at $x = 1$. However, a reanalysis of SLAC and NMC data by including more nuclear corrections suggests that the pQCD predicted $F_2^n/F_2^p \rightarrow 3/7$ and $d/u \rightarrow 0.2$ as $x \rightarrow 1$ are allowed, which leads to an about ~40% change in the d quark distribution at $x = 0.5$ [18]. Therefore, understanding deuteron nuclear effects is crucial for the determination of F_2^n/F_2^p at large x .

In the valence quark region ($x \gtrsim 0.3$), the impulse approximation is mostly used to describe the deuteron structure function. In this approximation, only one nucleon is directly involved in the scattering process, and the total γ^*D amplitude is factorized into γ^*N and ND amplitudes. So the

deuteron structure function is a convolution of a smearing function $f(y)$ and the nucleon structure functions as:

$$F_2^d(x, Q^2)^{(\text{conv})} = \int dy f(y) [F_2^p(\frac{x}{y}, Q^2) + F_2^n(\frac{x}{y}, Q^2)]. \quad (2.9)$$

where $f(y)$ accounts for the Fermi motion and binding effects of the deuteron. As F_2^n and F_2^p are the free nucleon structure functions, an additional off-shell correction that can not be included in the convolution is added:

$$F_2^d = F_2^{d(\text{conv})} + \delta^{(\text{off})} F_2^d \quad (2.10)$$

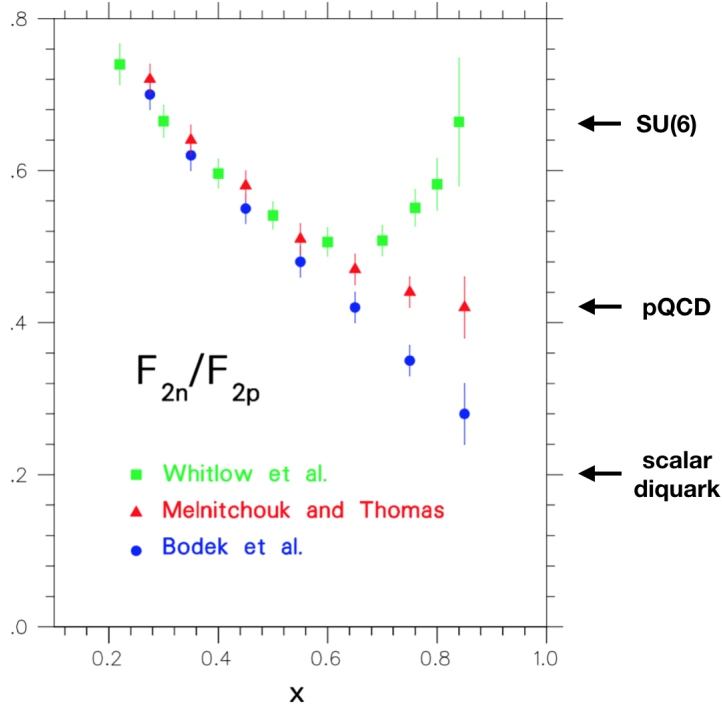


Figure 2.1: The ratio F_2^n/F_2^p extracted from deuteron and proton data with a) only Fermi motion considered (Bodek *et al.* [19]), b) Fermi motion, binding effects and off-shell corrections included (Melnitchouk and Thomas [20]), c) using nuclear density model (Whitlow *et al.* [21]).

The F_2^n/F_2^p extracted from deuteron and proton data using different nuclear models can be quite different, as shown in Fig.2.1. In the early days the deuteron analysis by Bodek *et al.* [19], the nuclear effects were considered to be small as the binding energy of the deuteron is only 2.2 MeV, while the energy transfer in the scattering process is at GeV level. Only the nucleon Fermi motion was taken into account in $f(y)$, and the off-shell correction is ignored. This gives the result that

$F_2^n/F_2^p \rightarrow 1/4$ as $x \rightarrow 1$. However, the discovery of the EMC effect (introduced later) indicates that nuclear effects inside nuclei are larger than expected, and only including the Fermi motion is not sufficient, as shown in Fig.2.2 [22]. Melnitchouk and Thomas add the binding effects to $f(y)$

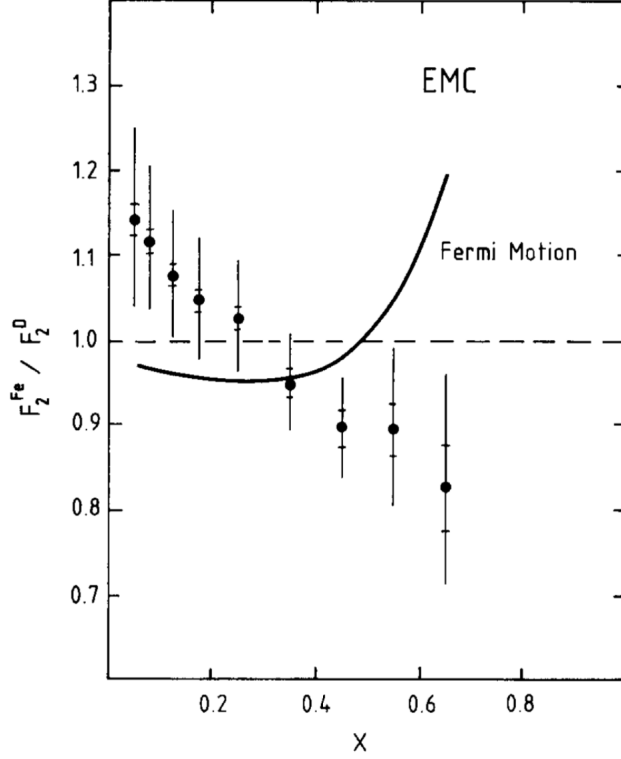


Figure 2.2: The ratio $F_2(Fe)/F_2^d$ averaged over Q^2 as a function of x . The curve shows the the expected behavior by including the Fermi motion of the nucleons in the nucleus.

and includes the off-shell corrections as Eq.(2.10) [20]. The F_2^n/F_2^p extracted is larger than 1/4 and in general consistent with the pQCD expectation of 3/7 as $x \rightarrow 1$. An alternative method to incorporate binding effects performed by Whitlow *et al.* [21] uses the nuclear density model from Frankfurt and Strikman [23]. In this model, the EMC effect of the deuteron was assumed to scale similarly to heavier nuclei according to the ratio of the nuclear densities [12]:

$$\frac{F_2^d}{F_2^p + F_2^n} = 1 + \frac{\rho_d}{\rho_A - \rho_d} \left[\frac{F_2^A}{F_2^d} - 1 \right] \quad (2.11)$$

where ρ_d is the charge density of deuterium nucleus, and ρ_A and F_2^A are the charge density and structure function of an atomic number A nucleus. The result of F_2^n/F_2^p from this method is

significantly higher than the others and is close to the SU(6) expectation as $x \rightarrow 1$. Melnitchouk and Thomas point out that even though the extrapolation from heavier nuclei to the deuteron is qualitatively reasonable, due to the special nature of the deuteron, where the neutron and proton are far apart, the extrapolation can not be considered quantitatively reliable [20].

A recent study by J. Arrington *et al.* [24] argues that it is important to account properly for the Q^2 dependence of the data especially for $x \gtrsim 0.7$, and some of the variations in F_2^n/F_2^p can result from the inconsistent treatment of kinematics of the data and calculations. Also, a careful study on the systematic uncertainties of F_2^n/F_2^p induced by nuclear effect model dependence is performed using different wave functions, different smearing models and off-shell predictions [25]. The results, as shown in Fig.2.3, have a much smaller uncertainty at large x compared with that shown on Fig.2.1. While the total uncertainty in Fig.2.3 is calculated as a quadrature sum of different kinds of uncertainties, this may not be reliable since different uncertainties can be correlated. Taking a linear sum of all uncertainties shown in Fig.2.3 gives the range $0.04 < F_2^n/F_2^p < 0.42$ at $x = 1$. Here, the pQCD prediction is not ruled out.

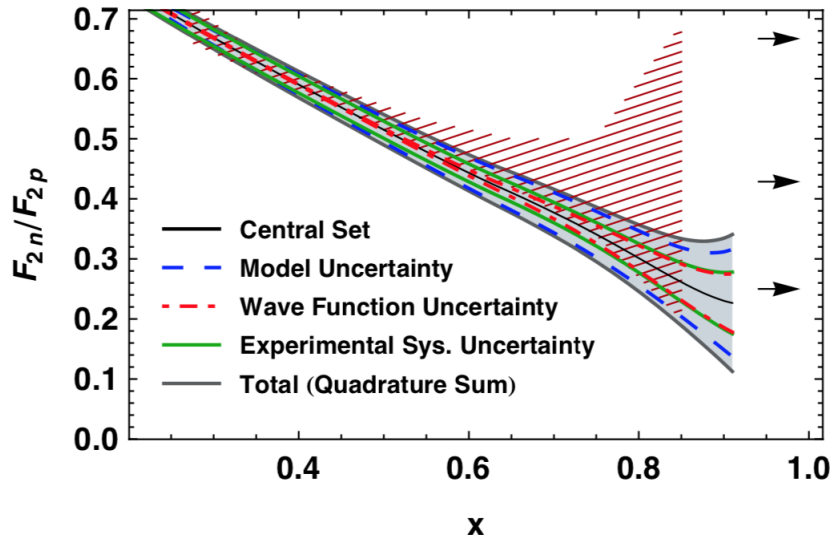


Figure 2.3: The F_2^n/F_2^p ratio together with the uncertainties induced by nuclear effects models. “Model uncertainty” is the uncertainty from the smearing function and off-shell effects. The red hatched region corresponds to the uncertainty range in Fig.2.1.

2.2 The EMC effect

The EMC effect is named after the European Muon Collaboration, who were the first group to discover the effect, somewhat by accident [11]. Originally, the European Muon Collaboration performed muon scattering on hydrogen, deuterium and iron targets to measure the structure functions. The use of iron targets was to increase the luminosity. When they compared the iron structure function F_2^{Fe} to the deuterium structure function F_2^d per nucleon, the ratio was not unity, as shown in Fig.2.2, that is to say the nucleon structure function inside the nucleus is modified by the nuclear medium, and the nuclear effects were significantly larger than expected. After the initial finding, many experiments have confirmed the features of the EMC effect. A list of experiments can be found in [26]. After many years, the experimental results for σ_A/σ_D per nucleon as a function of x agree. The prominent features are: the ratio is less than unity at very small x , and rises and crosses 1 as $x \sim 0.1$, then falls to a minimum at $x = 0.65$ and thereafter rises steeply, as shown in Fig.2.4. The x region is divided into separate regions: shadowing ($x \lesssim 0.1$, where the ratio is below unity at very small x), anti-shadowing (around $0.1 \lesssim x \lesssim 0.28$, where the ratio is above 1), and the EMC effect ($x \gtrsim 0.28$, where the ratio is below unity in the middle x). At high x , the rapid rise presumably comes from the Fermi motion. On the other hand, the EMC effect has weak Q^2 dependence, and decreases logarithmically with A [27].

2.2.1 Theoretical models of the EMC effect

The EMC effect suggests that the valence quarks in the nucleus tend to carry a smaller fraction of the momentum of nucleons than in free nucleons. Many theoretical models attempt to explain the origin of this trend. They can be divided into five categories: binding and x rescaling models, pion enhancement models, multiquark clusters models, dynamical rescaling models, and short range correlation models. The detailed review of the first four categories can be found in [26]. The light nuclei EMC results from JLab [33], which show that the EMC effect likely depends on the local nuclear density, have renewed the interest of studying short range correlations in recent years.

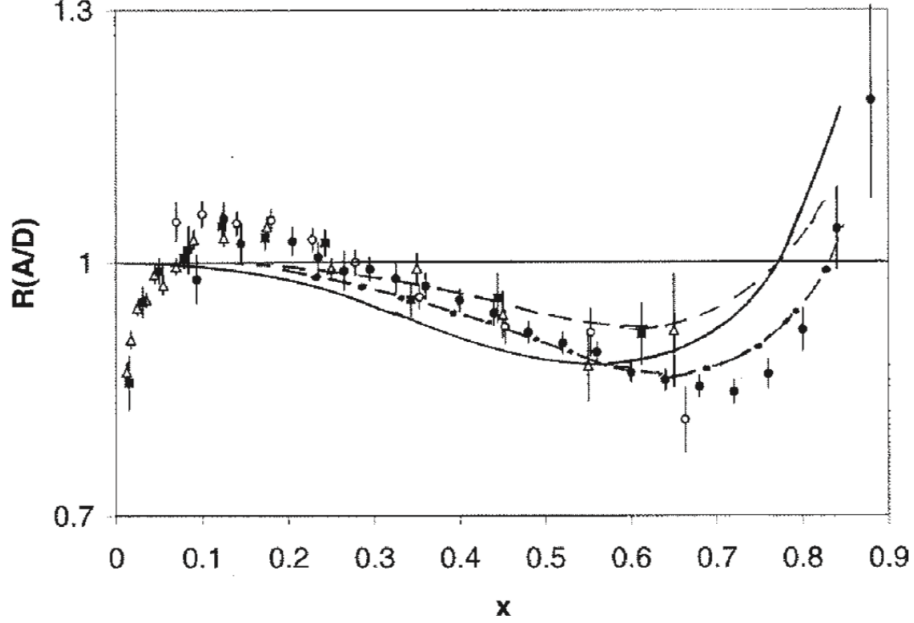


Figure 2.4: The typical EMC effect of a nucleus. The data comes from [27] (solid circles), [28] (solid squares), [29] (open circles), and [30] (open triangles). The theoretical models are based on the x rescaling. The solid line is from [31], and the dashed line and dashed-dotted line are from [32] with values of $\langle \epsilon \rangle$ of -26 and -39 MeV, respectively. [26]

Binding and x rescaling models

The models of the binding effects and Fermi motion before the discovery of the EMC effect assumed that the struck nucleon was off-shell and possessed a Fermi momentum, while the rest of the nucleus, comprising $A-1$ nucleons, remained in the ground state. However, in general, when a nucleon is knocked out of a nucleus, the recoil energy will excite the residual nucleus to an excited state. This is included in the later binding models by defining a separation energy ϵ_λ of the struck nucleon in the orbital specified by λ and a momentum \vec{p} :

$$\epsilon_\lambda = M_A - M_{A-1}^\lambda - M_N \quad (2.12)$$

where M_A and M_N are the mass of the nucleus and the nucleon, and M_{A-1}^λ is the mass of the residual nucleus in the excited state [34]. Then the Bjorken x becomes:

$$x' = \frac{Q^2}{2p' \cdot q}, \quad (2.13)$$

where p' is $(M_N + \langle \epsilon \rangle, \vec{p})$, which neglects the recoil nucleus, and $\langle \epsilon \rangle$ is the separation energy averaged over all occupied shells. The off-shell nucleon apparently has a negative $\langle \epsilon \rangle$. So x is smeared by the Fermi momentum \vec{p} and shifted by an amount $(-\langle \epsilon \rangle/M)$. The rescaling of x is able to explain the EMC ratio R_{EMC} for $x > 0.3$. However, this approach is criticized for the improper normalization of the spectral function. Frankfurt and Strikman point out that a flux factor correction should be applied in a fully relativistic theory, which strongly reduces the effect of $\langle \epsilon \rangle$ [35].

The remaining issue in this approach is the values of $\langle \epsilon \rangle$. The mean separation energy determined from single nucleon knockout reactions such as $(p, 2p)$ and $(e, e'p)$ rapidly saturates with increasing A at around -25 MeV, while -40 MeV has been used to explain the iron data. On the other hand, some suggest that direct measurements in these reactions may miss the high energy component generated by nucleon correlations [26]. The short-range and tensor correlations resulting from realistic nucleon-nucleon interactions strongly increase the mean separation energy, and as a result the agreement with data is partially recovered [36]. However, the agreement between the model and the data is only qualitative, as shown in Fig.2.4. It is difficult to simultaneously satisfy agreement in multiple x regions.

Pion enhancement models

In the nucleus, the nucleons are bound together presumably by the exchange of mesons, mostly pions. The nucleus' momentum is shared between the nucleons and pions. An increase in the number of virtual pions as A increases can produce an EMC effect at small x , implying a depletion at large x through momentum conservation. The nuclear structure function per nucleon is calculated by summing over the nucleon structure function and the pion structure function in a convolution formalism:

$$F_2^A(x) = \int_{x/A}^1 f_N(z) F_2^N\left(\frac{x}{Az}\right) dz + \int_{x/A}^1 f_\pi(z) F_2^\pi\left(\frac{x}{Az}\right) dz, \quad (2.14)$$

where z is the momentum fraction carried by the nucleon or pion, $f_N(z)$ and $f_\pi(z)$ are the momentum distributions of nucleons and pions, F_2^N and F_2^π are the free nucleon and pion structure

function. The agreement between the pion models and the data are qualitatively good, as shown in Fig.2.5 [26]. However, the evidence for the pion fields enhancement hasn't been found so far. For example, the enhancement of pion fields naturally indicates an enhancement of the sea quarks in nuclei. This contradicts the results from Drell-Yan experiments, which found no evidence for an enhancement of anti-quarks [37].

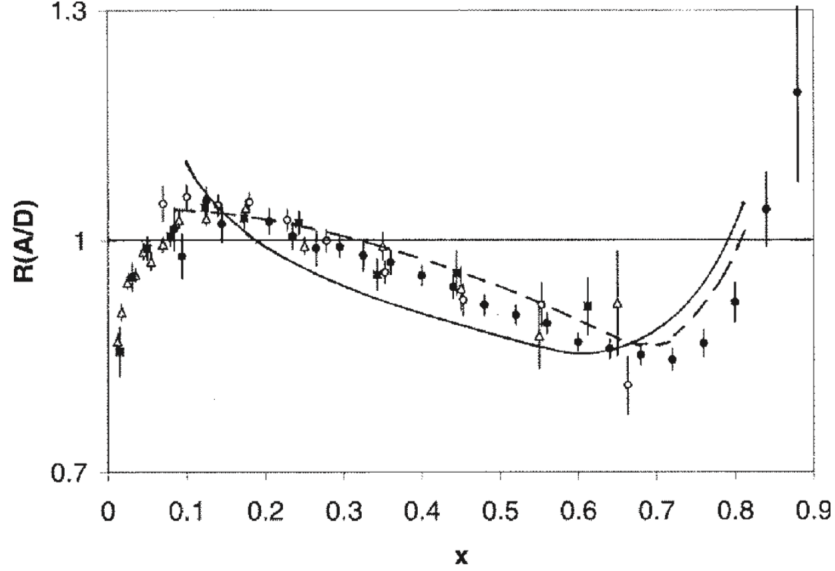


Figure 2.5: Comparison between EMC effect data and the pion enhancement models. The data are the same as Fig.2.4. The solid line is from [38], and the dashed line is from [39].

Multiquark clusters models

In dense nuclei, the nucleons are tightly packed so part of the nucleons can be viewed and treated as multiquark clusters. Color-singlet states can be made of 6, 9, 12 etc quarks. The nuclear structure function per nucleon is then expressed as the sum over nucleons and six-quark clusters (and can be extended to larger clusters):

$$F_2^A(x) = \int_{x/A}^1 f_N(z) F_2^N\left(\frac{x}{Az}\right) dz + \int_{x/A}^1 f_6(z) F_2^6\left(\frac{x}{Az}\right) dz, \quad (2.15)$$

where $f_6(z)$ is the momentum distribution of the six-quark clusters, and F_2^6 is the six-quark structure function. The normalization:

$$\int f_N(z)dz = 1 - p \quad , \quad \int f_6(z)dz = p \quad (2.16)$$

gives the probability of forming six-quark clusters inside a nucleus, which reflects the fraction of the time that the nucleons are found very close together with overlapping wave functions. For the structure function of six-quark clusters, one can get an idea from [40] which gives $F_2(x) \sim (1 - x)^{2n-1}$ where n is the number of spectator quarks. Since $6q$ clusters have 5 spectator quarks and the range of x is extended to 2, the $6q$ structure function can be $F_2^6(x) \sim (1 - x/2)^9$ [26]. This formula is only expected to be valid at large x . It shows that F_2^6 is softer than the nucleon structure function, which leads to the depletion of the iron structure function, and it has a hard tail that explains the rapid rise in R_{EMC} at very large x . A comparison with data is shown in Fig.2.6.

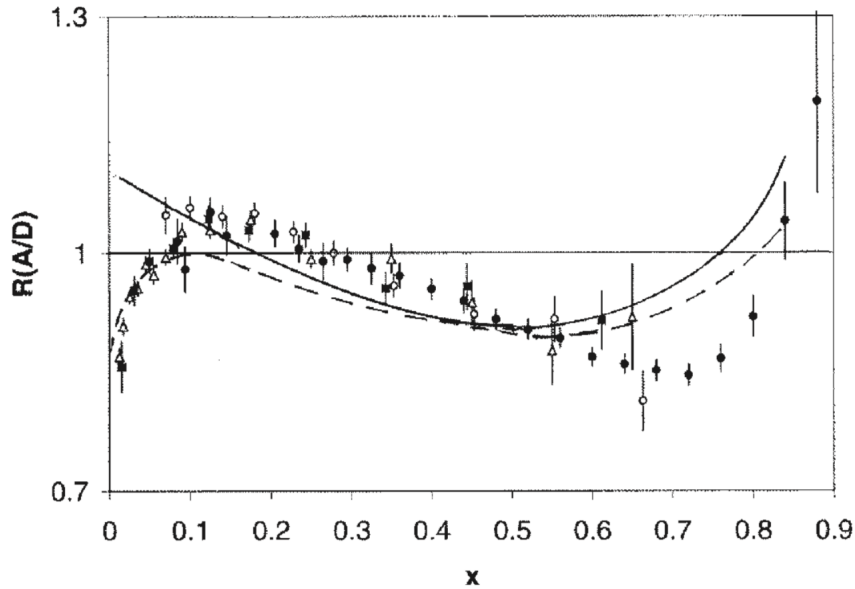


Figure 2.6: Comparison between EMC effect data and the quark cluster model. The data are the same as Fig.2.4. The solid line is from [41], and the dashed line is from [42].

However, there is no evidence found for the existence of multiquark clusters. Their structure function and momentum distribution require guessing, and are sensitive to many parameters.

Therefore, this approach does not have much predictive power.

Dynamical rescaling models

It was found that the discrepancy between F_2^{Fe} and F_2^d largely disappears if the comparison is made between the deuterium data at Q^2 and the iron data at $Q^2/2$ [43]. This suggests that the EMC effect might be due to the deconfinement of quarks and gluons inside a nucleus compared to that in a free nucleon. In the framework of pQCD, such a change in confinement scale leads to the rescaling relation between nuclear structure functions as [43]:

$$\frac{1}{A'} F_2^{A'}(x, Q^2) = \frac{1}{A} F_2^A(x, \xi_{AA'}(Q^2) Q^2) \quad (2.17)$$

where $\xi_{AA'}$ is the ‘‘rescaling parameter’’ given by:

$$\xi_{AA'}(Q^2) = \left(\frac{\lambda_{A'}^2}{\lambda_A^2} \right)^{\alpha_s(\mu_{A'}^2)/\alpha_s(Q^2)}. \quad (2.18)$$

where α_s is the QCD running coupling constant, and λ_A is the confinement scale. The renormalization scale μ_A occurs when the nucleon only consists of valence quarks and no gluons radiated.

The relation between λ_A and μ_A is given by:

$$\mu_{A'}^2 = \left(\frac{\lambda_A^2}{\lambda_{A'}^2} \right) \mu_A^2 \quad (2.19)$$

λ_A is obtained by assuming that the change in the confinement size is proportional to the probability that two nucleons overlap with one another.

The EMC effect predicted from Eq.(2.17) has good agreement with data at intermediate x , although it predicts a smaller crossing point when $R_{EMC} = 1$ at ~ 0.25 , as shown in Fig.2.7. It is not applicable at small and very large x where substantial next-to-leading order QCD corrections need to be considered. One explanation for the change in quark confinement size is that the bound nucleon size increases relative to the free one, referred to as nucleon ‘‘swelling’’. However, the

change of nucleon size should also lead to a change in the elastic form factors, for which no experimental evidence has been found [27].

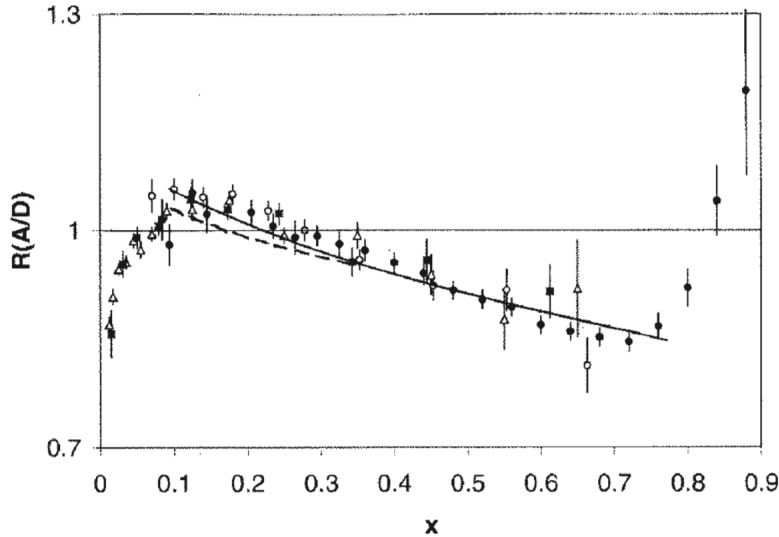
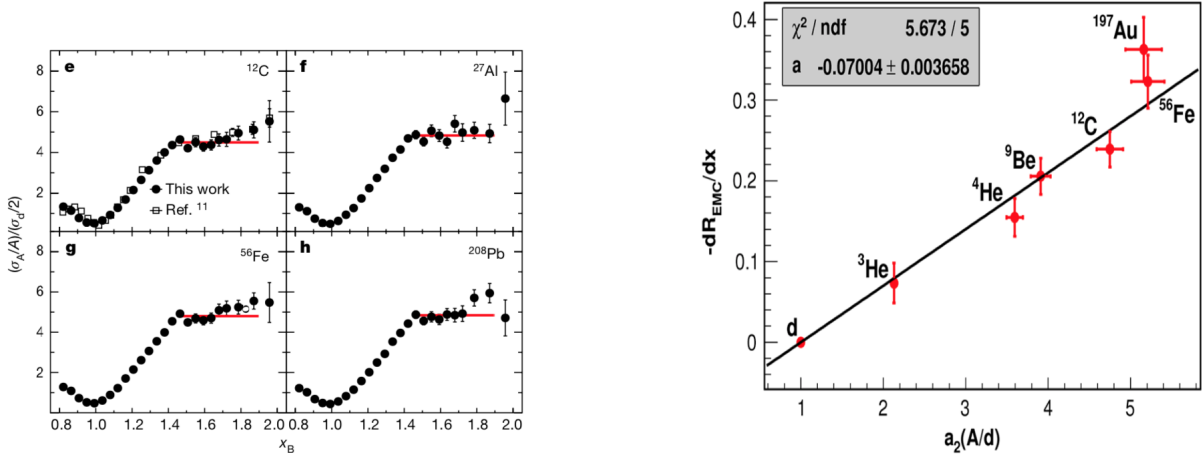


Figure 2.7: Comparison between EMC effect data and the dynamic scaling model. The data are the same as Fig.2.4. The solid line and dashed line are from [43] for different ranges of Q^2 corresponding to the SLAC and EMC data, respectively.

Short range correlation model

When the measurement of the cross section ratio $(\sigma_A/A)/(\sigma_d/2)$ is extended to $x > 1$ region, a plateau is observed at $x \gtrsim 1.45$, as shown in Fig.2.8a. The plateau have been attributed to the nucleon-nucleon short range correlations (SRC), in which two nucleons occasionally get close enough and form a NN pair such that their interactions cannot be explained by a mean field. It has been shown in electron quasi-elastic scattering experiments that SRC pairing (mostly np pairs) shifts nucleons from low-momentum nuclear states to high-momentum states with momenta greater than the nuclear Fermi momentum [44]. The amplitude of the plateau, which represents the SRC scale factor compared to the deuteron, is independent of Q^2 as well, making SRC phenomena seem related to the EMC effect. From the experimental measurements, it was found that the slope of the EMC effect is proportional to the amplitude of the SRC plateau, as shown in Fig.2.8b. As a result, the EMC effect can be understood as being driven by the high virtuality of the SRC pairs [46] or by the nuclear local density [47]. The predictions from both phenomenological models



(a) The nuclei cross section ratios in quasi-elastic region. The red line is the fit of the plateau. [44]

(b) The slope of the EMC effect plotted vs the SRC scale factor for a variety of nuclei. [45]

Figure 2.8: The short range correlations and the EMC effect.

agree with the data. While the local density model assumes the EMC effect is isospin independent, the high virtuality model assumes it is isospin dependent. Further experiments are needed to fully distinguish between the two.

The theoretical and phenomenological models mentioned above are able to qualitatively describe the EMC effect data. However, no clear evidence is found yet to support any of the microscopic features assumed by the models. In addition, it is hard for the theoretical models to agree with the EMC effect data without spoiling other relevant nuclear properties.

2.3 The MARATHON experiment

Considering the importance for the determination of the nucleon structure function ratio F_2^n/F_2^p at large x ($x > 0.7$), and the large uncertainty for nuclear effects in the deuteron, the MARATHON experiment puts forward a novel method. Instead of using a deuteron target, it performs electron deep inelastic scattering on the tritium (^3H) and helium-3 (^3He) targets over the x range from 0.17 to 0.82. The cross section for the scattering process is determined by the nuclear structure

functions:

$$\frac{d^2}{d\Omega dE'}(E, E', \theta) = \frac{4\alpha^2 E'^2}{Q^4} \cos^2\left(\frac{\theta}{2}\right) \left[\frac{F_2(\nu, Q^2)}{\nu} + \frac{2F_1(\nu, Q^2)}{M} \tan^2\left(\frac{\theta}{2}\right) \right] \quad (2.20)$$

where α is the fine-structure constant, E is the incident electron energy, E' and θ are the scattering energy and angle of the scattered electron. The structure function of ${}^3\text{H}$ and ${}^3\text{He}$ can be extracted from the experimental cross sections. Then the ratio F_2^n/F_2^p is extracted from the ratio $F_2^{3\text{H}}/F_2^{3\text{He}}$ (introduced in Chapter 5), where it requires a theoretical prediction for the EMC effect difference between ${}^3\text{H}$ and ${}^3\text{He}$. Because ${}^3\text{H}$ and ${}^3\text{He}$ are mirror nuclei, the difference should be small. Thus, the results is expected to have much less nuclear physics model dependence than with a deuteron target. On the other hand, we also perform DIS on the deuteron target in the MARATHON experiment. So the EMC effect of ${}^3\text{H}$ and ${}^3\text{He}$ are able to be measured. It is widely accepted that the understanding of the structure functions of the simplest nuclei is the first step to a complete understanding of the EMC effect.

Chapter 3: Experimental Setup

3.1 Introduction

In order to access the high x region ($x \sim 0.83$), both W^2 and Q^2 must be sufficiently large. Conventionally, $Q^2 > 1 - 2 \text{ GeV}^2$ and $W^2 > 3 - 4 \text{ GeV}^2$ is considered as the DIS region [48]. In order to meet the requirement for deep inelastic scattering, the energy of the incident electron should be large ($\geq 8.5 \text{ GeV}$). At the same time, since the scattering cross section decreases as the incident electron energy increases, to accumulate sufficient statistics, the beam energy shouldn't be too high. Hence, the upgraded 11 GeV electron beam at Jefferson Lab (JLab) combined with a pair of identical 4.0 GeV/c High Resolution Spectrometers (HRS) in Hall A provide the best system to measure the nucleon structure functions in the large x region.

The MARATHON experiment completed data taking in the spring of 2018. During the experiment, the beam energy was kept at 10.6 GeV. The ^3He , ^3H and ^2H data were taken at 12 kinematic points, while the ^1H data was only taken at five kinematic points ($x \sim 0.2 - 0.338$). The total x range covered is from 0.2 to 0.82. A complete list of kinematic is shown in Table 3.1. The distributions of W^2 and Q^2 versus x are shown in Fig.3.1 and Fig.3.2. A $W^2 > 3 \text{ GeV}^2$ cut is applied to make sure that the scattering is in the DIS region.

The experimental setup and its calibrations will be introduced in the following sections.

3.2 Accelerator

The Continuous Electron Beam Accelerator Facility (CEBAF) at Jlab is comprised of two anti-parallel linear accelerators (linacs) linked by multiple recirculation beam lines [49]. Unlike the pulsed beam typical of ring shaped accelerators, the CEBAF accelerator is capable of sending continuous wave (CW) beam up to $200 \mu\text{A}$, resulting in high luminosity. From 1995 to 2012, the

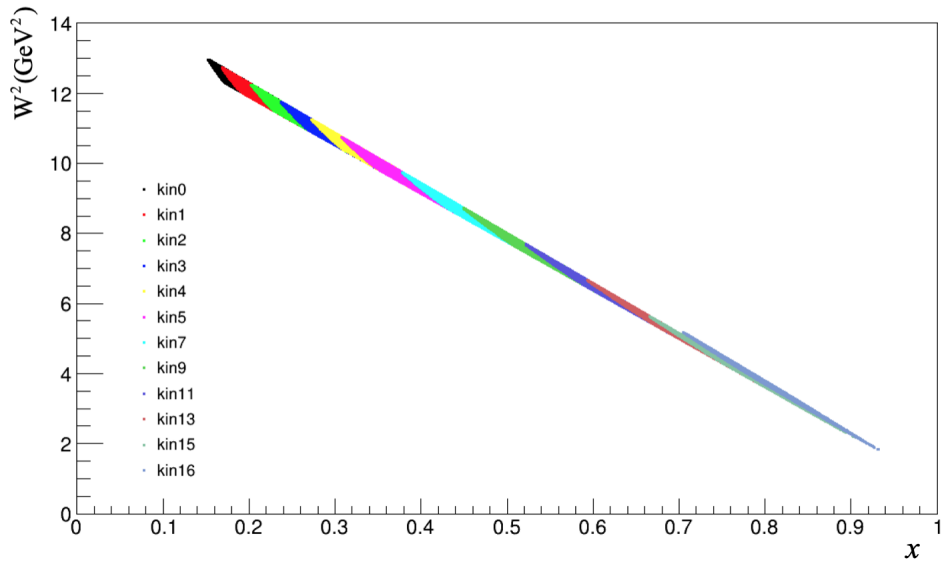


Figure 3.1: W^2 vs. x distribution in the MARATHON experiment

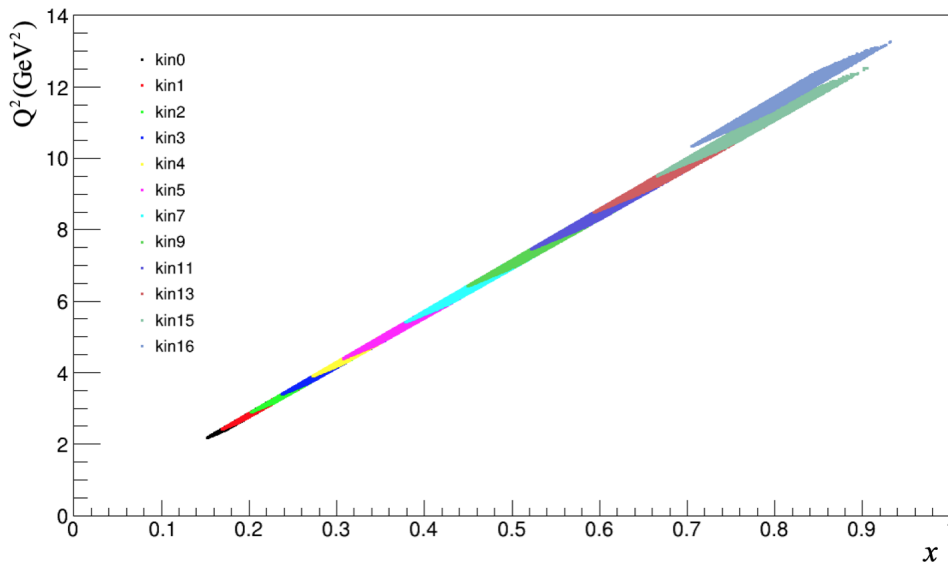


Figure 3.2: Q^2 vs. x distribution in the MARATHON experiment

Kinematics	x	W^2 (GeV ²)	Q^2 (GeV ²)	θ (°)	E' (GeV)	HRS
kin0	0.200	12.14	2.81	16.81	3.1	L
kin1	0.218	11.89	3.07	17.58	3.1	L
kin1*	0.199	12.45	2.87	17.58	2.9	R
kin2	0.258	11.32	3.63	19.14	3.1	L
kin3	0.298	10.76	4.19	20.58	3.1	L
kin4	0.338	10.20	4.76	21.93	3.1	L
kin5	0.378	9.63	5.32	23.21	3.1	L
kin7	0.458	8.51	6.45	25.59	3.1	L
kin9	0.538	7.38	7.57	27.77	3.1	L
kin11	0.618	6.26	8.70	29.81	3.1	L
kin13	0.698	5.13	9.82	31.73	3.1	L
kin15	0.778	4.00	10.95	33.55	3.1	L
kin16	0.818	3.51	11.82	36.12	2.9	R

* Kin1 RHRS data is used for RHRS calibration only. It's not included in the physics analysis.

Table 3.1: The kinematics of the MARATHON experiment

CEBAF was running in a 6 GeV configuration. It delivered electron beams up to 6 GeV to three experimental halls (Hall A, B, C). In 2017, JLab completed the 12 GeV upgrade project by largely making use of the existing CEBAF. During the 12 GeV upgrade, 5 high performance cryomodules were added in each linac, and a new arc was added for the newly built experimental Hall D. The schematic of the upgrade is shown in Fig.3.3.

A detailed diagram of the accelerator is shown in Fig.3.4. The electron beam, which can be polarized or unpolarized, is produced at the injector by illuminating a photocathode and the beam is then injected into the north linac. The recirculating beam lines send the beam multiple times through the linac, where the electron gains around 1.1 GeV energy in each pass. After passing through the south linac, the beam is directed to one of the experimental halls (Hall A, B, C) or sent through for additional recirculation. Since there are five recirculation beam lines in the east arc, the beam energies available to experimental Halls A, B, and C are 2.2 GeV, 4.4 GeV, 6.6 GeV, 8.8 GeV and 11 GeV, which are called energy pass 1, 2, 3, 4, and 5. The accelerator can deliver the first four passes to a single hall. The fifth pass can be delivered to all four halls simultaneously. With the newly added arc in the west arc, the fifth pass electron sent to Hall D is accelerated one

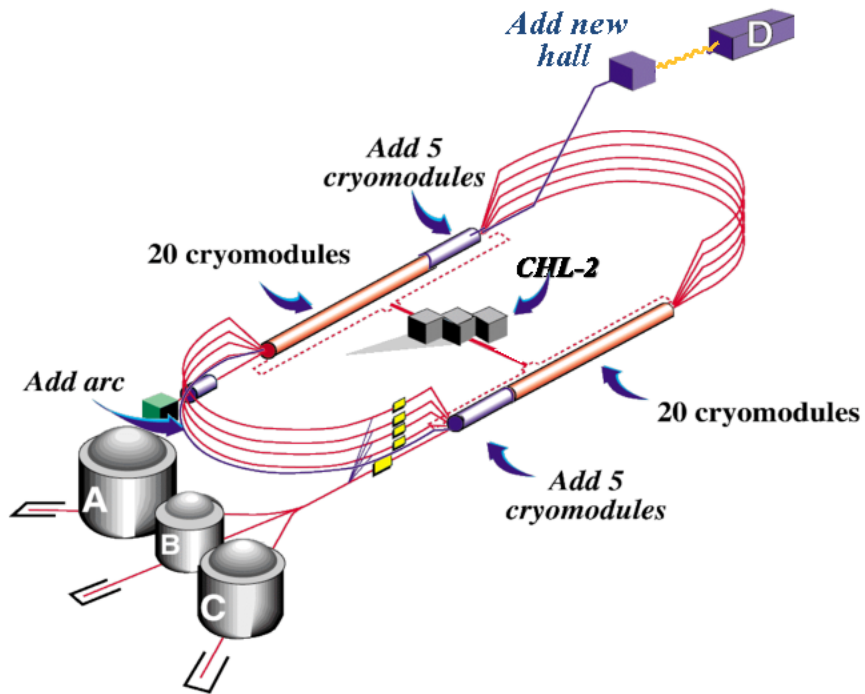


Figure 3.3: CEBAF 12 GeV upgrade schematic

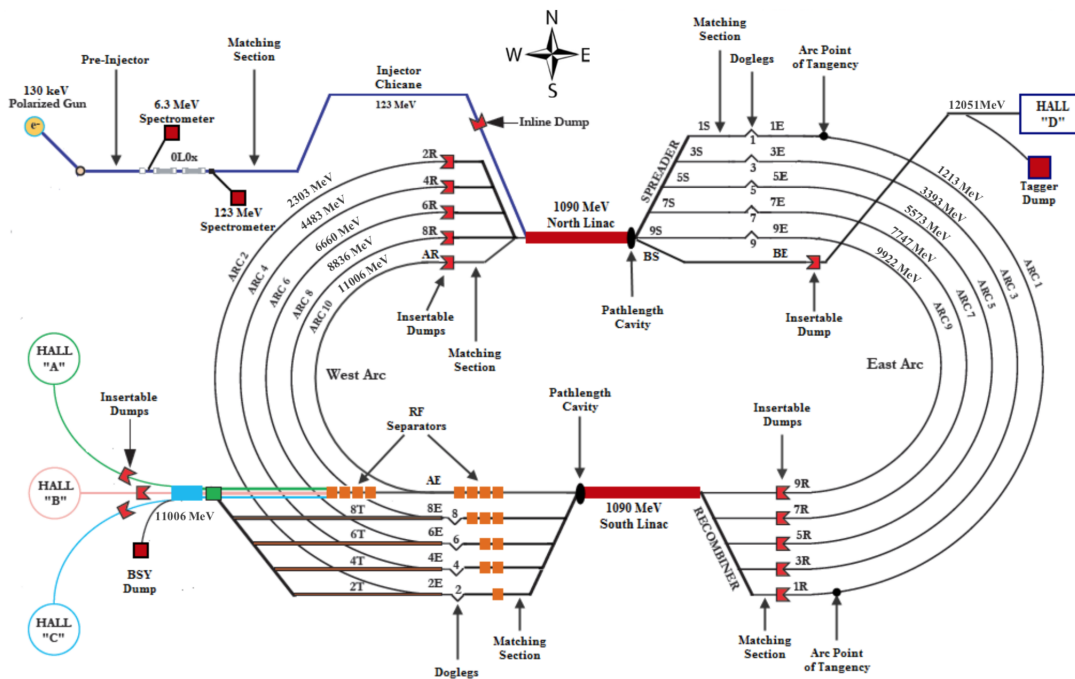


Figure 3.4: CEBAF overview [50]

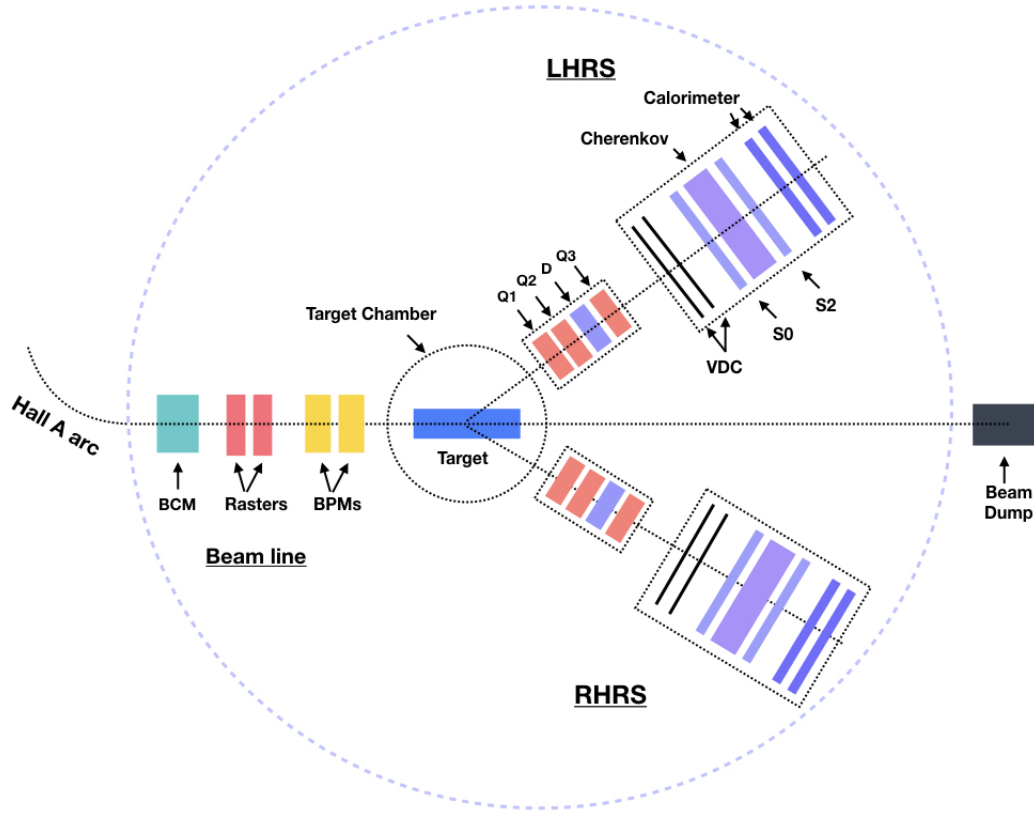


Figure 3.5: Hall A configuration during the MARATHON experiment

more time through the north linac. The beam energy for Hall D is around 12 GeV, and it is used to generate a 9 GeV photon beam for hadron spectroscopy study.

3.3 Hall A overview

The basic layout of Hall A during the MARATHON experiment is shown in Fig.3.5. The beam line transports the beam onto the target. Then the two HRS and the detector packages are used to detect the scattered electrons, while the remaining beam goes to the beam dump. Details of these devices are discussed in the following sections.

3.4 Hall A arc and beam line

At the end of the south linac, the beam is extracted to transport lines and then deflected into the Hall A arc. The Hall A arc then bends the beam into the Hall A beam line. The arc is also

used for the beam energy measurement. After the arc, the beam is essentially undeflected onto the target. Along the Hall A beam line, there is a Beam Current Monitor (BCM), a pair of rasters and two Beam Position Monitors (BPMs). These elements are necessary to transport the electron beam onto the target and simultaneously monitor the accuracy of the beam energy, current and position.

3.4.1 Beam energy measurement

The absolute beam energy can be measured using the curvature of the arc. The Hall A arc is a composite of eight dipoles interspersed with quadrupoles and sextupoles. The nominal bend angle of the beam in the arc section is 34.3° , (see Fig.3.6). The concept behind the measurement is that the momentum of the beam (p) is proportional to the product of the field integral of the eight dipoles ($\int \vec{B} \cdot d\vec{l}$) and the net bend angle through the arc section (θ):

$$p = k \frac{\int \vec{B} \cdot d\vec{l}}{\theta} \quad (3.1)$$

where $k=0.299792 \text{ GeV rad T}^{-1} \text{ m}^{-1}/c$ [51]. The magnetic field integral of the bending elements (eight dipoles) is measured based on a reference magnet (9th dipole), and the actual bend angle can be measured either when the beam is in the dispersive or achromatic mode. In the dispersive mode, only dipoles are turned on. The bend angle is determined by performing harp scans with a set of wire scanners located at the entrance and exit of the arc section. The achromatic mode occurs when both dipoles and multipoles are turned on to keep the beam size optimal for production data. The bend angle is then determined by the beam position monitors along the arc. The accuracy of the measurement in the dispersive mode ($\delta E_{beam}/E_{beam} \sim 2 \times 10^{-4}$) is better than that in achromatic mode ($\delta E_{beam}/E_{beam} \sim 5 \times 10^{-4}$), but it is an invasive measurement. During a harp scan, the harps move across the beam allowing for a precise measurement of the beam position.

The beam energy inserted in the data stream for each run is measured relative to a nominal momentum p_0 , which is calibrated to the absolute measurement. Knowing the beam positions along the arc and the currents of the magnets, the deviation from the central momentum δp is

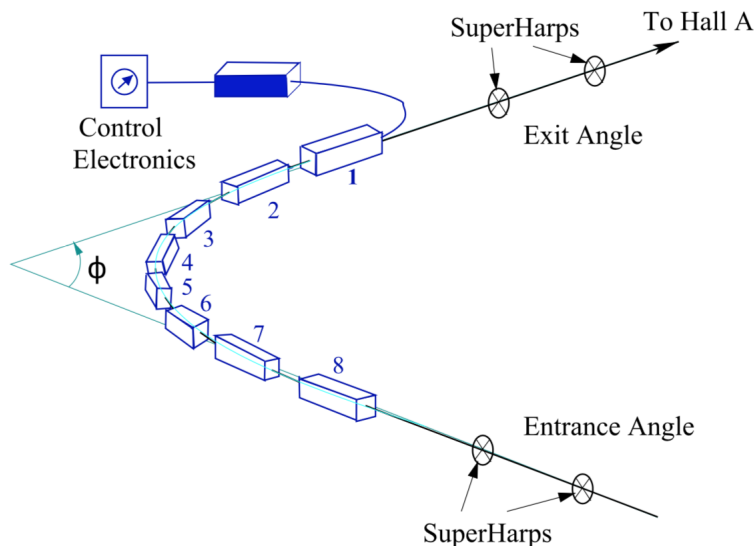


Figure 3.6: Hall A arc section

determined. The beam energy becomes $p_0 + \delta p$. The precision of this approach is around 5×10^{-4} .

The Arc method was performed multiple times during the Hall A GMP experiment, which took data at each beam energy pass (just prior to the MARATHON experiment). A comparison between the beam energy of pass 1, 3, 4, and 5 from Arc method and the relative method can be found in the Table 2.2 of Ref. [52]. The results show good agreement.

3.4.2 Beam Current Monitor

The Beam Current Monitor (BCM) is designed for a stable, low-noise, non-interfering beam current measurement [51]. It includes an Unser monitor, two RF cavities and associated electronics. Both the Unser monitor and the two RF cavities can be used to determine the current absolutely. The Unser monitor is a Parametric Current Transformer, which responds to the passed DC current with good linearity. The gain of the Unser can be calibrated by passing a known DC current from the current supplier in the counting house to a wire inside the beam pipe. The nominal output is $4 \text{ mV}/\mu\text{A}$. This level output is sent to a Voltage-To-Frequency (VTOF) converter whose output frequency is proportional to the input DC voltage level and then fed to the scalers. While the gain of the Unser monitor is stable within 0.1%, its offset drifts significantly on a time scale of

several minutes. Therefore, it cannot be used to continuously monitor the beam current. Instead, the Unser monitor provides an absolute reference during the calibration of the two RF cavities.

Two cylindrical RF cavities are located on either side of the Unser Monitor. They are tuned to the frequency of the beam (1.497 GHz) with a large loop antenna inside the cavity. When beam passes through the cavity, the output signals from the loop antenna is proportional to the beam current. The output of each RF cavities is split into two parts. One part goes to a 1 MHz down converter, as the frequency of the output signal is 1.497 GHz. Then the signal is sent to three amplifiers ($\times 1$, $\times 3$, $\times 10$), each of which covers a different linear region, so that the total linear region for current is from about $3 \mu\text{A}$ to $200 \mu\text{A}$. The amplifiers outputs are sent to an RMS-to-DC converter, and the resulting analog DC voltage is sent to a VTOF converter. These signals are then fed to scalers and inserted into the data stream. The other part of the RF cavity output is sent to a digital receiver which covers the full current range with high linearity. Its output is also sent to scalers and inserted in the data stream. The schematic of BCM is shown in Fig.3.7.

The gain and offset of the RF cavity can be measured by passing through an electron current with the measurement from Unser monitor as an absolute reference. Then the time-accumulated charge can be calculated from the scaler counts:

$$Q = I \cdot t = (\text{gain} \cdot \frac{\text{BCM counts}}{t} + \text{offset}) \cdot t \quad (3.2)$$

where I is the beam current that is proportional to the BCM rate, and $t = \frac{\text{clock counts}}{f_0}$. A clock signal with frequency $f_0 = 103700 \text{ Hz}$ is sent to both spectrometers. BCM and clock signals are counted by scalers. In the data analysis, the measurement from the down stream digital receiver is used.

3.4.3 Raster and Beam Position Monitor

The beam size from the accelerator is about hundred micro-meters [51]. It can cause damage to the target cell at high currents. To minimize this, the electron beam is usually rastered to a diameter of a few mm. The raster is a pair of horizontal (X) and vertical (Y) dipoles which deflect the beam

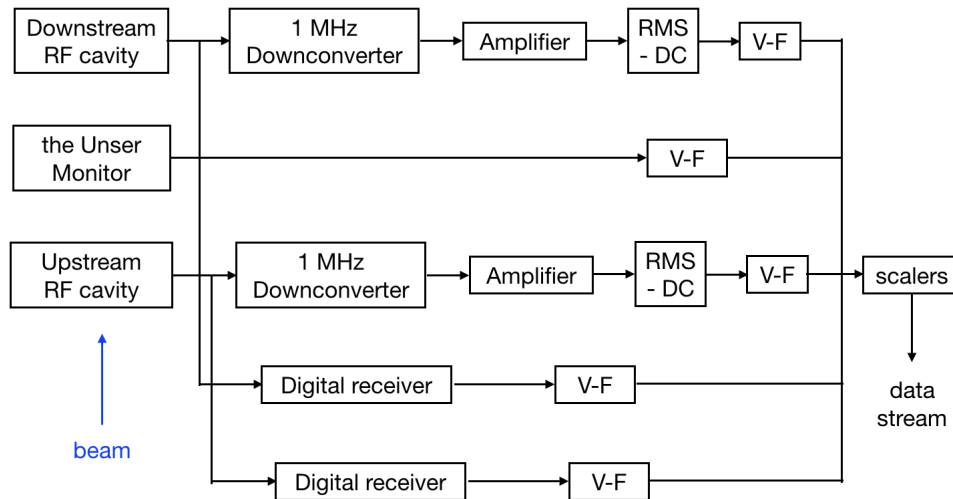


Figure 3.7: Beam Current Monitors [53]

at 25 kHz in the X and Y directions. The ratio of frequencies f_x/f_y should be an irrational number in order to get a Lissajous pattern, so that the beam is deflected uniformly in every direction. Due to the high beam energy of the MARATHON experiment, two rasters are synchronized to produce a 2 mm \times 2 mm square pattern. It's shown in Fig.3.8.

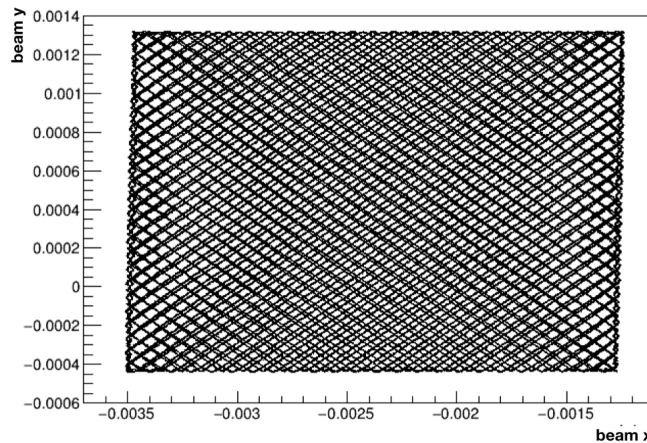


Figure 3.8: Rastered beam y vs. beam x

After the rasters, two Beam Position Monitors (BPMs) and two wire scanners (superharps) are located upstream of the target. All are used to measure the beam position absolutely and the beam direction is then extracted from the pair. The design of superharps is shown in Fig.3.9. The

superharps positions are surveyed with respect to the Hall A coordinates at regular intervals and the results are reproducible at the level of $200\ \mu\text{m}$ [51]. Each harp contains three wires which can be moved in and out of the beam line by a motor driver at a known speed. A peak signal is generated when a wire crosses the beam. Therefore, from the peak signal's relative position and the surveyed harp's absolute position, the absolute beam position can be determined. This method is invasive. It cannot be used during data taking. Instead, it provides an absolute reference to the BPMs calibration.

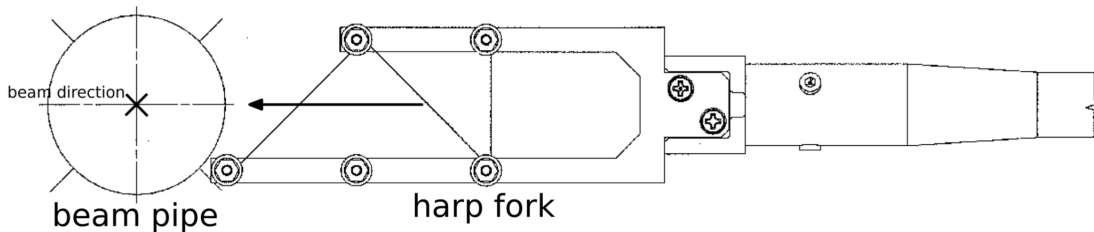


Figure 3.9: Superharp design

The BPM consists of a 4-wire antenna array of open ended thin wire striplines tuned to the fundamental RF frequency of 1.497 GHz of the beam [54]. When beam passes through the BPM, the signal amplitude picked up by each antenna is related to the relative beam position and direction. The BPMs data is recorded event by event in the data stream. During the BPMs calibration, the beam position (with raster off) is first determined by a harp scan, and then the absolute measurement from the superharps is used to calibrate the BPMs data that is taken simultaneously.

Since the BPMs only provide the average beam position, the event-by-event beam position has to be constructed by combining the information from BPMs and rasters. The rasters are calibrated by using the BPMs as a reference or a carbon hole target of which the size is known. A similar detailed calibration procedure of superharps, BPMs and rasters is found in Ref.[55].

3.5 Target

The target system includes five cells of gaseous ^3H , ^3He , ^2H , ^1H and an empty cell for background studies. Several solid targets are hung below the cells and used for calibrations. The target

ladder is shown in Fig.3.10 and a list of targets used in the MARATHON experiment and their purpose are shown in Table 3.2.

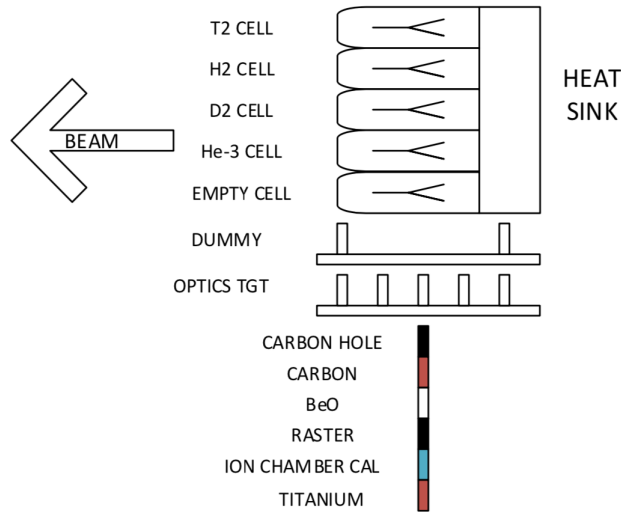


Figure 3.10: Target ladder

Target name	Materials	Thickness (mg/cm^2)	Purpose
Tritium	^3H gas	85.099 ± 0.825	Production
Helium3	^3He gas	53.3752 ± 0.57	Production
Deuterium	^2H gas	142.15 ± 0.788	Production
Hydrogen	^1H gas	70.8 ± 0.3974	Production
Empty cell	Aluminum 7075	-	Background study
25 cm Dummy	Aluminum 7075	-	Background study
Optics	Carbon 99.95%	(muti-foils)	Optics study
Carbon hole	Carbon 99.95%	-	Raster calibration and beam alignment
Carbon	Carbon 99.95%	(single foil)	Raster calibration

Table 3.2: A list of targets used in MARATHON

Tritium is radioactive. For safety reason, the amount of tritium in the target was limited to a radioactivity of approximately $1 \text{ kCi} = 37 \text{ TBq}$. A special target system was designed to minimize the safety hazards associated with the tritium target. The system consists of three layers of containment/confinement during the operation, which include a sealed target cell, a scattering chamber and the Hall itself. The target cells are of a modular design (see Fig.3.11). This design made the installation of the target system easy and allowed the tritium cell to be installed after all other tar-



Figure 3.11: Tritium target cell design

get installation activities had been completed. It also allowed the tritium cell to be filled off site at the Savannah River site tritium Enterprises (SRTE). The target ladder was put inside a sealed scattering chamber which was part of the target vacuum system. The vacuum system included a beryllium window to isolate the scattering chamber vacuum from the upstream beam line. The beryllium window needed to be considered in the beam energy loss correction. As the final layer of containment/confinement, all the doors of the Hall were locked. In case of an accidental release of tritium, an exhaust system was installed to be able to remove tritium in a controlled manner. Since the target cells are sealed, the cell assemblies are cooled by a heat sink. Coolant 15K helium from the End Station Refrigerator (ESR) is preheated to 40K and then used to cool the heat sink. This removes $\sim 15\text{W}$ of heat generated by the electron beam. The beam current allowed on the tritium cell was limited to a maximum of $22 \mu\text{A}$. A detailed description of the Hall A Tritium Target systems can be found in Reference [56].

The gas target thickness is one of the dominant scale uncertainties in cross section ratio extraction. The target thickness of ^2H , ^1H are determined by the NIST table using equation of states. For ^3He and ^3H , the temperature and pressures during the fill at room temperature are used assuming the ideal gas law. The relative uncertainty for the target thickness is 0.6% for ^1H and ^2H , 1.1% for ^3He , and 1% for ^3H [57].

3.6 Hall A High Resolution Spectrometers

In order to isolate different reaction channels, two identical HRS were constructed to vertically bend charged particles and determine their momenta with a high momentum resolution (at

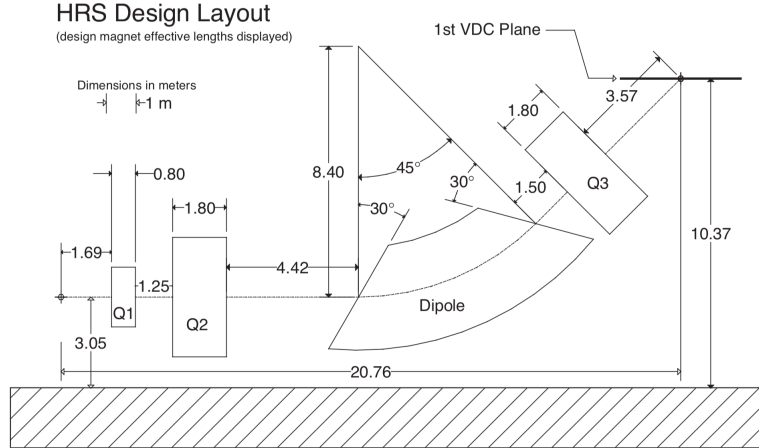


Figure 3.12: The layout of a HRS (side view)(the numbers in the plot are out of date)

the 10^{-4} level) over the range 0.8 to 4.0 GeV/c. The basic layout is shown in Fig.3.12. This figure corresponds to the original design of a HRS. The numbers on the plot have been changed somewhat over the years. For example, the Q1 quadrupoles in both spectrometers have been replaced in 2016. Each of the HRSs includes a pair of superconducting quadrupoles followed by an indexed dipole magnet which includes additional focusing. Following the dipole is a third superconducting quadrupole that is identical to the second one. The left HRS (LHRS) magnets operated as expected, while the right HRS (RHRS) was only able to reach a maximum central momentum of about 3.16 GeV/c, due to complications caused by an internal short in the dipole. During the MARATHON experiment, the RHRS could only operate and remain stable at 2.9 GeV/c. The main design characteristics of the HRS are shown in Fig.3.13 [51].

3.6.1 Scattering angle and momentum measurement

To extract the differential cross section, the scattering angle and the scattering momentum need to be measured. If the position and direction of the scattered particle (x_{tg} , y_{tg} , θ_{tg} , ϕ_{tg} , see Fig.3.15) at the interaction vertex are determined, the scattering angle can be calculated by combining θ_{tg} and ϕ_{tg} (measured relative to the central ray of the spectrometer), and the spectrometer central

Configuration	QQD _n Q vertical bend
Bending angle	45°
Optical length	23.4 m
Momentum range	0.3–4.0 GeV/ <i>c</i>
Momentum acceptance	−4.5% < δ <i>p/p</i> < + 4.5%
Momentum resolution	1 × 10 ^{−4}
Dispersion at the focus (<i>D</i>)	12.4 m
Radial linear magnification (<i>M</i>)	−2.5
<i>D/M</i>	5.0
Angular range	
HRS-L	12.5–150°
HRS-R	12.5–130°
Angular acceptance	
Horizontal	± 30 mrad
Vertical	± 60 mrad
Angular resolution	
Horizontal	0.5 mrad
Vertical	1.0 mrad
Solid angle at δ <i>p/p</i> = 0, <i>y</i> ₀ = 0	6 msr
Transverse length acceptance	± 5 cm
Transverse position resolution	1 mm

Figure 3.13: Main design characteristics of the HRS.

angle θ_0 between the beam line and the spectrometer nominal central ray [51]:

$$\theta_{scat} = \arccos\left(\frac{\cos(\theta_0) - \phi_{tg}\sin(\theta_0)}{\sqrt{1 + \theta_{tg}^2 + \phi_{tg}^2}}\right) \quad (3.3)$$

where θ_0 can be obtained either from the spectrometer survey or data from the Experimental Physics and Industrial Control System (EPICS). Since a survey requires hours of beam downtime, it is impossible to be performed for each run. In the MARATHON experiment, θ_0 and the spectrometer mispointing offsets are determined by three linear variable differential transformer (LVDT) and an encoder located around the spectrometer. Their values are monitored by EPICS and inserted in the data stream every few seconds.

Similarly, if the relative momentum fractional difference δ for the scattered particle is measured, it can be used to calculate the absolute scattering momentum p :

$$p = p_0(1 + \delta) \quad (3.4)$$

where p_0 is the central momentum of the spectrometer. The central momentum p_0 is determined by multiplying the central magnetic field measured by NMR probes in the dipole by a calibration constant [58]. This spectrometer central momentum was cross checked with using constants determined by performing elastic scattering on ^{12}C target and missing-energy measurements of the $1p_{1/2}$ state in the $^{12}\text{C}(e,e'p)$ reaction [59].

While θ_0 and p_0 are determined by EPICS data at the beginning of each run, x_{tg} , y_{tg} , θ_{tg} , ϕ_{tg} and δ are measured on an event by event basis. The trajectory of a charged particle passing through a series of magnets is represented by a vector $\vec{x} = (x, y, \theta, \phi, \delta)$ [51]. The interaction vertex at the spectrometer entrance can be reconstructed from the coordinates of the scattered particles measured at the focal plane through an optics matrix. The HRS magnets tuning of the MARATHON experiment is the same as the GMP experiment, and they have optics data taken around 3.1 GeV/c. To save beam time, we use the optics matrix from the GMP experiment in the data analysis [52]. While part of the target boiling data was taken in 2017 with slightly different magnets tuning, the optics matrix used in that part of analysis is from our optics calibration. The basic idea of optics calibration is introduced in the following sections, while the details are found in [52] and [60].

3.6.2 Coordinate systems and optics matrix

The variables used in the optics calibration are measured in different coordinate systems. A short overview of five commonly used coordinate systems is presented here. A more detailed description can be found in [60].

- **Hall Coordinate System (HCS)** The origin of the HCS is at the center of the hall, which is defined by the intersection of the beam line and the vertical symmetry axis of the target system. \hat{z} is along the beam line and points to the beam dump. \hat{y} is vertically up. See Fig.3.14.
- **Target Coordinate System (TCS)** Each of the two spectrometers has its own TCS. \hat{z} is along the central ray of the spectrometer and points away from the target. \hat{x} is vertically

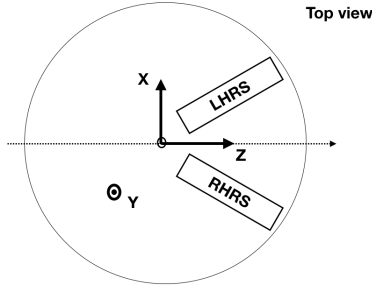


Figure 3.14: Hall coordinate system (top view)

down. The origin of TCS is defined to be the point on \hat{z} axis at a distance L from the sieve slit surface of the spectrometer, where L is the distance from the hall center to the midpoint of the central sieve slit hole. See Fig.3.15. Ideally, the origin of TCS should be at the hall center.

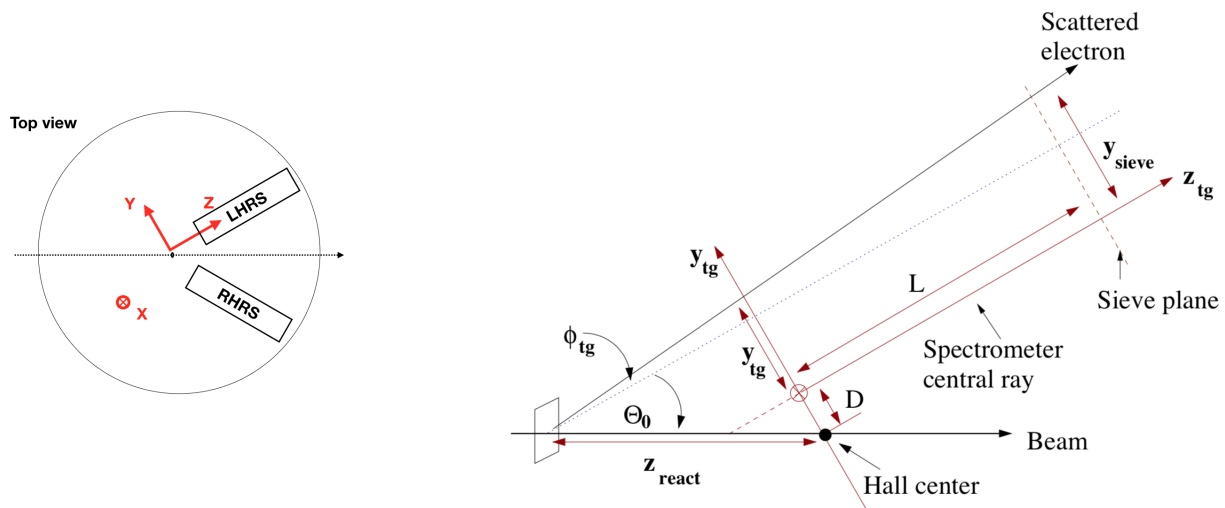


Figure 3.15: Target coordinate system (top view)

- **Detector Coordinate System (DCS)** The intersection of wire 184 of the VDC1 U1 plane and the perpendicular projection of wire 184 in the VDC1 V1 plane onto the VDC1 U1 plane defines the origin of the DCS. (VDC will be introduced in section 3.7.1). \hat{z} is perpendicular to the VDC plane pointing vertically up. \hat{x} is along the long symmetry axis of the VDC. The \hat{x} - \hat{z} plane is also called dispersive plane. See Fig.3.16.
- **Transport coordinate system (TRCS) at the focal plane** Rotating the DCS clockwise

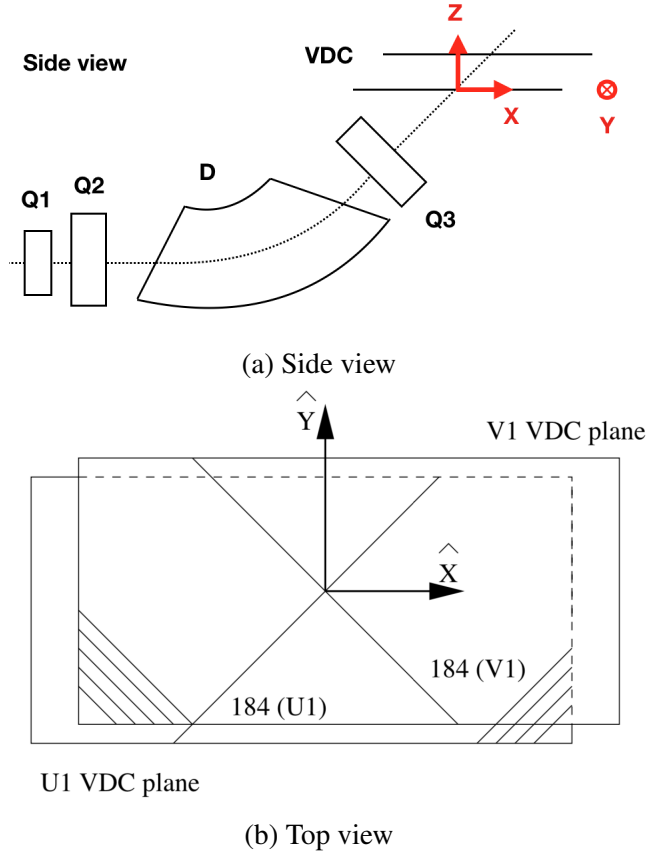


Figure 3.16: Detector coordinate system

around its y-axis by 45° generates the TRCS. See Fig.3.17.

- **Focal plane Coordinate System (FCS)** To simplify the optics calibration, a rotated coordinate system FCS is defined. It's obtained by rotating the DCS around its y-axis by an angle ρ , where ρ is the angle between the local central ray¹ and the \hat{z} axis of the DCS. So the \hat{z} axis of the FCS rotates as a function of the fractional relative momentum $\frac{\Delta p}{p}$. See Fig.3.18.

For each event, x_{det} , y_{det} , θ_{det} and ϕ_{det} are measured by VDC in DCS. Then these focal plane variables are corrected for any detector offsets from the ideal central ray of the spectrometer to obtain x_{fp} , y_{fp} , θ_{fp} and ϕ_{fp} in FCS. The transform formula can be found in [60]. These observables are used to calculate x_{tg} , y_{tg} , θ_{tg} , ϕ_{tg} and δ in TCS. In optics calibration (raster off), in order to reduce the unknowns, x_{tg} is effectively fixed at zero by requiring that the beam position on target

¹The ray with $\theta_{tg} = \phi_{tg} = 0$

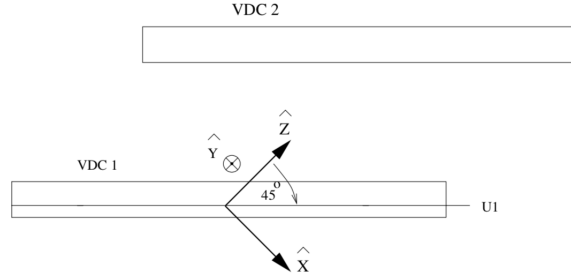


Figure 3.17: Transport coordinate system (side view)

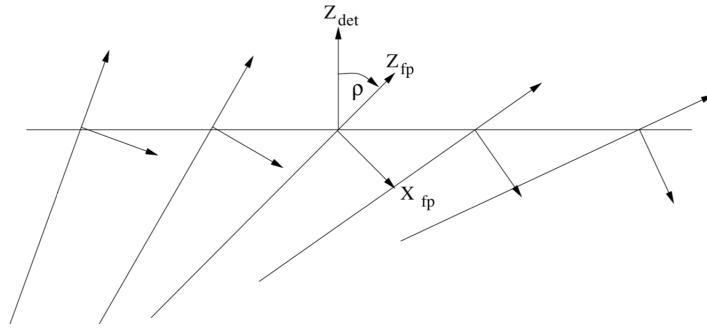


Figure 3.18: Focal plane (rotated) coordinate system (side view)

is within $250 \mu\text{m}$ of the origin of HCS. Then a set of tensors (up to fifth order) Y_{jkl} , T_{jkl} , P_{jkl} and D_{jkl} link the focal plane coordinates to target coordinates according to:

$$y_{tg} = \sum_{j,k,l} Y_{jkl} \theta_{fp}^j y_{fp}^k \phi_{fp}^l \quad (3.5)$$

$$\theta_{tg} = \sum_{j,k,l} T_{jkl} \theta_{fp}^j y_{fp}^k \phi_{fp}^l \quad (3.6)$$

$$\phi_{tg} = \sum_{j,k,l} P_{jkl} \theta_{fp}^j y_{fp}^k \phi_{fp}^l \quad (3.7)$$

$$\delta = \sum_{j,k,l} D_{jkl} \theta_{fp}^j y_{fp}^k \phi_{fp}^l \quad (3.8)$$

where Y_{jkl} , T_{jkl} , P_{jkl} and D_{jkl} are polynomials in x_{fp} . For example,

$$Y_{jkl} = \sum_{i=0}^m C_i x_{fp}^i. \quad (3.9)$$

The $C_i^{Y_{jkl}}$, $C_i^{T_{jkl}}$, $C_i^{P_{jkl}}$ and $C_i^{D_{jkl}}$ are the optics matrix elements which are optimized in the optics calibrations.

3.6.3 Optics calibrations

The calibrations for the optics matrix elements of geometric variables y , θ and ϕ are done by performing DIS scattering on a multi-foil target, with a sieve slit placed in front of the spectrometer and the raster turned off. The sieve is about an inch thick made of Tungsten with holes drilled in a grid pattern, see Fig.3.19a. The scattered electrons are stopped by the metal, except those whose tracks pass through the holes and reach the focal plane detectors. In practice, it is not convenient to use the basic variables y_{tg} , θ_{tg} , ϕ_{tg} , since the y_{tg} varies with ϕ_{tg} . On the other hand, the interaction position z_{react} along the beam corresponds to the z position of the foil target in HCS. The vertical and horizontal positions at the sieve plane in TCS, x_{sieve} and y_{sieve} (see Fig.3.15), represent the positions of the holes in the sieve-slit collimator. These three variables are uniquely determined for the given targets and the sieve slit. They are linked to the basic variables through the equations:

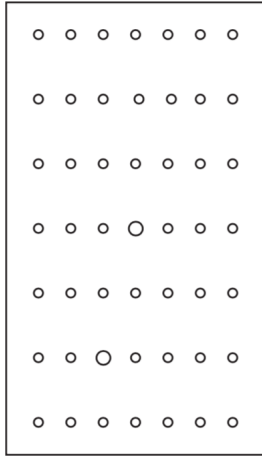
$$z_{react} = -(y_{tg} + D) \frac{\cos(\arctan\phi_{tg})}{\sin(\theta_0 + \arctan\phi_{tg})} + x_{beam} \cot(\theta_0 + \arctan\phi_{tg}) \quad (3.10)$$

$$y_{sieve} = y_{tg} + L\phi_{tg} \quad (3.11)$$

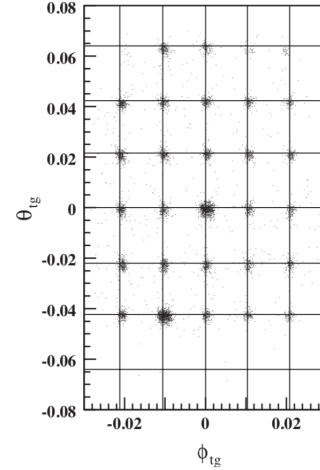
$$x_{sieve} = x_{tg} + L\theta_{tg} \quad (3.12)$$

where x_{beam} is the beam position in HCS measured by BPM. x_{tg} is calculated using the beam position in the vertical direction, the vertical displacement of the spectrometer from its ideal position,

θ_{tg} and z_{react} . Once z_{react} , x_{sieve} , y_{sieve} are known from the survey, and x_{det} , y_{det} , θ_{det} , ϕ_{det} are measured by the focal plane detectors, the optics matrix elements are determined from Eq.(3.5), Eq.(3.6) and Eq.(3.7) by a χ^2 minimization procedure. An example of reconstructed sieve pattern after calibration is shown in Fig.3.19b.



(a) Geometric configurations of the sieve slit



(b) Reconstructed configuration of the sieve slit

Figure 3.19: The sieve slit collimator

The δ calibration in the GMP experiment was done by performing elastic scattering on a liquid hydrogen target with sieve removed. The raster was turned on to protect the target. The central momentum of the spectrometer was adjusted from -4% to 4% in steps of 2%, so that the elastic peak moves across the focal plane and covers the whole momentum acceptance. By comparing the scattering momentum calculated from the elastic scattering formula with that reconstructed from eq.(3.8), the optics matrix elements for δ are determined.

3.7 Detector package

The detector packages for the two spectrometers are designed to perform various functions including providing triggers to the data acquisition (DAQ) system and characterizing the charged particles passing through the spectrometer. In the MARATHON experiment, the detector package includes:

- A pair of Vertical Drift Chambers (VDCs) to provide tracking information;
- Two scintillators (s0 and s2) to provide timing information and generate the main trigger to the DAQ;
- A gas Cherenkov and two-layer shower detectors for electron identification.

The configurations of the detector packages in both spectrometers are shown in Fig.3.20. They are almost identical except for the shower detectors.

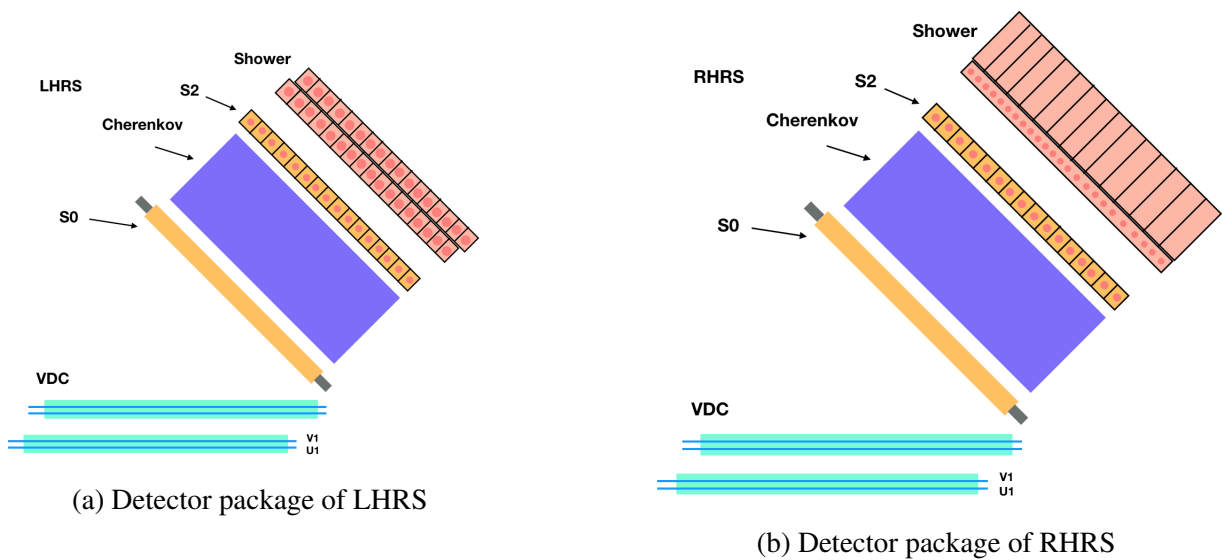


Figure 3.20: Detector package in MARATHON

3.7.1 Vertical Drift Chamber (VDC)

A pair of VDCs in each HRS provides the tracking information (position and direction) of the scattered particle at the focal plane. Each VDC is composed of two wire planes in a standard UV configuration—the wires of each successive plane are perpendicular to one another. The VDC lies in the laboratory horizontal plane. The wires are inclined at an angle of 45° with respect to the dispersive and non-dispersive directions. Nominally, the particle trajectory crossing the wire plane is at an angle of 45° . See Fig.3.21.

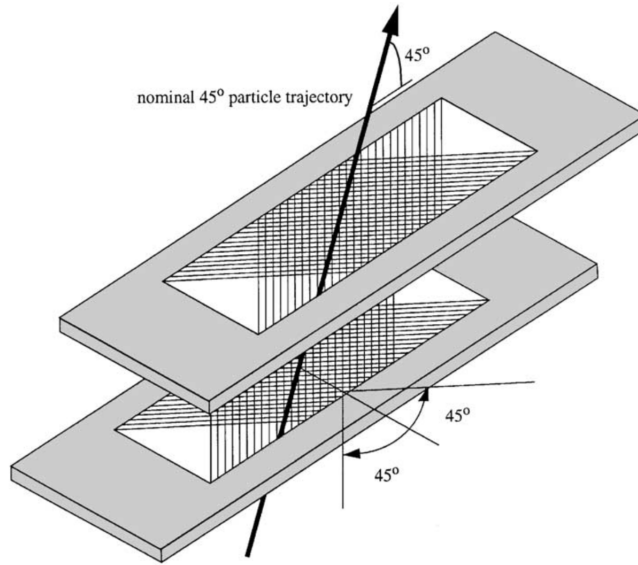


Figure 3.21: Schematic layout of VDCs

For a single wire plane, the sense wires are connected to ground and are placed horizontally between two high voltage planes. This configuration generates a uniform electric field in the vertical direction (the solid line in Fig.3.22). The chamber is filled with a gas mixture of argon and ethane. Charged particles passing through the chamber gas cause ionization. In the electric field, the ionized electrons travel from the trajectory to the sense wires along the path of least time (the arrowed lines in Fig.3.22). When an electron is collected by a sense wire, the wire generates a signal. The timing of this signal is measured by TDC, which is referenced to the main event trigger. This time can be converted into a perpendicular distance from the trajectory to the wire plane (the dot/dashed line in Fig.3.22). By performing a linear fit on these drift distances, the local cross-over point Q_i and the local trajectory angle θ_{Q_i} of the track is determined for each wire plane [61]. By combining the cross-over information from the four wire planes, the position and direction of the trajectory at the first wire plane can be determined.

A single wire drift-time spectrum in common-stop mode is shown in Fig.3.23. A larger x-axis value represents a shorter time. The timing offset t_0 is due to the signal processing time and various cable lengths. Before comparing the drift time from different wires, the timing offset t_0 has to be subtracted. The variable t_0 corresponds to the value of the bin which has the largest slope on the

right side of the main peak.

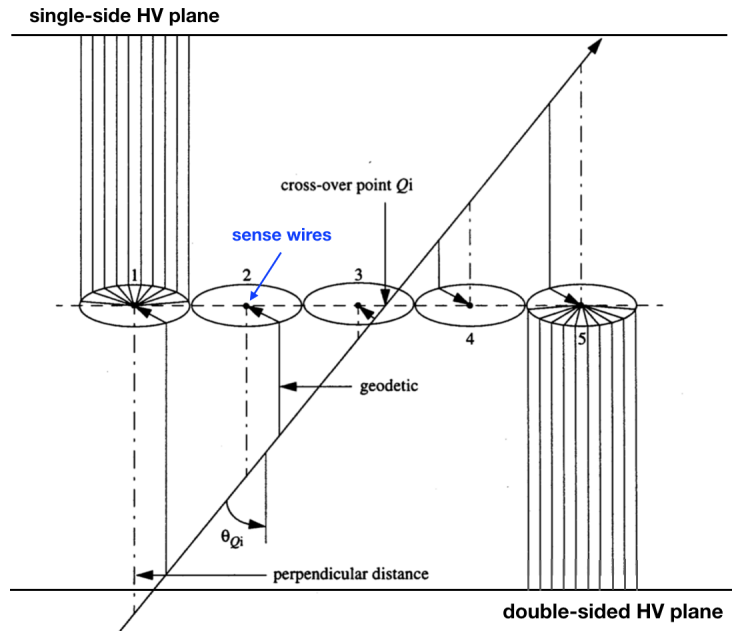


Figure 3.22: A nominal track in a wire plane

3.7.2 Scintillators

There are two scintillator planes (S0 and S2) installed in the MARATHON experiment. When a particle passes through the scintillator materials, a small flash of light is emitted and collected by the photomultiplier tubes (PMTs). The signals from the PMTs are measured by both ADCs and TDCs, and are used to generate the event trigger (see Section 3.8.1). The timing information of S0 and S2 combined with the distance between them can be used to measure the speed of particles (β). β helps distinguish a cosmic event ($\beta < 0$) from a physics event ($\beta > 0$). The timing calibration method is described in Section 3.3.3 in [52]. S0 is located just in front of the Cherenkov. It is an un-segmented scintillator plane with two PMTs on each side along the dispersive direction. See Fig.3.24a. S2 is located after the Cherenkov and is composed of 16 paddles. The paddles are arranged to provide segmentation along the dispersive direction. Each paddle is viewed by two PMTs on each side along the non-dispersive direction. See Fig.3.24b.

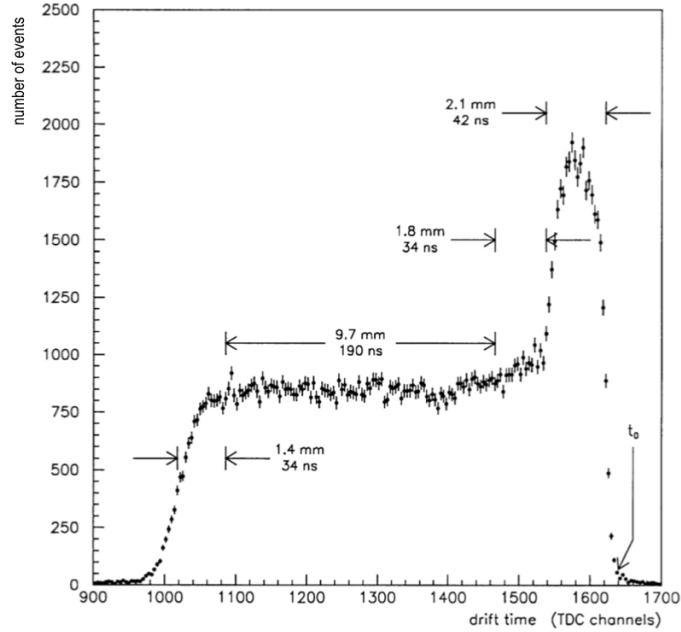


Figure 3.23: A single wire drift-time spectrum in common-stop mode [61]

3.7.3 Gas Cherenkov Detector

In the MARATHON experiment, a gas Cherenkov detector filled with CO_2 was mounted between S0 and S2. It allows for an electron identification with 99% efficiency [51]. The gas Cherenkov is used to distinguish scattered electrons from hadron backgrounds. The background is largely composed of pions generated from photopion production which can pass through the spectrometer, be reconstructed back to the target and fake being an electron.

Cherenkov radiation arises when the speed of the charged particle (v) in the detector material is faster than the speed of light in the same material ($v > c/n$). For CO_2 gas Cherenkov, the index of refraction at STP is $n=1.00041$. The threshold momentum for electron to produce Cherenkov light is $0.017 \text{ GeV}/c$, whereas for pions the threshold is $4.8 \text{ GeV}/c$ [62].

The Cherenkov detector has ten spherical mirrors with 80 cm focal length, each viewed by a PMT. The 10 mirrors are placed in front of the exit window for the detector and are arranged in two columns of 5 mirrors. The Cherenkov ring emitted by the electron is reflected by the mirrors onto the paired PMTs placed at the side of the box. See Fig.3.25. The signal from each PMT is

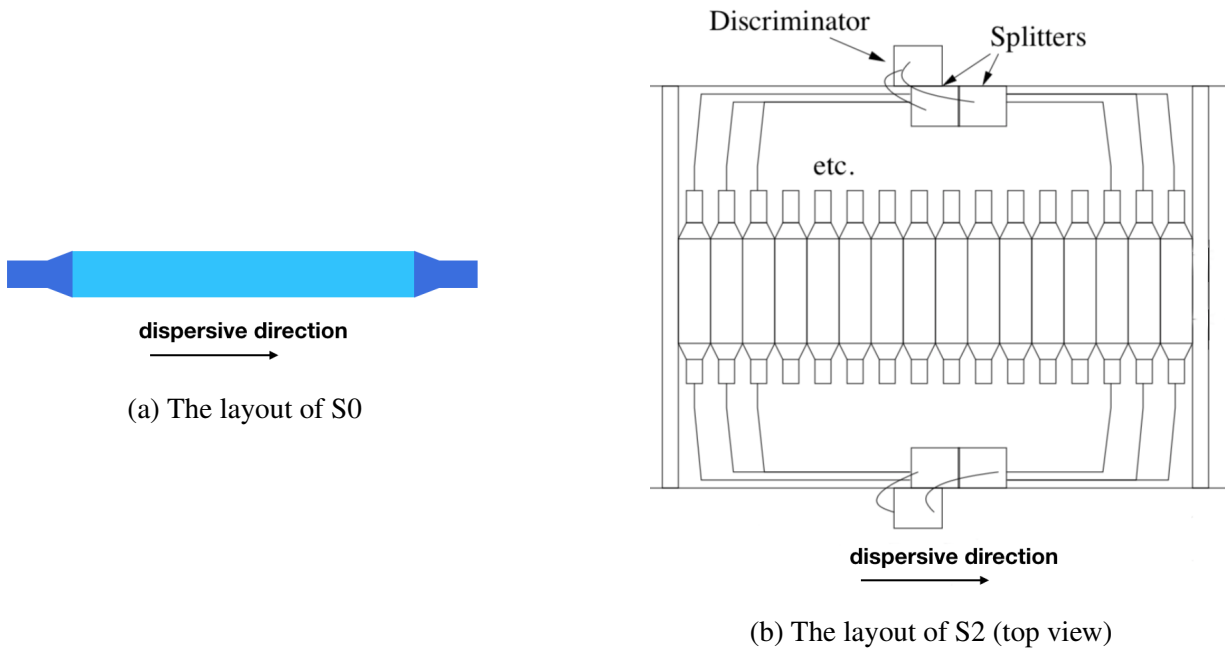


Figure 3.24: Scintillators

recorded by an ADC. The sum of the ADC values from 10 PMTs is proportional to the total number of photoelectrons collected. The length of the particle's path in the gas radiator in the LHRS is 120 cm, and 130 cm in the RHRS, leading to an average of about 12 emitted photoelectrons. Since the gain of different PMTs varies, it was calibrated for each PMT before summing. The gain of each PMT is determined by normalizing the single photoelectron peak to the same value.

While the pions does not emit Cherenkov radiation, energetic knock-on electrons produced by pions become a dominant contamination. However, in order to produce Cherenkov light that can cross the mirror and be reflected to the PMT, and generate a trigger (fire S0 and S2), the knock-on electrons have to satisfy strict conditions. Therefore, the contamination is small (about 10^{-3}) [62].

3.7.4 Shower detectors

The shower detectors provide additional particle identification (PID) information to separate electrons from backgrounds. The shower detectors are built from lead glass. Each HRS has two layers. The configurations of shower detectors in each HRS are shown in Fig.3.26. In LHRS, each

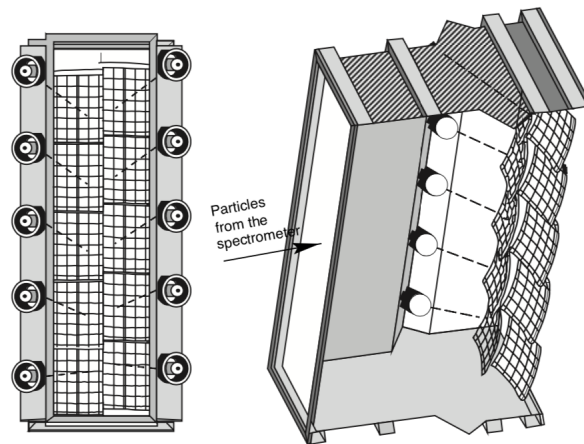


Figure 3.25: Front view and side view of Gas Cherenkov Detector

layer has $2 \times 17 = 34$ blocks and the blocks are oriented perpendicular to the tracks. In RHRS, the first layer has $2 \times 24 = 48$ blocks, and the blocks are arranged the same way as LHRS, while the second layer has $5 \times 15 = 75$ blocks and they are parallel to the tracks. Each block is viewed by a single PMT.

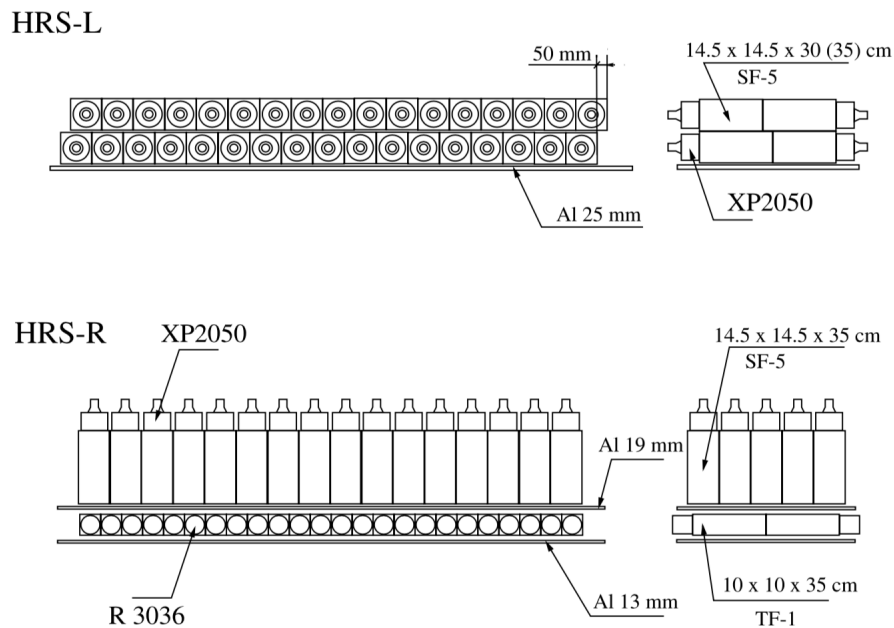


Figure 3.26: The configurations of shower detectors in LHRS and RHRS

When high energy electrons pass through the materials, they produce photons through the bremsstrahlung process; the photons then convert into electron-positron pairs which in turn emit

further energetic bremsstrahlung photons. This continues until the energy of the pair produced electrons and positrons drops below a critical energy (around 15 MeV). At the same time, the electrons and positrons produced in the cascade emit Cherenkov light which are collected by PMTs and then measured by ADCs. The total number of Cherenkov photons is proportional to the particle energy. Therefore, the sum of the ADC values of fired PMTs is proportional to the energy of the scattered electron deposited in the shower detectors. The electrons deposit most of their energy in the shower detectors. Other particles like muons and pions only deposit a small energy in the shower detectors, since the probability of the bremsstrahlung emission varies as the inverse square of the particle mass.

In the data analysis, a group of adjacent fired blocks is first identified as a cluster and the sum of their calibrated ADC values is considered as the total energy of the electron:

$$E = \sum_{i \in C} E_i = \sum_{i \in C} g_i \cdot A_i \quad (3.13)$$

where C is the set of block numbers belonging to the cluster. A_i is the pedestal subtracted ADC value of the i th block, and g_i is the calibration constant of this block. To determine the calibration constants, firstly, a bunch of "electron" events is selected by requiring a big Cherenkov sum, a good track and a relative large shower energy. Secondly, a cluster made up of the block that has the biggest ADC value and its surrounded blocks is selected in each layer. In principal, neglecting the electron mass, the total energy (E) of the two clusters should be equal to the momentum (P) of the electron which is reconstructed from the focal plane variables. Therefore, the calibration constants can be determined by minimizing the χ^2 :

$$\begin{aligned} \chi^2 &= \sum_i^N (E_{ps}^i + E_{sh}^i - P^i) \\ &= \sum_i^N \left(\sum_{j \in C_{ps}} g_j \cdot A_j^i + \sum_{k \in C_{sh}} g_k \cdot A_k^i - P^i \right)^2 \end{aligned} \quad (3.14)$$

N is the number of selected "electron" events. "ps" and "sh" are the first and second layer of the

shower detectors. After calibration, the ratio of the energy to the momentum (E/P) of electrons are close to 1 as shown in Fig.4.5.

3.8 Data acquisition

The data-acquisition (DAQ) systems for Hall A uses CODA (CEBAF On-line Data Acquisition System) developed by the JLab data-acquisition group [51]. The DAQ hardware consist mainly of commercially available electronics, including front-end Fastbus and VME digitization devices (ADCs, TDCs, scalers) to collect the data from the detectors. Besides that, the JLab developed Trigger Supervisor (TS) together with the Trigger Interface (TI) boards, Trigger Distribution (TD) boards and Signal Distribution (SD) boards are the central point for the DAQ. They distribute trigger, synchronous clock source and sync signals to the front-end electronics and monitor the BUSY signals returned from the front-end electronics [63]. For each event, which generates a trigger through logic operations by NIM modules, the TS receives the trigger and sends event readout signal through the distribution system to the TI in the front-end crates. Then, the read-out controller (ROC) gathers the data and buffers them in memory, and sends these buffers to the event builder (EB) via a network connection. The EB builds events from fragments sent by multiple ROCs and passes them to the event recorder (ER) which writes data to a local disk. Another event-transfer (ET) system allows additional data like EPICS data and scaler data to be inserted in the data stream every few seconds. Finally, everything is controlled by the RunControl process, from which users can build their own DAQ configurations, and start and stop runs.

The EPICS are used to monitor the sensors and probes of both Hall A instrumentation as well as the accelerator. The EPICS data is monitored in real time by alarm handlers and the shift crews to insure the data quality. The BCM data is recorded by scalers, as well as all the triggers and detector signals which are sent to a discriminator first and then to scalers. The scaler data can be used to monitor the real-time trigger rates, detector behaviors and calculate the DAQ dead time.

3.8.1 Triggers

Triggers are used to select the electron events, and should be loose enough to not miss a possible candidate. For this purpose, three triggers are built for each spectrometer in the MARATHON experiment. First, a possible candidate must fire both S0 and S2. As mentioned in Section 3.7.2, S0 is viewed by two PMTs as is each paddle of S2. A coincidence between two PMTs is made for S0 and each paddle of S2. The logical OR of the sixteen S2 paddles signals is formed as the S2 signal. The first trigger (T1/T4 for LHRS/RHRS) which is also the main trigger is the logical AND of the S0 and S2 signal ($S0 \& S2$). Second, a possible electron event must also fire the Cherenkov. An analog sum of the signals from the 10 Cherenkov PMTs is formed. The logical AND of this Cherenkov sum and the logical AND of S0 and S2 signal forms the second trigger ($T2/T5 = (S0 \& S2) \& GC$). This helps separate the physics event from the cosmic events. In order to measure the trigger efficiency, a third trigger (T3/T6) which is the logical AND of the Cherenkov sum and the logical OR of the S0 and S2 signal ($(S0 || S2) \& GC$) is formed.

The trigger setup is shown in Fig.3.27 and Fig.3.28 [64]. For a given physics event in LHRS(RHRS), T1(T4) is designed to come first, T2(T5) second, and then T3(T6). The triggers are sent to the TS to make the gates for the ADCs and TDCs. The fired triggers are recorded in the data stream. A graphical user interface (GUI) is used to define the prescale factors of the triggers. In the MARATHON experiment, all the prescale factors were set to 1.

$$T1 = (S0 \& S2), T2 = (S0 \& S2) \& GC, T3 = (S0 | S2) \& GC$$

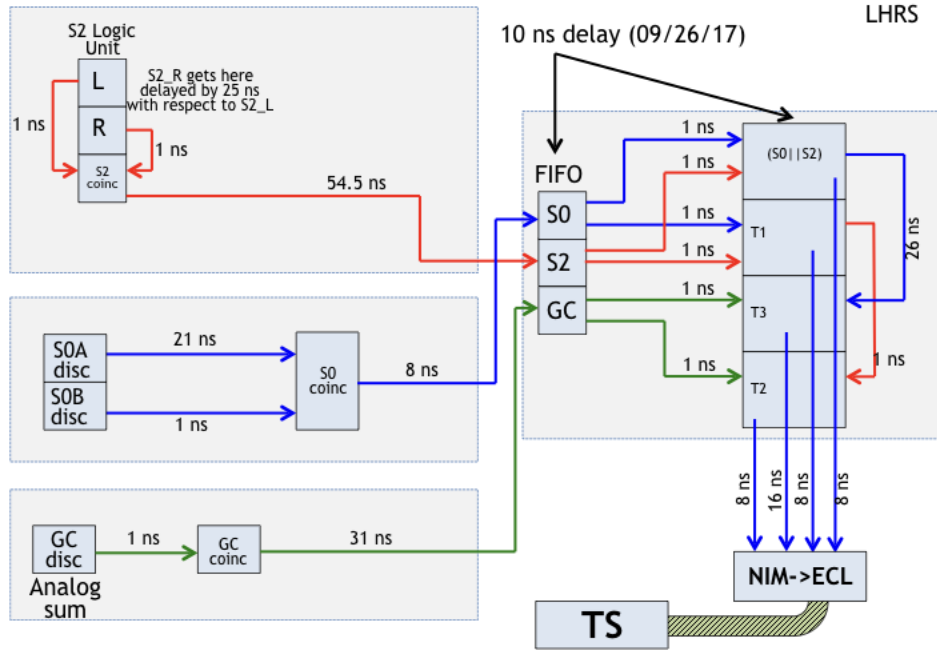


Figure 3.27: LHRS trigger setup

$$T4 = (S0 \& S2), T5 = (S0 \& S2) \& GC, T6 = (S0 | S2) \& GC$$

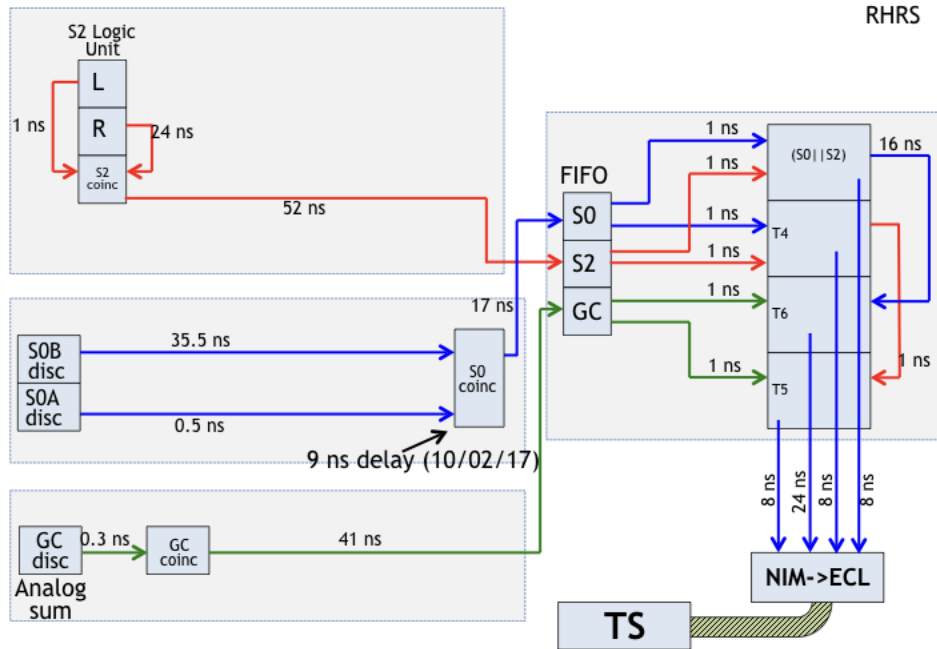


Figure 3.28: RHRS trigger setup

Chapter 4: Data Analysis

4.1 Introduction

The double differential electron scattering cross section $\frac{d\sigma}{dE'd\Omega}(E', \theta)$ represents the probability density function of finding an electron within energy range $\Delta E'$ and solid angle $\Delta\Omega$ after it scatters from a target particle. With a fixed incident energy, the cross section is a function of the scattering energy and the scattering angle. Using the equipment introduced in the last chapter, we are able to identify the scattered electrons and measure the physics kinematics in the scattering process, and eventually extract the cross section from the data collected.

The data yield is the integral of the double differential cross section over a certain phase space:

$$Y_{data} = \int \frac{d\sigma}{dE'd\Omega}(E', \theta) dE' d\Omega \quad (4.1)$$

It is related to the probability for an electron scattering into a certain solid angle. Therefore, the yield is extracted from the data as the ratio of the number of scattered electrons detected in that phase space (N_e) to the corresponding luminosity (L):

$$Y_{data} = \frac{N_e}{L} \quad (4.2)$$

Nominal cuts are applied to select the electrons scattered from the target gas. However, the detectors do not operate at 100% efficiency; the DAQ can miss an event due to electronics and computer processing time, and, in addition, some backgrounds are misidentified as electron events. In order to get the true number of scattered electrons, several corrections have to be applied:

$$N_e = (N_{raw}^e - N_{e^+} - N_{EC}) \cdot C_{eff} \cdot C_{DT} \cdot ACC(E', \theta) \quad (4.3)$$

where N_{raw}^e is the raw counts of the scattered electrons; N_{e^+} is the background electrons produced through pair production from the 2γ decayed of a π^0 ; N_{EC} is the background electrons scattered from the end caps of the target; C_{eff} is the product of detectors' efficiencies including trigger efficiency, VDC efficiency and PID efficiency; C_{DT} is the DAQ dead time correction; and $ACC(E', \theta)$ is the acceptance function which accounts for the non-uniform response of the spectrometer.

Luminosity is the product of the number of incident electrons (N_e^i) and the number of target particles (N_{targ}):

$$L = N_e^i \times N_{targ} \quad (4.4)$$

where N_e^i is calculated by multiplying the beam current by the beam time. N_{targ} is the number of target particles seen by the electrons, and is proportional to the density thickness regardless of the target length:

$$N_{targ} \propto \frac{\tau}{m_A} \quad (4.5)$$

where m_A is the nucleus mass, and τ is the gas thickness given in Table 3.2.

The average cross section can be extracted from the yield by:

$$\sigma_{avg}(\Delta E', \Delta\Omega) = \frac{Y_{data}(E', \theta)}{\Delta E' \Delta\Omega} \quad (4.6)$$

The yields from different targets are binned in the same way. Therefore, the cross section ratio is equal to the yield ratio. In the MARATHON experiment, a typical production run is about one hour, and after few runs the target was switched to a different gas target, while everything else was kept the same. The spectrometers are considered stable over time periods of hours. The efficiency of detectors and the acceptance function should be the same for different gases, and cancel out in the yield ratio. Only the dead time, the background contamination and the boiling effect have to be studied for each target. The consistency of efficiencies and the comparison between the acceptance functions of different targets are shown in Section 4.2. Finally, in order to get the Born cross section ratio at the bin center, the radiative correction, coulomb correction and the bin centering correction are applied.

4.2 DAQ and detector efficiencies

No detector and DAQ works perfectly. The inefficiency of detectors and DAQ affects the number of events collected, and results in misidentifying electrons. The DAQ dead time varies run by run, and has to be corrected in the data analysis. While the efficiencies of the detectors are canceled in the yield ratio, they characterize the behavior of the spectrometers and were monitored during the experiment.

4.2.1 DAQ dead time

The DAQ dead time is the time after each event during which the system can not record another event. It is a function of rate. The dead time consists of two parts. One part comes from the electronics dead time. Using a discriminator as an example, if the event rate is too high, a second pulse occurring during the process of the first pulse extends the dead time. The electronics dead time is usually less than 100 ns [52]. Since the event rate during the MARATHON experiment was lower than 2 kHz, electronics dead time is negligible. The second part is the TS processing dead time, and the dead time when the computer and network transfer data. This is measured and corrected per run.

For the dead time measurement, scalers with zero dead time are used to monitor the absolute counts. The triggers are sent to both the TS and the scalers. Since the prescale factor was kept at 1, the ratio of the CODA recorded trigger counts (N_{trig}) and the counts from scaler (N_{scal}) represents the DAQ live time. The dead time correction factor is:

$$C_{DT} = \frac{1}{N_{trig}/N_{scal}} \quad (4.7)$$

In data analysis, the T2 trigger is used in the LHRS electron selection. For RHRS which only ran at the kin16, the T5 trigger is used. The dead time correction factor of T2(T5) trigger for different kinematics is shown in Fig.4.1.

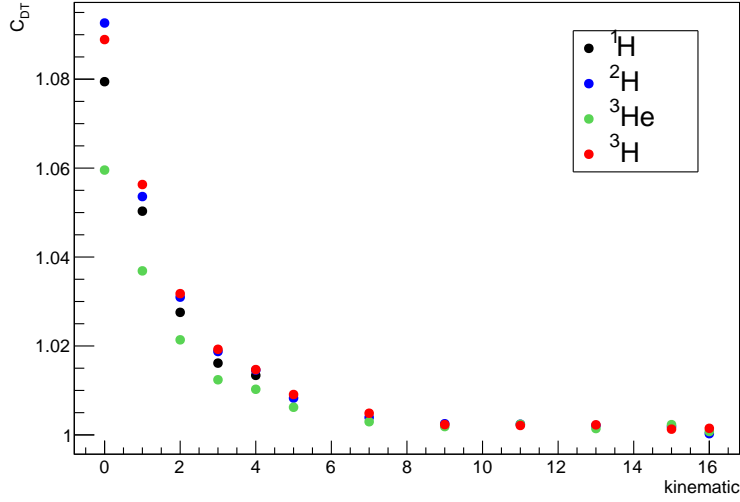


Figure 4.1: T2(T5) dead time correction factor of each target for each kinematic setting

4.2.2 Trigger efficiency

Inefficiencies in the scintillators and Cherenkov result in a failure for generating triggers for an electron event. As the leading trigger, the T1/T4 (S0&S2) efficiency can be measured using T3/T6 ((S0||S2)&GC) as a reference. In principal, if T3/T6 is formed for an electron event, T2/T5 ((S0&S2)&GC) must be formed too. For a good electron sample with T3/T6 fired, if the T2/T5 counts are less than the T3/T6 counts, the difference comes from the (S0&S2) inefficiency, which is equivalent to the T1/T4 inefficiency. Since the VDC timing is invalid for an event with missing T1/T4, using the spectrometer reconstructed information to select the electron sample can cause a bias. Only the Cherenkov sum cut and the energy cut of the shower detectors are applied in the electron sample selection. The T1/T4 efficiency, $\eta_{T1/T4}$ is then equal to the ratio of T2/T5 counts to the T3/T6 counts in the electron sample:

$$\eta_{T1/T4} = \frac{\text{T2/T5 counts in the electron sample}}{\text{T3/T6 counts in the electron sample}} \quad (4.8)$$

In order to minimize the dilution from cosmic events, the T1/T4 trigger efficiency is calculated at high event rate runs for each gas target. The efficiency results are shown in Fig.4.2a, and the ratios

of T1 efficiency between different targets are shown in Fig.4.2b. The ratios are equal to one within statistical uncertainties.

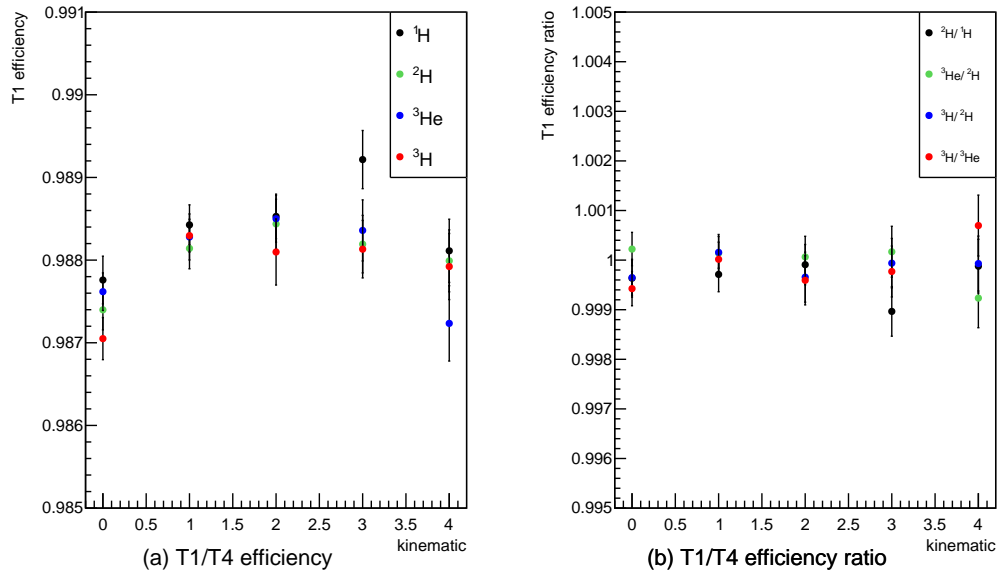


Figure 4.2: T1/T4 trigger efficiency

While T1/T4 is the production trigger, T2/T5 is the trigger used in data analysis. Besides S0&S2 efficiency, T2/T5 involves the Cherenkov detection efficiency – that is, the possibility of Cherenkov to be fired when an electron passes. If we can select a clean electron sample, the ratio of the T2/T5 counts to T1/T4 counts in the sample represents the Cherenkov detection efficiency. This efficiency multiplied by the T1/T4 efficiency is the T2/T5 efficiency. However, it is difficult to define a clean electron sample with only an E/P cut, since there is pion contamination in the shower detectors (introduced in Section 4.4.1). While other tritium experiments which were run before and after the MARATHON experiment have much lower π/e , their study shows that the Cherenkov detection efficiency is close to 1.

4.2.3 VDC efficiency

Two parts contribute to the VDC efficiency. The first part is the VDC detection efficiency; that is, the efficiency of the wire being fired when a charged particle passes. It is measured by using

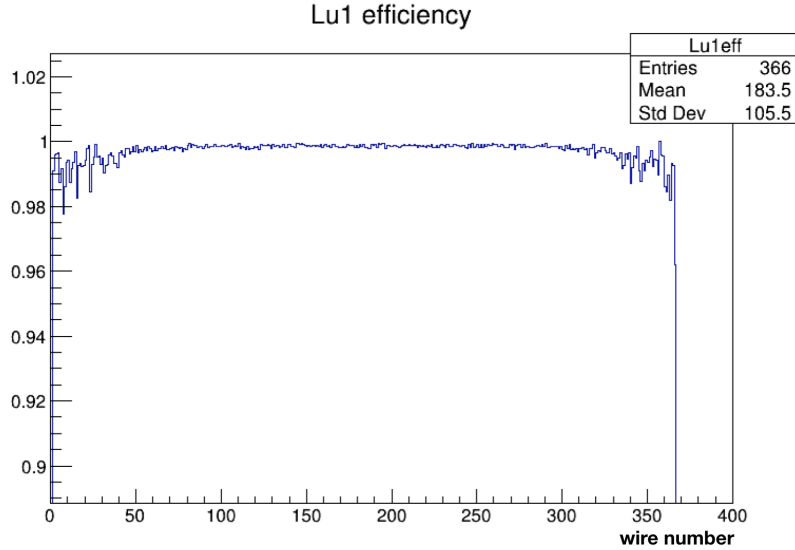


Figure 4.3: Detection efficiency of LHRs U1 wires

three adjacent wires. If the two outer wires have a hit, the middle wire should be fired as well. The efficiency of each wire was monitored online during data taking. An example of the online efficiency plot is shown in Fig.4.3. The VDC detection efficiency is above 99% for the central area where most data are collected.

The dominant inefficiency from the VDC comes from the track reconstruction. In the data analysis, a good electron event is required to have only one track. Due to backgrounds and software misreconstruction, there exist electron events with no track or multiple tracks. This efficiency is obtained by calculating the percentage of one-track events in a clean electron sample. The T2 trigger and tighter PID cuts are applied in the clean sample selection. In order to minimize the cosmic contamination in the electron sample, the VDC efficiency is studied for the low x kinematic settings, where the event rate is much higher than the cosmic rate. The one-track efficiency is shown in Fig.4.4. The efficiency is about 98% and is the same between different targets.

4.2.4 PID efficiency

The Cherenkov and shower detectors are used to identify the electrons. However, the Cherenkov can be fired by the knock-on electrons produced by other particles with fewer photoelectrons emitted. As can be seen in Fig.4.5(a), the peak around 300 is the single photoelectron peak. In the

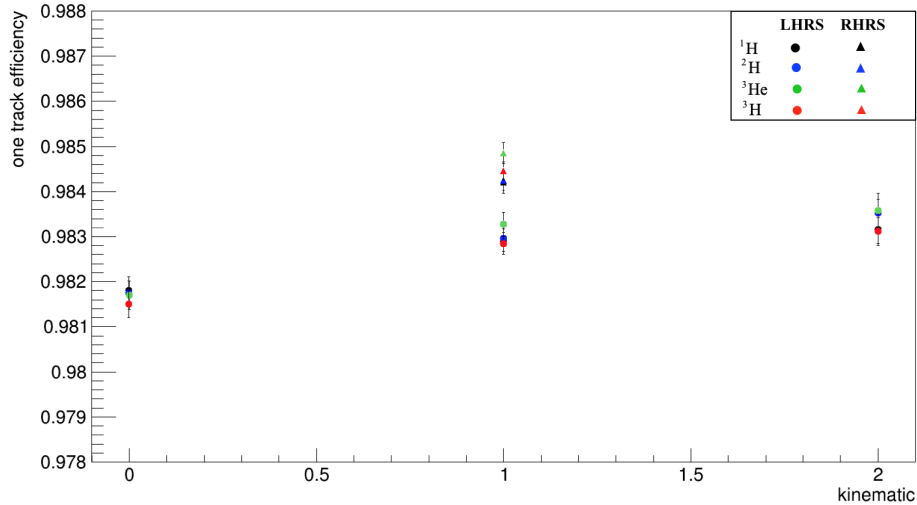


Figure 4.4: VDC efficiency for LHRS and RHRS at kin0, kin1 and kin2

shower detectors, other particles (mostly pions) deposit some part of their energy, which generate a small peak at low E/P in Fig.4.5(b). Therefore, a specific Cherenkov sum cut and a E/P cut are applied to get rid of these backgrounds, which are called PID cuts. In the PID cuts study, we care about both the possibility of electrons being able to survive the cuts (η_e), and the possibility to reject pions (η_π).

The PID efficiency is the product of the Cherenkov sum cut efficiency and the E/P cut efficiency. If a clean electron sample or pion sample is selected, the efficiency is measured by passing the sample events through the cut. Cherenkov and shower detectors are considered to work independently. Therefore, the electron/pion sample used in the Cherenkov sum cut study is selected by a tight E/P cut as well as other nominal cuts. Similarly, the sample for the E/P cut study is obtained by applying a tight Cherenkov sum cut. Low π/e runs are used. The PID study shows that the η_e is above 99%, and η_π is above 99.9%.

4.2.5 Acceptance

When the spectrometer transports the charged particles from target to focal plane, the electrons can be stopped when they collide with the edge of the magnet systems. The acceptance of the spectrometer depends on the interaction vertex position, the in-plane and out-of-plane angle, and

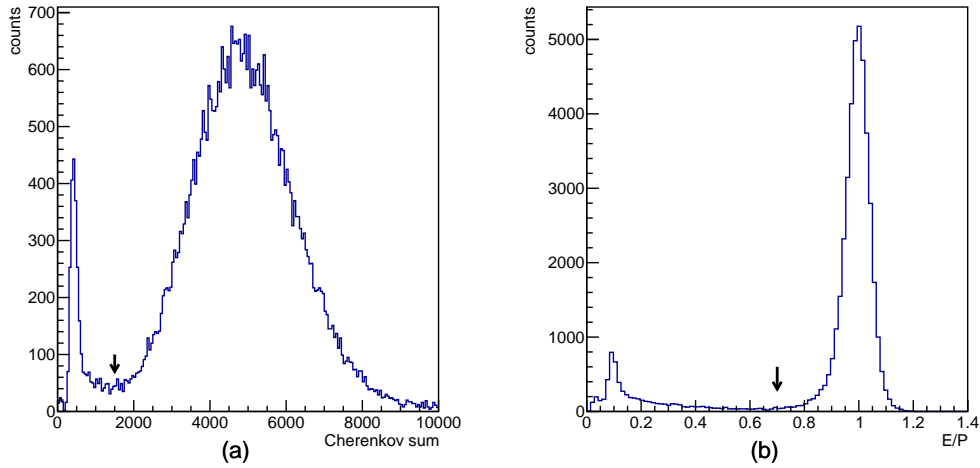


Figure 4.5: Cherenkov sum distribution and E/P distribution. The arrows point to the nominal cuts.

the momentum. While the cross sections depends only on the momentum (E') and the full scattering angle (θ), it is convenient to measure the acceptance as a function of E' and θ . The acceptance function $A(E', \theta)$ is not uniform everywhere. It is close to 1 at the center of the spectrometer and starts to drop off when reaching the edge. Acceptance cuts on the interaction vertex position, the in-plane and out-of-plane angle, and the relative momentum are applied to avoid multi-scattering effects and bad optics reconstruction near the edge.

Normally, the acceptance function is determined from simulations when extracting the absolute cross section. However, since the geometrical acceptance does not depend on the target nuclei, it is supposed to be canceled in the yield ratio between different targets. In the MARATHON data analysis, a quick comparison between the acceptance functions of ^2H and ^1H was performed. The E' vs. θ distribution in data with all the nominal cuts applied represents a convolution of the radiative cross section and the acceptance function. The radiative cross section is obtained from the program mentioned in Section 4.5. Assuming that the acceptance function is uniform in a small phase space, the (E', θ) distribution divided by the radiative cross section gives the acceptance value for each (E', θ) bin. The ratio of the ^2H acceptance to the ^1H acceptance is shown in Fig.4.6. The ratio is near 1 except for a few bins at the edge with poor statistics.

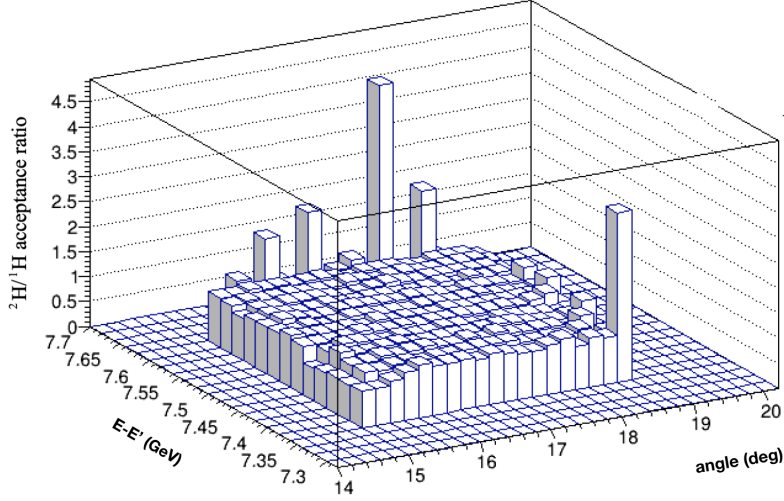


Figure 4.6: The $^2\text{H}/^1\text{H}$ acceptance function ratio

4.3 Boiling effect correction

As can be seen in Eq.(4.4), the luminosity depends on the gas target thickness. However, when the electron passes through the target gas, the heat generated by the radiation changes the local density. The target thickness τ given in Table 3.2 needs to be corrected. The amount of heat deposited is determined by the beam current. Therefore, the real gas thickness “seen” by the electrons is a function of current; this is called the boiling effect.

The boiling effect for each gas target was studied by performing a current scan. Both the data and simulation show that the target density reaches equilibrium within a few seconds after the beam first hits the target. Two analysis methods are applied to measure the boiling effect. The first method is to extract the charge normalized yield of the gas with corrections applied [65]. The corrections include detector efficiencies, DAQ dead time and end cap contamination. The charge normalized yield is given by:

$$Y_{gas} = \frac{PS \cdot N_e}{Q \cdot \epsilon \cdot LT} \quad (4.9)$$

where PS is the DAQ prescale factor, N_e is the number of good electrons with background subtracted, Q is the total charge incident on the target, ϵ is the product of detector efficiencies and PID efficiency, and LT is the live-time. The Y_{gas} is measured at multiple incident currents (I_{beam}). A

simple quadratic polynomial function describes well the boiling effect's relation between Y_{gas} and I_{beam} . This function is then normalized to 1 at $I_{beam} = 0$, where there is no boiling effect. The boiling correction is applied run by run by multiplying the gas thickness by the correction factor expressed as:

$$f(I_{beam}) = a \cdot I_{beam}^2 + b \cdot I_{beam} + 1.0 \quad (4.10)$$

where a, b are the fit parameters, and I_{beam} is the average current of the run. The density change for ^3H target as a function of current is shown in Fig.4.7. At low current, the systematic uncertainty is larger, because the BCM monitors have larger uncertainty for low current measurement.

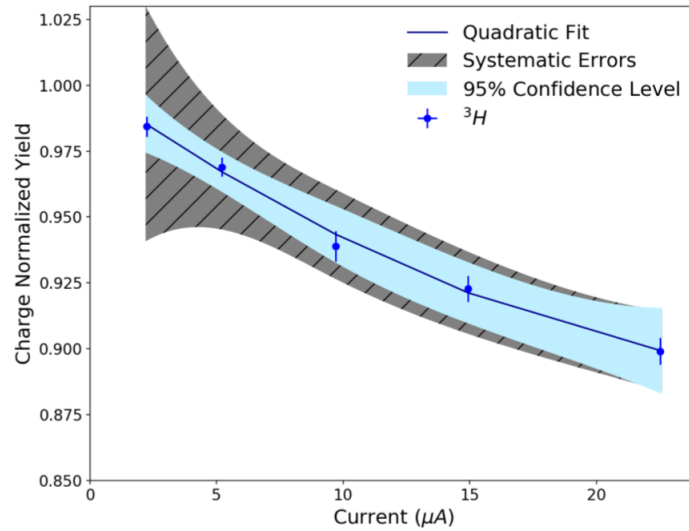


Figure 4.7: The ^3H density change as a function of current

The second method avoids performing the corrections by taking the ratio:

$$R_{boiling} = \frac{Y_{gas}}{Y_{end\ cap}} \quad (4.11)$$

where Y_{gas} and $Y_{end\ cap}$ are the charge normalized yields from the gas section of the target compared to the upstream end cap. The solid target does not have a boiling effect, which has been proved by measuring the yield from an aluminum target at different currents [65]. Therefore, $Y_{end\ cap}$ remains constant at different currents. The distribution of $R_{boiling}$ is proportional to that of Y_{gas} . And this normalization difference will be eliminated when normalizing the $R_{boiling}$ to 1 at $I_{beam} = 0$.

Since Y_{gas} and $Y_{end\ cap}$ are extracted with the same nominal cuts except for the vertex Z cut in the same run, the corrections applied in the first method as well as the total charge are canceled in the ratio. This avoids the uncertainty induced by the BCM offset uncertainty in the beam charge measurement. Then the yield ratio in Eq.(4.11) is reduced to the ratio of electron counts from gas versus those from upstream end cap part:

$$R_{boiling} = \frac{Y_{gas}}{Y_{end\ cap}} = \frac{N_e^{gas}}{N_e^{end\ cap}} \quad (4.12)$$

Boiling data were collected with the LHRS during December 2017, March 2018 and May 2018 with different kinematic settings. They were analyzed by the above two methods, and the results are in agreement. The ratio of the density correction factors between targets are shown in Fig.4.8. Most of our production data were taken with the current set at $20\ \mu A$.

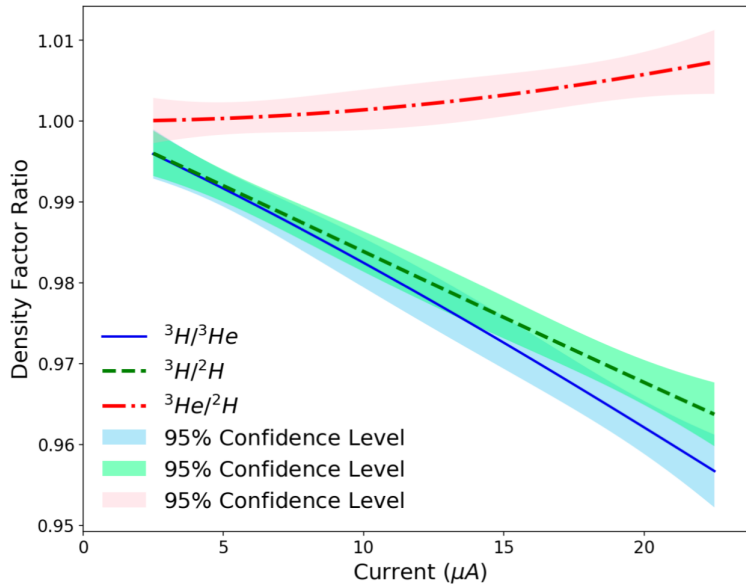


Figure 4.8: The boiling correction factor ratio for various target combinations

4.4 Background subtraction

As shown in previous sections, the efficiencies of the detectors are close to 100%. The two HRS are able to characterize 99% of electrons and reject 99.99% of non-electron particles. However,

not all the detected electrons are scattered from the target gas. The electrons generated from other processes can contribute. This electron backgrounds vary according to the target geometry and the kinematics. They are different for different targets, and have to be considered in the extraction of cross section ratios.

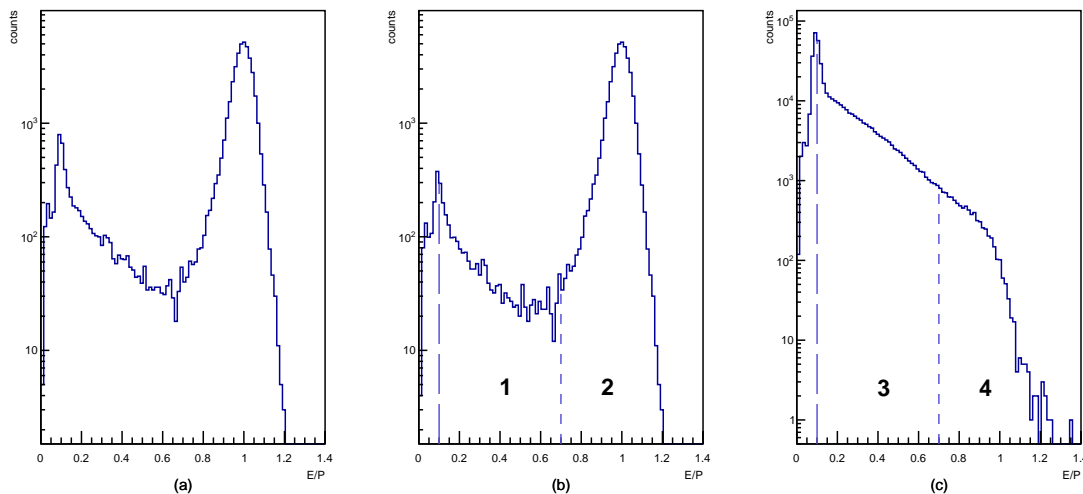


Figure 4.9: The E/P distribution for: (a) all events with nominal cuts applied except PID cuts; (b) pions (no Cherenkov signals); (c) electrons (with Cherenkov cut). The long-dashed lines indicate the cut of $E/P > 0.1$. The short-dashed lines are the nominal E/P cut.

4.4.1 Pion contamination

Even though the Cherenkov rejects pions with 99% efficiency, a pion can fire the Cherenkov by producing knock-out electrons. In the shower detectors, pions normally deposit a small amount of energy which generate a second peak at low E/P . However, the tail of the peak can be above the nominal E/P cut as shown in Fig.4.9(c). That is, some pions pass the PID cuts and are misidentified as electrons.

Since the pion E/P spectrum is independent of the Cherenkov signals, the pion contamination in Fig.4.9(b) is obtained by properly normalizing the pion distribution from Fig.4.9(c). In order to determine the normalization, two regions are defined in the E/P distributions of pions and electrons as shown in Fig.4.9. The regions 1 and 3 are supposed to be pure pion regions, which are

defined by the cut $0.7 > E/P > 0.1$. This cut helps remove events with E/P near 0 which might come from inefficiency in the shower detectors. The regions 2 and 4 are defined by the nominal E/P cut. The normalization is obtained from $N1/N3$. The π/e ratio is given by $(N1/N3)*N4/N2$. This actually overestimates the π/e ratio, since region 1 includes not only pions but also some electrons which come from the tail of the main E/P peak. The π/e ratio is shown in Fig.4.10. It is less than 0.26%. Since the pion contamination is so small, and it cancels out when subtracting other backgrounds, no correction is applied for the pion contamination.

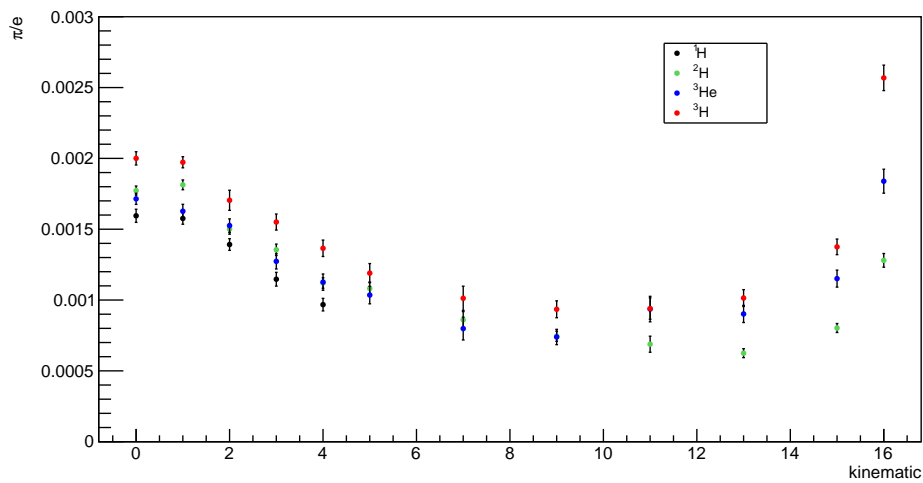


Figure 4.10: The π/e ratio

4.4.2 End cap contamination

The aluminum entrance window of the gas target is about 0.25 mm thick. From a scattering cross section perspective, its thickness is comparable to the gas thickness. As a result, a large part of the scattered electrons come from the end cap. A vertex Z position cut is applied to get rid of these end cap events. However, the tail of the end cap events leak into the region where the gas is present, and is not removable by the nominal cuts, as shown in Fig.4.11. The upstream end cap is flat, while the downstream end cap is round. This difference leads to the different width and height of the two end cap peaks in Fig.4.11.

The end cap contamination is studied by performing an identical kinematic scattering on the

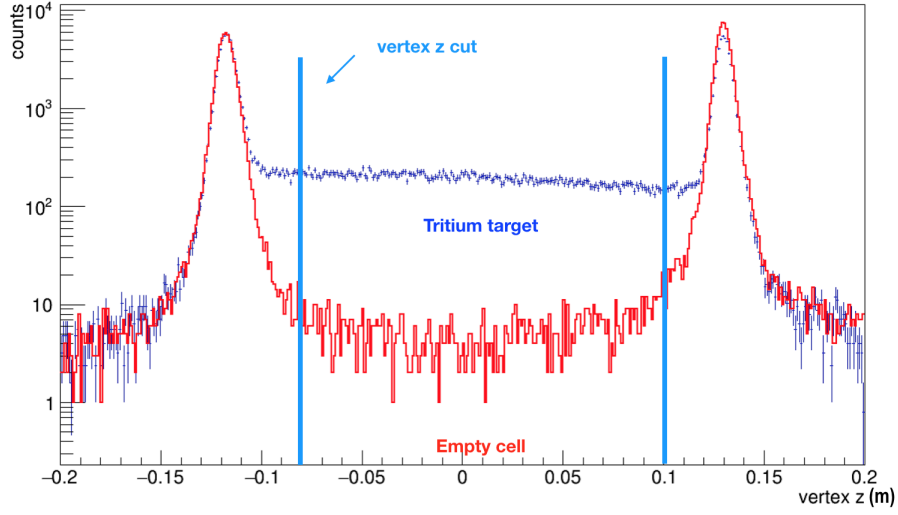


Figure 4.11: The vertex z distribution at target

empty cell. The empty cell has the same design as the gas target, but with no gas filled. The contamination is measured by extracting the luminosity normalized yield of the empty cell with the nominal cuts applied. The luminosity is the product of the total beam charge and the thickness of the empty cell window, where the upper part (vertex $Z < 0$) of the target uses the entrance window thickness, and the lower part (vertex $Z > 0$) uses the exit window thickness. Since the gas targets have slightly different window thickness from the empty cell, a thickness correction factor is applied to the empty cell yield (Y_{EM}) to find the true end cap contamination for each gas,

$$Y_{EM}^{Corr} = Y_{EM} \times \frac{T_{window}^{gas}}{T_{window}^{EM}} \quad (4.13)$$

where T_{window}^{gas} is the window thickness of the gas target, and T_{window}^{EM} is that of the empty cell [66]. The ratio of Y_{EM}^{Corr} to the gas yield gives the percentage for the end cap contamination. It is a function of x . One or two empty cell runs were taken regularly after few production runs. The detector efficiencies and spectrometer acceptance remain the same for all targets. Therefore, only the dead time correction and boiling effect are considered in the ratio. The end cap contamination correction factor is:

$$C_{EC} = 1 - \frac{Y_{EM}^{Corr}}{Y_{gas}} \quad (4.14)$$

The ratios of the correction factors between different gases are fitted by exponential functions. The raw cross section ratio is then corrected by multiplying C_{EC} bin by bin. The correction factors on ratios are shown in Fig.4.12, where only statistic uncertainties are considered.

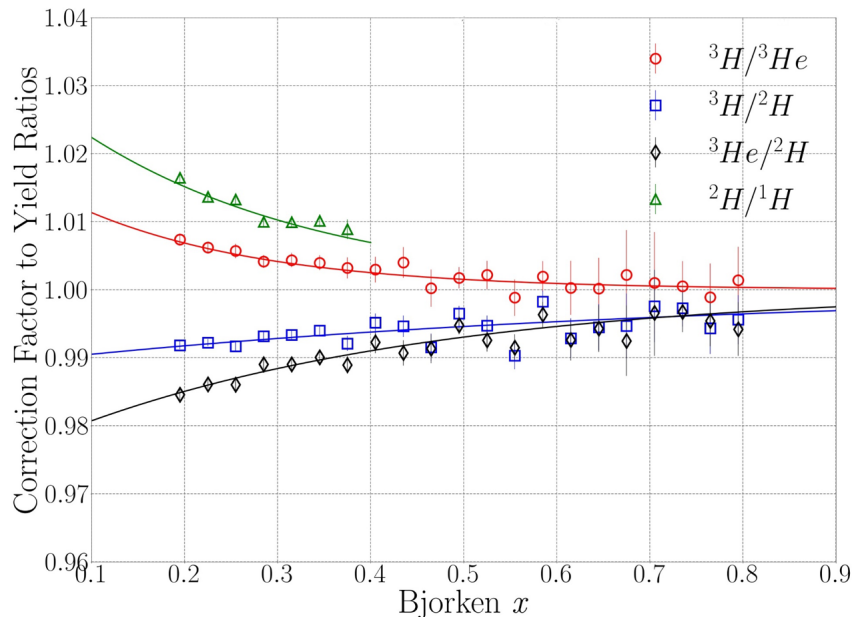


Figure 4.12: End cap contamination correction factor on ratios

4.4.3 Charge symmetric background

When the electron passes through the target, there is a possibility of the scattering process producing a π^0 . The π^0 decays into two photons, which then produce electron-positron pairs. These electrons behave the same as those scattered from the gas, so they cannot be removed by the nominal cuts. As the electrons and positrons are produced in pairs, the electron background is measured by extracting the luminosity normalized yield of the positrons. The π^0 decay is the dominant process for producing positrons.

The positron yield was measured by reversing the polarity of the spectrometer. Since the cross section is very small and decreases when x increases, the positron runs were taken only at low kinematic settings (kin1, kin3, kin5). The ratio of e^+/e^- is equal to their yield ratio. An empty cell measurement was performed for each positron kinematic setting to subtract the end cap back-

ground using the same procedure discussed in Section 4.4.2. The relative hadron (especially π^+) rate was higher in positron runs than that in the electron runs, which produces a non-negligible pion background. The pion contamination is determined by fitting the E/P distribution with a combination of an exponential function and a Gaussian function, see Fig.4.13. The ratio of the integral of the exponential tail above the nominal E/P cut to the total positron events represents the pion contamination. After subtracting the end cap contamination and pion contamination, the

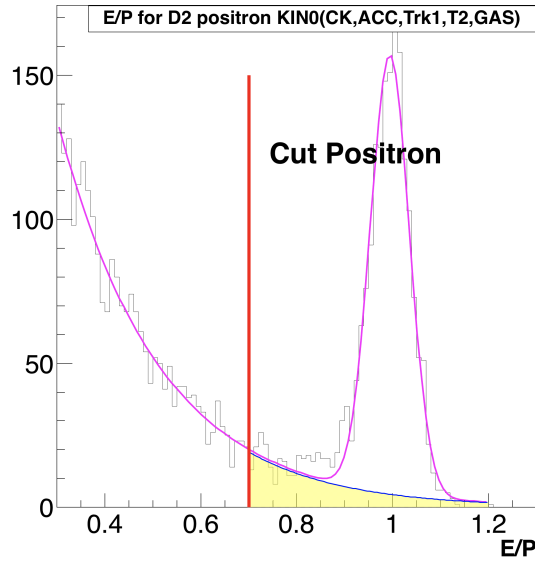


Figure 4.13: E/P distribution of positrons with nominal cuts applied

ratio of positron yield to electron yield, $R(x) = Y_{e^+}/Y_{e^-}$, is fit by an exponential function. As shown in Fig.4.14, the charge symmetric background is less than 1.6% at low x and is negligible at high x . It is removed by multiplying the raw cross section ratio by the correction factor given in Eq.(4.15):

$$C_{e^+} = 1 - \frac{Y_{e^+}}{Y_{e^-}} = 1 - R(x) \quad (4.15)$$

4.4.4 Tritium decay

Tritium is radioactive, decaying into helium-3 by the following beta decay process:



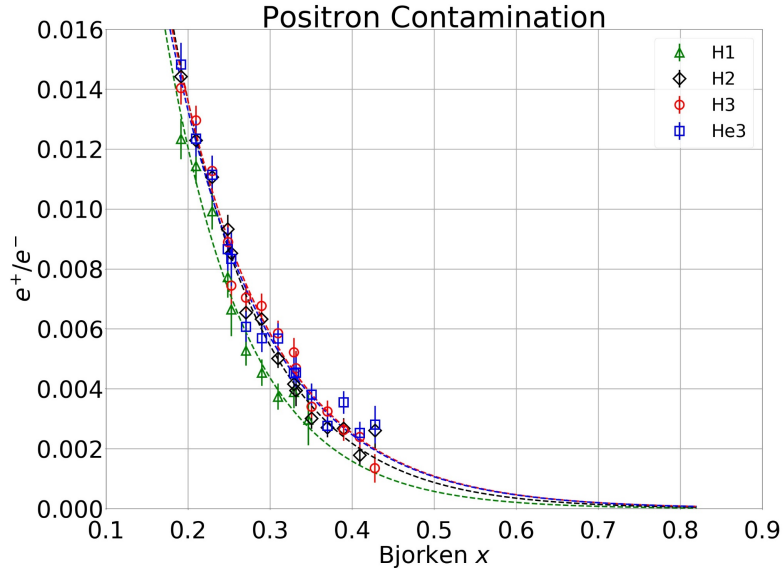


Figure 4.14: Charge symmetric background correction factor

with a half life of $\tau_{1/2} = 4500 \pm 8$ days [67]. This results in a decreasing ${}^3\text{H}$ density and increasing ${}^3\text{He}$ contamination in the tritium target. Therefore, the yield extracted from tritium data ($Y_{raw}^{3\text{H}}$) represents a combination of electrons scattering on ${}^3\text{H}$ and ${}^3\text{He}$:

$$Y_{raw}^{3\text{H}} = \frac{\sum_i (T_i + H_i)}{\sum_i Q_i (N_i^t + N_i^h)} \quad (4.17)$$

where i is the run number, T_i (H_i) is the number of electrons scattered from ${}^3\text{H}$ (${}^3\text{He}$), Q_i is the beam charge, and N_i^t (N_i^h) is ${}^3\text{H}$ (${}^3\text{He}$) thickness in the tritium target. A correction factor is applied to remove the ${}^3\text{He}$ yield and extract the real ${}^3\text{H}$ yield.

The tritium target was filled with an initial tritium number N_0^t , and an initial helium-3 number N_0^h [57]. As tritium decays into helium-3, the ${}^3\text{H}$ number and ${}^3\text{He}$ number change over time:

$$N_i^t = N_0^t e^{-t_i/\tau_{1/2}} \quad (4.18)$$

$$N_i^h = N_0^h + N_0^t (1 - e^{-t_i/\tau_{1/2}}) \quad (4.19)$$

But the total number of nuclei in the target cell remains constant: $N_{tot} = N_0^t + N_0^h$. Therefore,

Eq.(4.17) is rewritten to separate out the ^3H yield:

$$Y_{raw}^{3\text{H}} = \frac{\sum_i T_i}{\sum_i Q_i N_i^t} \cdot \frac{\sum_i Q_i N_i^t}{\sum_i Q_i N_{tot}} + \frac{\sum_i H_i}{\sum_i Q_i N_i^h} \cdot \frac{\sum_i Q_i N_i^h}{\sum_i Q_i N_{tot}} \quad (4.20)$$

$$= Y_{3\text{H}} \cdot \frac{\sum_i Q_i (1 - f_{\text{He}_i})}{\sum_i Q_i} + Y_{3\text{He}} \cdot \frac{\sum_i f_{\text{He}_i}}{\sum_i Q_i} \quad (4.21)$$

where $Y_{3\text{H}}$ ($Y_{3\text{He}}$) is the real ^3H (^3He) yield, f_{He_i} is the ^3He contamination in the tritium target for each run (see Fig.4.15):

$$f_{\text{He}_i} = \frac{N_i^h}{N_{tot}} \quad (4.22)$$

Once the ^3He yield is found, the ^3H yield can be separated from the raw yield via the expression:

$$Y_{3\text{H}} = Y_{raw}^{3\text{H}} \cdot \frac{\sum_i Q_i}{\sum_i Q_i (1 - f_{\text{He}_i})} - Y_{3\text{He}} \cdot \frac{\sum_i Q_i f_{\text{He}_i}}{\sum_i Q_i (1 - f_{\text{He}_i})} \quad (4.23)$$

The real ratio of ^3H and ^3He yields becomes:

$$\frac{Y_{3\text{H}}}{Y_{3\text{He}}} = \frac{Y_{raw}^{3\text{H}}}{Y_{3\text{He}}} \cdot \frac{\sum_i Q_i}{\sum_i Q_i (1 - f_{\text{He}_i})} - \frac{\sum_i Q_i f_{\text{He}_i}}{\sum_i Q_i (1 - f_{\text{He}_i})} \quad (4.24)$$

The ratio of ^3H to ^2H yields is obtained in a similar way:

$$\frac{Y_{3\text{H}}}{Y_{2\text{H}}} = \frac{Y_{raw}^{3\text{H}}}{Y_{2\text{H}}} \cdot \frac{\sum_i Q_i}{\sum_i Q_i (1 - f_{\text{He}_i})} - \frac{Y_{3\text{He}}}{Y_{2\text{H}}} \cdot \frac{\sum_i Q_i f_{\text{He}_i}}{\sum_i Q_i (1 - f_{\text{He}_i})} \quad (4.25)$$

4.5 Radiative corrections

The cross section given by Eq.(2.20) corresponds to the zeroth order Feynman diagram, which is called the Born cross section. However, to describe the true scattering process, higher order corrections must be applied due to a number of effects. Firstly, the electrons lose energy when traveling through materials via bremsstrahlung and ionization. The measured incident energy and scattering momentum do not represent the true ones during the collision. Secondly, higher or-

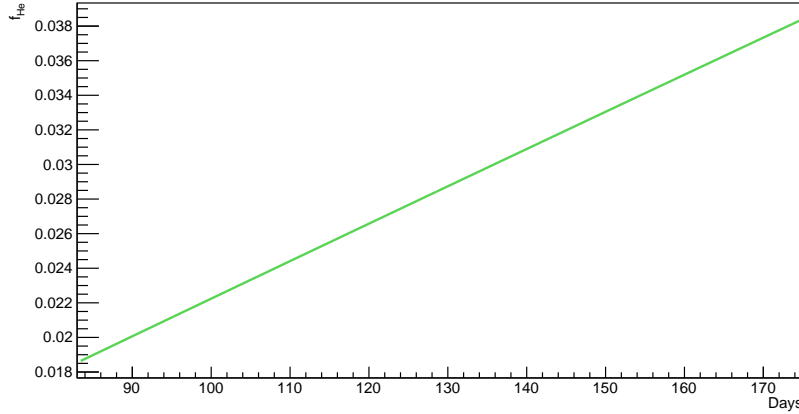


Figure 4.15: ^3He contamination in ^3H target during the MARATHON experiment

der quantum electrodynamics (QED) processes also make contributions to the total cross section. These radiative effects need to be removed from the raw yield to obtain the Born cross section. The program used to compute the radiative corrections for the MARATHON experiment is the same one used in the Hall C 6 GeV EMC experiment (JLab E03-103) [68] with the tritium target geometry incorporated. It is primarily based on the Mo & Tsai method [69, 70].

The “internal” radiative effects, which occur during the collision, include the vacuum polarization and the electron vertex diagrams, the internal bremsstrahlung, and the soft multiple photon emission process (see Fig.4.16). The corrections are restricted to one photon exchange between the electron current and hadron current. Photon emission by hadrons is negligible. The infrared divergent piece of the two-photon exchange diagrams and the emission of real photons by hadrons are only considered in radiative corrections to the elastic peak. The straggling effect of the electrons passing through the materials before and after the collision is referred to as “external” radiative effect, which is a combination of external bremsstrahlung and ionization. The measured cross section (σ_{rad}) is related to the Born cross section by [70]:

$$\sigma_{rad}(E_s, E_p) = \int_0^T \frac{dt}{T} \int_{E_s \min(E_p)}^{E_s} dE'_s \int_{E_p}^{E_p \max(E'_s)} dE'_p I(E_s, E'_s, t) \sigma_r(E'_s, E'_p) I(E'_p, E_p, T - t) \quad (4.26)$$

where $I(E, E', t)$ represents the probability of an electron with initial energy E losing energy to

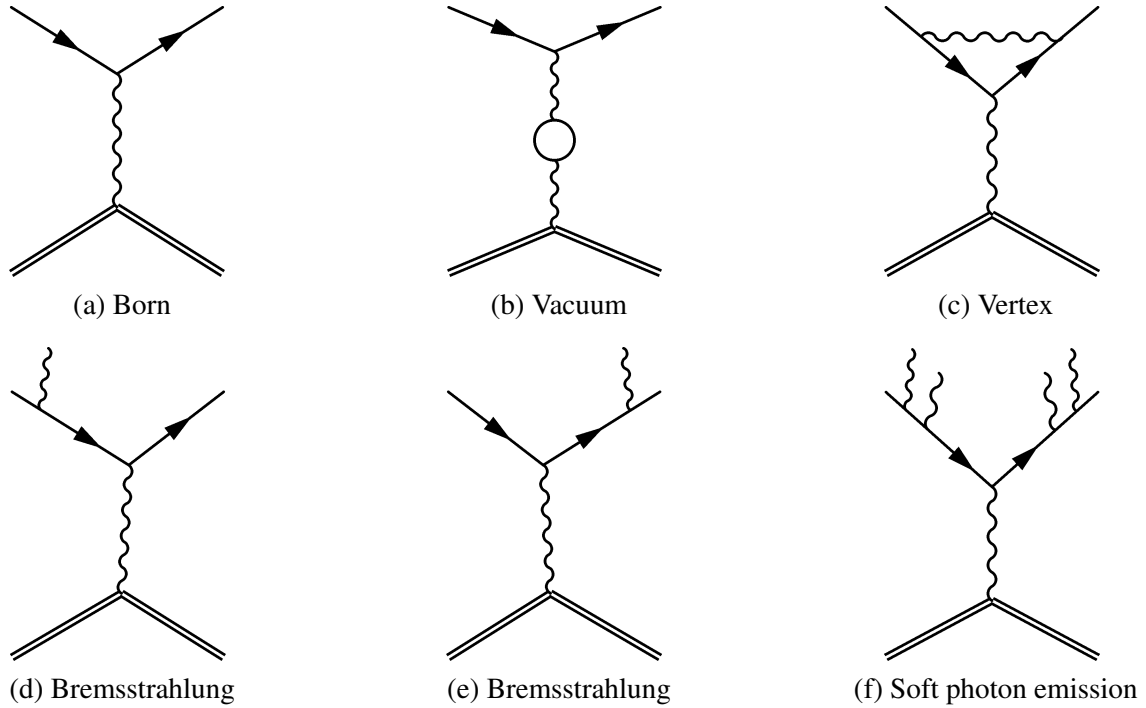


Figure 4.16: Feynman diagrams in internal radiative correction

E' after traveling distance t in the material due to the external radiation. T is the total path length of the electron before scattering and after scattering. E_s is the measured incident energy and E_p is the measured scattering energy. $\sigma_r(E'_s, E'_p)$ is the Born cross section $\sigma_{born}(E'_s, E'_p)$ with internal radiative effects included.

The missing mass squared (W^2) of the scattering is defined by the four momentum of the final hadron system (p_f) and of the emitted photon(k):

$$W^2 = (p_f + k)^2 \geq p_f^2 = M_f^2 \quad (4.27)$$

where M_f is the invariant mass of the final hadron system. For a given missing mass, the invariant mass of the final hadron system will be small if high energy photons are emitted. That is to say, the lighter invariant mass states have a radiative tail at the heavier invariant mass states, but not vice versa. For example, the elastic peak has the smallest M_f , hence its tail affects all the other states. As a result, the radiative cross section for DIS is a combination of radiative tails from the elastic

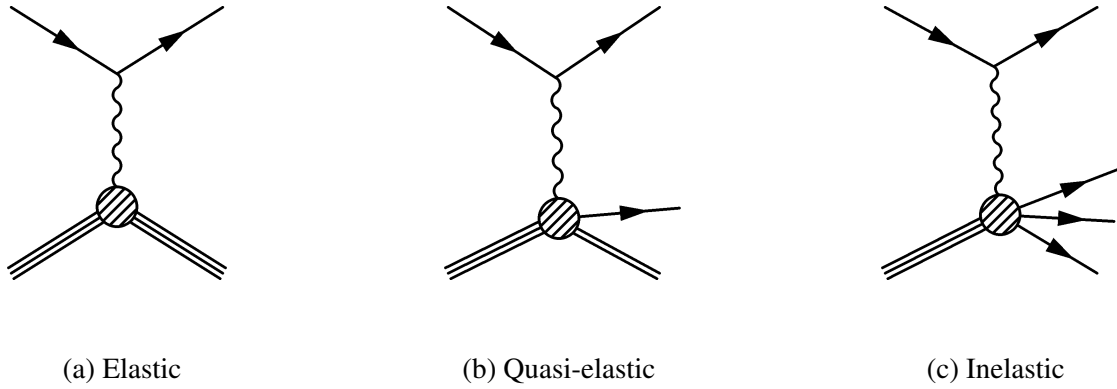


Figure 4.17: Schematic representation of the processes that contribute to the DIS radiative cross section

peak, quasi-elastic states, and the nearby DIS states (see Fig.4.17):

$$\sigma_{rad} = \sigma_{rad}^{elastic} + \sigma_{rad}^{quasi-elastic} + \sigma_{rad}^{DIS} \quad (4.28)$$

Each process can be calculated using Eq.(4.26). The elastic tail and quasi-elastic tail are calculated by the exact formula given by Mo & Tsai. For DIS, the internal bremsstrahlung is approximated by adding two external radiators, one before and one after the scattering. The rest of the internal radiative effects are included in a factor $F(Q^2, T)$ similar to Eq.(2.8) in [70]. The σ_r is the product of σ_{born} and $F(Q^2, T)$. The double integral in Eq.(4.26) is calculated exactly instead of using the energy peaking approximation. The ionization is taken care of event by event in the data analysis rather than in the radiative corrections [71].

If there is a valid model Born cross section (σ_{born}^{model}) that applies over the measured region, the radiative cross section (σ_{rad}^{model}) can be calculated from it. Then the radiative correction factor becomes the ratio:

$$RC = \frac{\sigma_{born}^{model}(E', \theta)}{\sigma_{rad}^{model}(E', \theta)} \quad (4.29)$$

The Born cross section extracted from data (σ_{born}^{data}) is obtained by multiplying the measured cross

section (σ_{rad}^{data}) by the radiative correction factor:

$$\sigma_{born}^{data} = \sigma_{rad}^{data} \cdot RC \quad (4.30)$$

The radiative correction factors applied to the cross section ratios as a function of x are shown in Fig.4.18.

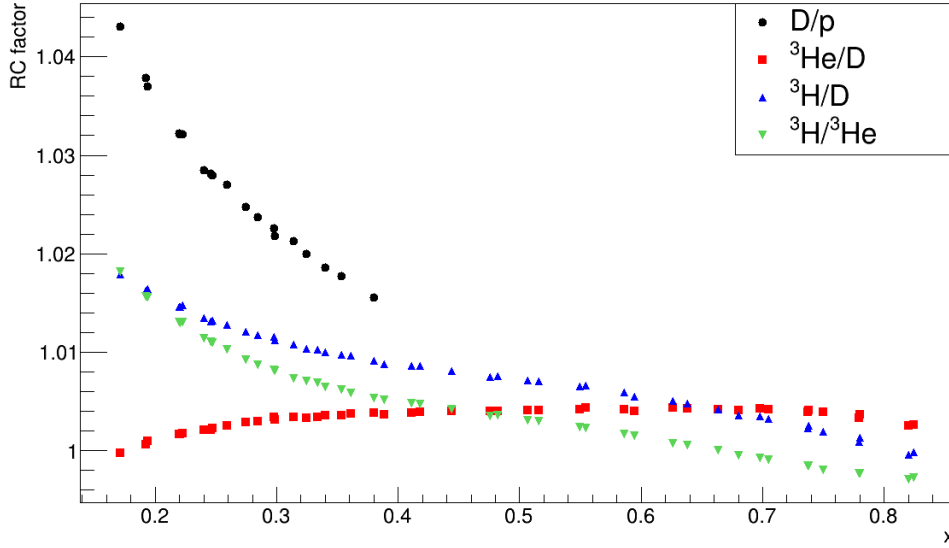


Figure 4.18: Radiative correction factors applied to the cross section ratios as a function of x

4.5.1 Cross section model

In order to make a good estimate of the radiative correction factor, it is important to choose a cross section model that approximates accurately the real Born cross section. For the MARATHON kinematics, the contribution to the radiative cross section from the elastic tail and quasi-elastic tail is small (see Fig.4.19). The elastic cross section is calculated from the nuclei form factors. The quasi-elastic cross section is obtained by using a y -scaling model [68]. For the inelastic cross section, the model used in 6 GeV experiments is no longer valid, due to the larger Q^2 from the higher energy beam in the MARATHON experiment. However, the structure functions for the proton (F_2^p) and deuteron (F_2^d) are well measured by many experiments over a wide kinematic range. And there are numerous phenomenological EMC models which describe the previous EMC

data over the x range similar to the MARATHON experiment. Therefore, the structure function for ${}^3\text{H}$ and ${}^3\text{He}$ can be computed by multiplying the deuteron structure function by the EMC ratio.

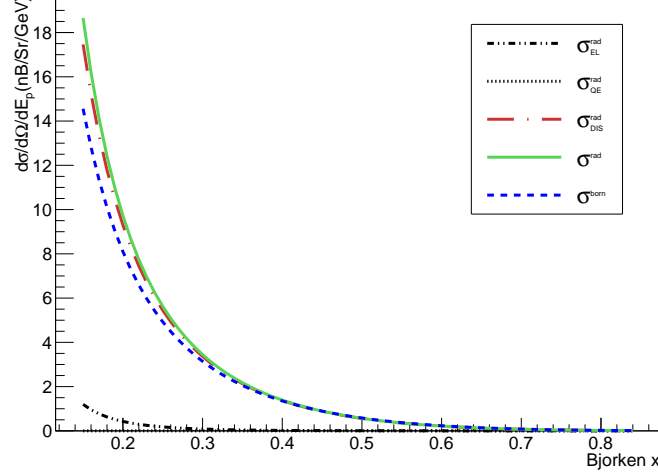


Figure 4.19: ${}^3\text{H}$ Born cross section σ_{model}^{born} and radiative cross section σ_{model}^{rad} from model with $Q^2 = 14x$ (similar to the MARATHON kinematic settings). Contributions from the elastic tail (σ_{EL}^{rad}), quasi-elastic tail (σ_{QE}^{rad}) and DIS (σ_{DIS}^{rad}) to the radiative cross section are shown.

The kinematic coverage of the MARATHON experiment is similar to the SLAC proton and deuterium DIS experiments [19]. Even though Whitlow *et al.* did a global reanalysis of F_2^p and F_2^d with higher statistics and better systematic control, this fit doesn't include the resonance region, with a cut $W^2 > 3 \text{ GeV}^2$ [72]. In the MARATHON experiment, we use a fit by Bodek *et al.* [19] which includes both the DIS and resonance regions. The format of F_2^d and F_2^p are the same as in Eq.(5.1) in [19] with the DIS parameters given in TABLE VIII. The ${}^3\text{H}$ and ${}^3\text{He}$ structure functions are built from F_2^d using the ${}^3\text{H}$ and ${}^3\text{He}$ EMC ratios:

$$F_2^{3\text{H}} = F_2^d \cdot R({}^3\text{H}) \quad R({}^3\text{H}) = \frac{F_2^{3\text{H}}}{F_2^d} \quad (4.31)$$

$$F_2^{3\text{He}} = F_2^d \cdot R({}^3\text{He}) \quad R({}^3\text{He}) = \frac{F_2^{3\text{He}}}{F_2^d} \quad (4.32)$$

$R({}^3\text{H})$ and $R({}^3\text{He})$ are the EMC ratios taken from S. Kulagin and R. Petti [10][73] (KP - or K&P - see Fig.A.3). The KP model does appear to be in excellent agreement with the raw cross section

ratio measurements without applying any large nuclear corrections. The inelastic born cross section is then computed using the F_2 with the assumption that $R = \sigma_L/\sigma_T = 0.18$:

$$\sigma_{born}^{DIS\ model} = \frac{4\alpha^2 E_p^2}{Q^4} \cos^2\left(\frac{\theta}{2}\right) F_2 \left[\frac{1}{\nu} + \frac{1 + Q^2/\nu^2}{xM(1 + R)} \tan^2\left(\frac{\theta}{2}\right) \right] \quad (4.33)$$

Other F_2^p , F_2^d and EMC models are also used to evaluate the systematic uncertainty from model dependence. More details are presented in Appendix A.

4.6 Coulomb correction

The Born cross section formula given by theory is based on the assumption that the wave functions of the incident and scattered electrons are described by plane waves. However, the Coulomb field of the target particles will distort the wave function. This Coulomb effect shifts the Q^2 value of the interaction to an ‘‘effective’’ value, given by [74]:

$$Q_{eff}^2 = Q^2 \left(1 + \frac{3Z\alpha\hbar c}{2RE} \right)^2 \quad (4.34)$$

where Z is the nuclear charge and R is the hard-sphere equivalent radius of the nucleus. R is equal to $(\frac{5}{3} \langle r^2 \rangle)^{1/2}$, where $\langle r^2 \rangle$ is the root-mean-squared radius of the nucleus. The Coulomb correction to the cross section is calculated by using the cross section model presented in Section 4.5.1:

$$C_{coul} = \frac{\sigma^*(x, Q^2)}{\sigma^*(x, Q_{eff}^2)} \quad (4.35)$$

where σ^* denotes the model cross section, and Q^2 is the average Q^2 of a bin. This correction is applied by multiplying the yield with the correction factor.

4.7 Bin centering and combination of kinematics

In the kinematics of the MARATHON experiment, the Q^2 dependence of the structure function is negligible. Therefore, the yield is binned in x only. The size of the bins are varied for different

kinematics to optimize the statistical uncertainty over the measured range. The yields of different targets use the same bins. Once the cross section ratio is extracted as the yield ratio with all the corrections applied, which x the data point corresponds to must be determined. Since the average x within a bin from different targets are essentially the same, it is used as the bin value. The average x includes both the acceptance and the cross section information similar to the yield. The results for the Born cross section ratios for each kinematic setting as a function of x are shown in Fig.4.20 to Fig.4.23 with only statistical uncertainty included. The x value for each bin represents the average x .

The measured ratio is the ratio for the average cross sections. In order to combine the data points which have similar average x , the average cross sections must be converted to the value at a specific x . This is called the bin centering correction and it is done using the cross section model presented in Section 4.5.1:

$$C_{bc} = \frac{\sigma^*(x, Q^2)}{\int \sigma^*(x, Q^2) dx} \quad (4.36)$$

where σ^* is the model cross section, and Q^2 is the average Q^2 of the bin.

The ratio between the cross sections from different targets at a given x with bin centering correction applied is expressed by:

$$R(x) = \frac{\sigma_1(x)}{\sigma_2(x)} = \frac{Y_1(\Delta x)}{Y_2(\Delta x)} \cdot \frac{C_{bc}^1}{C_{bc}^2} \quad (4.37)$$

The bin centering correction factors applied to ${}^2\text{H}/{}^1\text{H}$ cross section ratio are less than 1.1%, and those applied to ${}^3\text{He}/{}^2\text{H}$, ${}^3\text{H}/{}^2\text{H}$ and ${}^3\text{H}/{}^3\text{He}$ ratios are less than 0.8%.

The final ratio at a given x is the weighted average of the ratios corresponding to that x [72]:

$$\overline{R(x)} = \frac{\sum_i w_i R_i(x)}{\sum_i w_i}, \quad \delta^k = \frac{\sqrt{\sum_i (w_i \delta_i^k)^2}}{\sum_i w_i} \quad (4.38)$$

with

$$w_i = \frac{1}{(\delta_i^{stat})^2} \quad (4.39)$$

where i denotes the points, and δ_i^k represents the uncertainties on $R_i(x)$ from different sources k . The weight w_i is determined by the statistical uncertainty (δ_i^{stat}). The systematic errors (δ^k) on the final value are obtained by propagating δ_i^k . The relative systematic errors are added in quadrature to get the total systematic error.

4.8 Experimental uncertainties

Every measured physics variable and applied correction results in a systematic error on the cross section. Some of them are canceled in the ratio, while others lead to an uncertainty in the ratio.

The uncertainties of the beam energy, measured momentum and the scattering angle will shift the real x value, which in turn will affect the corrections that are related to x and change the ratio. The accuracy of the beam energy measurement is around 5×10^{-4} . This results in a relative change in x by about 2×10^{-4} . The momentum resolution is 4×10^{-4} , which induces a relative 5.7×10^{-4} shift in x . The resolution of the scattering angle measurement is dominated by the uncertainty of the spectrometer central angle θ_0 read from EPICS, which is about 0.001° . This leads to a shift in x less than 1×10^{-4} . These 0.01% shifts on x have a negligible effect on the ratio. Therefore, the uncertainties induced by the beam energy, measured momentum and the scattering angle are ignored.

The uncertainty of the total charge measurement comes from the precision of the BCM measurement, which is about 1%. Since the BCM at our production current range is independent of the current, the uncertainty is canceled in the ratio.

The uncertainties of the gas thickness given in Table 3.2 result in an overall shift of the ratios. The effects are calculated by the error propagation function:

$$\frac{\delta R}{R} = \sqrt{\left(\frac{\delta\tau_1}{\tau_1}\right)^2 + \left(\frac{\delta\tau_2}{\tau_2}\right)^2} \quad (4.40)$$

The gas thickness uncertainties lead to 0.79% uncertainty in $\sigma(^2\text{H})/\sigma(^1\text{H})$, 1.20% uncertainty in

$\sigma(^3\text{He})/\sigma(^2\text{H})$, 1.12% uncertainty in $\sigma(^3\text{H})/\sigma(^2\text{H})$ and 1.44% uncertainty in $\sigma(^3\text{H})/\sigma(^3\text{He})$.

The uncertainty induced by the boiling corrections on the ratio is calculated from the variance-covariance matrix of the fit functions Eq.(4.10). As the luminosity is determined for each kinematic setting, this uncertainty remains the same for points at that same kinematic setting. The uncertainty due to the boiling corrections on the ratios is less than 0.4%.

The poor reconstruction near the edges of the spectrometer from the uncertainty of the optics matrix cause a loss in the electron reconstruction. The resulting uncertainty on the ratio is studied by applying different acceptance cuts. The relative uncertainty is found to be less than 0.2%.

The uncertainty from the end cap contamination mostly comes from the end cap thickness uncertainty given in [66]. Especially for the downstream end cap of the gas cell, the uncertainty in the thickness is about 20%. The resulting uncertainty on the Y_{EM}^{Corr} is calculated similarly to Eq.(4.40), which is less than 20%. The uncertainty in the ratio coming from the end cap contamination depends on the percentage of the contamination, which decreases when x increases. The relative uncertainty is less than 0.3% on average since most of these events are removed with cuts.

The uncertainty in the charge symmetric background is dominated by the statistical uncertainty, and the correction factors on the ratios are tiny (less than 0.2%). The uncertainty induced by this correction is negligible.

The uncertainty from the tritium decay correction is different between $\sigma(^3\text{H})/\sigma(^3\text{He})$ and $\sigma(^3\text{H})/\sigma(^2\text{H})$. As can be seen in the Eq.(4.24) and Eq.(4.25), the systematic uncertainty of the former comes mainly from f_{He} where the half life of tritium has an uncertainty, while the uncertainty of the latter is not only due to f_{He} but also the uncertainty of $Y_{^3\text{He}}/Y_{^2\text{H}}$. The relative uncertainty in f_{He} is estimated by:

$$\frac{\Delta f_{He}}{f_{He}} = \frac{f_{He}(\tau + \Delta\tau) - f_{He}(\tau)}{f_{He}(\tau)} \quad (4.41)$$

where $\Delta\tau$ is 8 days. The result is about 0.2%. The uncertainty on the cross section ratio caused by this is negligible. The relative uncertainty on the $\sigma(^3\text{H})/\sigma(^2\text{H})$ from the $Y_{^3\text{He}}/Y_{^2\text{H}}$ uncertainty is

estimated by error propagation:

$$\frac{\Delta R(^3\text{H}/^2\text{H})}{R(^3\text{H}/^2\text{H})} = \frac{\sum_i Q_i f_{He_i}}{\sum_i Q_i (1-f_{He_i})} \cdot \Delta\left(\frac{Y_{^3\text{He}}}{Y_{^2\text{H}}}\right) \quad (4.42)$$

The coefficient is less than 2.6%, and assuming the relative error on $Y_{^3\text{He}}/Y_{^2\text{H}}$ is 3%, then the relative uncertainty on $\sigma(^3\text{H})/\sigma(^2\text{H})$ is less than 0.1%.

The uncertainty on the cross section ratio from radiative corrections can be divided into two parts. One is from the uncertainty in the cross section model, which has been discussed in Appendix A. It is less than 0.35%. The other part is from the Mo&Tsai method. The theoretical uncertainty of the internal correction is smaller than 1.4% [72], and should have negligible contribution to the cross section ratios for light nuclei. The uncertainty for the external radiative correction depends on the length of the electron path. In our experiment, it is similar between different targets. Therefore, the uncertainty cancels in the ratio.

The shift in the Q^2 due to the Coulomb correction is very small (less than 0.004 GeV²). The structure function has little dependence on Q^2 in the MARATHON kinematics. Therefore, the uncertainty on the Coulomb correction due to the cross section model is negligible.

The uncertainty of the bin centering correction comes from the model cross section. It is studied by using different models. The bin centering correction depends heavily on the shape of the model cross section. As the EMC ratios extracted from our data agree well with the KP model, it is used as the EMC ratios to build $F_2^{^3\text{H}}$ and $F_2^{^3\text{He}}$. Since only the DIS Born cross section is utilized in the bin centering correction, Whitlow's F_2 model [72] is applied as the other option. The deviation on the bin centering correction is less than 0.08% for $^2\text{H}/^1\text{H}$. For the EMC ratios, it is negligible when $x < 0.75$, and is less than 0.025% at high x . For $^3\text{H}/^3\text{He}$, the uncertainty is negligible.

A summary of the systematic uncertainties on the cross section ratios is shown in Table 4.1.

Source	$\frac{\delta R}{R} \left(\frac{\sigma(^2\text{H})}{\sigma(^1\text{H})} \right)$	$\frac{\delta R}{R} \left(\frac{\sigma(^3\text{He})}{\sigma(^2\text{H})} \right)$	$\frac{\delta R}{R} \left(\frac{\sigma(^3\text{H})}{\sigma(^2\text{H})} \right)$	$\frac{\delta R}{R} \left(\frac{\sigma(^3\text{H})}{\sigma(^3\text{He})} \right)$
Beam energy	-	-	-	-
HRS momentum	-	-	-	-
Scattering angle	-	-	-	-
Beam current	-	-	-	-
Target boiling	< 0.40%	< 0.32%	< 0.3%	< 0.3%
Acceptance	0.2%	0.2%	0.2%	0.2%
Endcap contamination	0.3%	0.3%	0.3%	0.3%
Charge symmetric background	-	-	-	-
Tritium decay	-	-	< 0.1%	-
Radiative Correction	0.26%	0.25%	0.3%	0.35%
Coulomb Correction	-	-	-	-
Bin centering	0.08%	< 0.02%	< 0.02%	-
Target density*	0.79%	1.20%	1.12%	1.44%
total**	< 0.61%	< 0.54%	< 0.56%	< 0.58%

* The uncertainties induced by target density uncertainties are considered as the normalization uncertainty. They will be examined in Section 5.1.2.

** The total systematic uncertainties do not include the normalization uncertainties.

Table 4.1: Systematic uncertainties on the cross section ratios

4.9 Cross section ratios

The cross section ratios for each kinematic setting are shown in Fig.4.20 to Fig.4.23 with statistical uncertainties only. The results show good agreement between nearby kinematics. The statistical uncertainty at low x is lower than 1%, and rises up to 2% at the highest x . The statistical uncertainty can be reduced by combining nearby kinematic points.

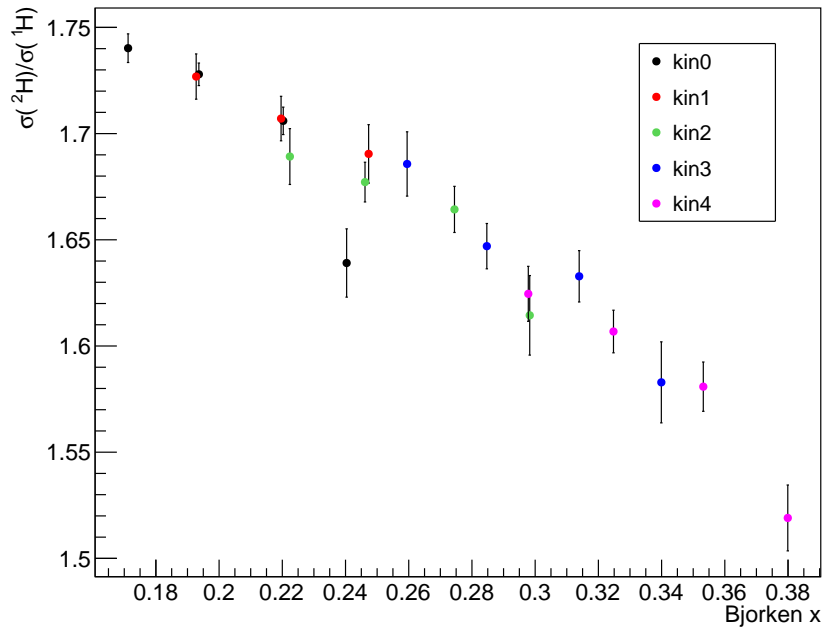


Figure 4.20: $\sigma(^2\text{H})/\sigma(^1\text{H})$ for each kinematic setting (only statistical uncertainties are included)

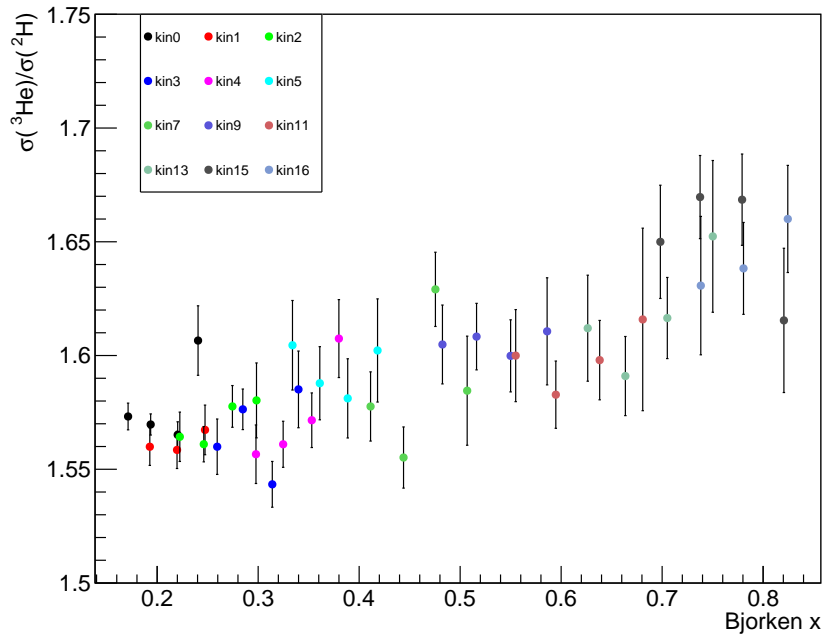


Figure 4.21: $\sigma(^3\text{He})/\sigma(^2\text{H})$ for each kinematic setting (only statistical uncertainties are included)

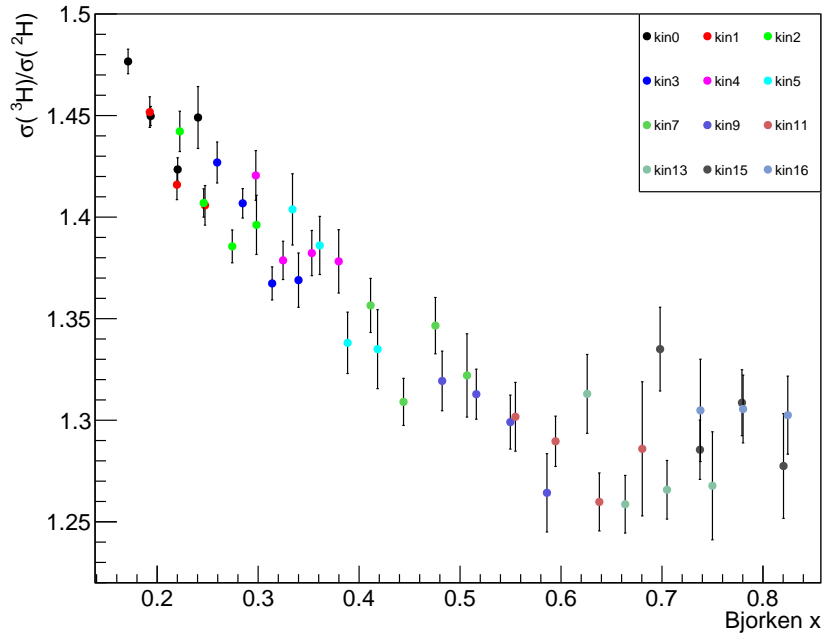


Figure 4.22: $\sigma(^3\text{H})/\sigma(^2\text{H})$ for each kinematic setting (only statistical uncertainties are included)

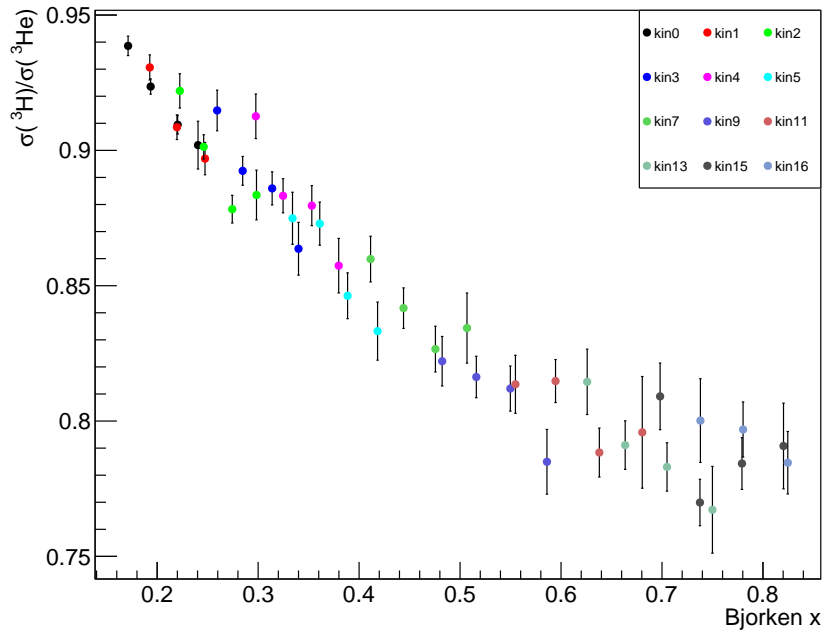


Figure 4.23: $\sigma(^3\text{H})/\sigma(^3\text{He})$ for each kinematic setting (only statistical uncertainties are included)

The results after combining nearby points are shown in Fig.4.24 to Fig.4.27. The statistical uncertainty and the systematic uncertainty are added in quadrature. The systematic uncertainty does not include the normalization uncertainty coming from the target density correction.

The $\sigma(^2\text{H})/\sigma(^1\text{H})$ ratio is well measured over a large kinematic range (x up to 0.9). Many models have been developed to describe the data. The comparison between $\sigma(^2\text{H})/\sigma(^1\text{H})$ from the MARATHON experiment and those from global fits are shown in Fig.4.24. The ‘‘Whitlow’’,

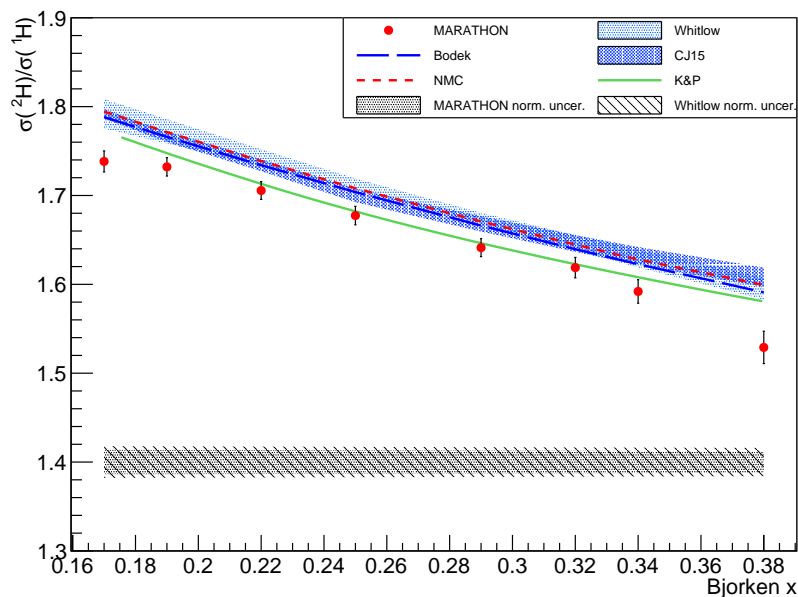


Figure 4.24: $\sigma(^2\text{H})/\sigma(^1\text{H})$ result as a function of x . The MARATHON result (red circles) is compared with the $\sigma(^2\text{H})/\sigma(^1\text{H})$ from global fits. The 0.79% normalization uncertainty is not included in the uncertainty bar.

‘‘Bodek’’, and ‘‘NMC’’ fits are parameterizations of proton and deuteron structure function data. The ‘‘Whitlow’’ fit includes eight SLAC DIS experiments on ^1H and ^2H [72], where the error band is a composite of statistical and systematic uncertainties. The systematic uncertainty is determined by comparing the difference between the results from the two fitting models. The normalization uncertainty on $\sigma(^2\text{H})/\sigma(^1\text{H})$ from the Whitlow fit is about 1% and is not included in the uncertainty band. It is comparable with the normalization uncertainty for the MARATHON result (0.8%). The data set used in the ‘‘Bodek’’ fit comes from three SLAC DIS experiments, which have less statistics than what is used in the Whitlow fit and a larger systematic uncertainty due to the radiative

correction procedure applied. The NMC data covers a large range of x and Q^2 . Not only the NMC data, but also data from SLAC and BCDMS [75] are included in the NMC fit. While the uncertainty provided by the NMC collaboration applies to the structure functions individually, the uncertainty on the ratio should be less, and is not shown in the figure. On the other hand, the CJ15 fit parameterizes the parton distribution functions (PDFs) [48]. It includes not only DIS data but also high energy data from Fermilab. The structure function is then built from the PDFs. The fit from K&P is also based on PDFs [10], which is different from CJ15. The MARATHON result agrees with global fits within experimental uncertainties. The KP model gives the best description for the MARATHON data. This suggests that our systematic uncertainty is under control.

The EMC effect on helium-3 has only been measured by HERMES [76] and JLab E03-103 [33] before the MARATHON experiment. However, the published result from the HERMES experiment has the isoscalar correction applied. The comparison between the $\sigma(^3\text{He})/\sigma(^2\text{H})$ from the MARATHON experiment and JLab E03-103 is shown in Fig.4.25. The uncertainty on the

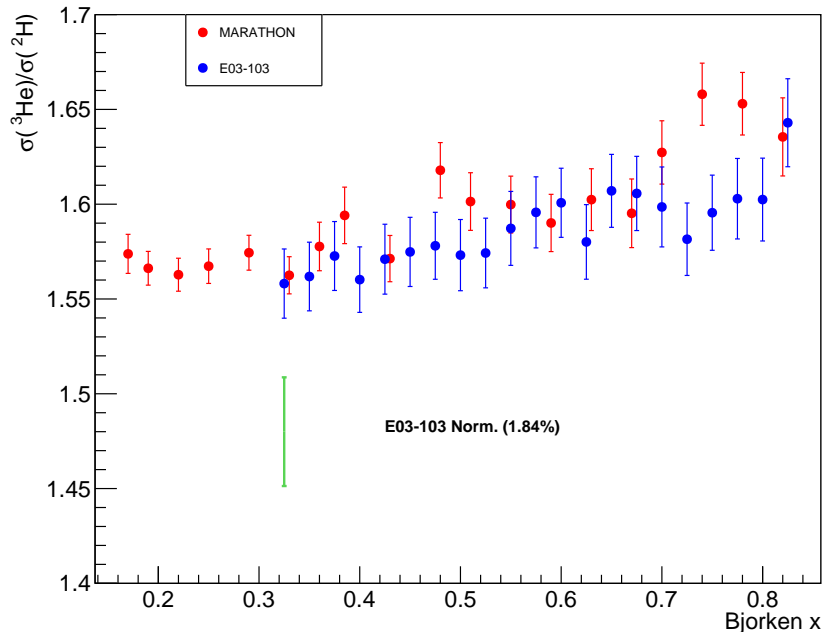


Figure 4.25: $\sigma(^3\text{He})/\sigma(^2\text{H})$ as a function of x . The MARATHON result (red circles) is compared with that from JLab E03-103 experiment (blue circles). The claimed 1.2% normalization uncertainty is not included.

MARATHON result is similar to that of E03-103. Note that in the high x range of E03-103 ($x > 0.6$), this is not considered as deep inelastic scattering anymore since the W^2 value is too low. The normalization uncertainty for the results is not included. The agreement between the two experiments is reasonable.

The MARATHON experiment is the first DIS measurement using a tritium target. The $\sigma(^3\text{H})/\sigma(^2\text{H})$ result shows a clear EMC effect for ^3H (see Fig.4.26). The uncertainty for the ^3H EMC ratio is comparable to that of ^3He . The $\sigma(^3\text{H})/\sigma(^3\text{He})$ decreases as x increases (see Fig.4.27), which agrees with the fact that F_2^n/F_2^p decreases as x increases. The neutron inside ^3H has a softer distribution than the mirror proton inside the ^3He . Ignoring the normalization uncertainty, the total uncertainty on $\sigma(^3\text{H})/\sigma(^3\text{He})$ is less than 1.4%.

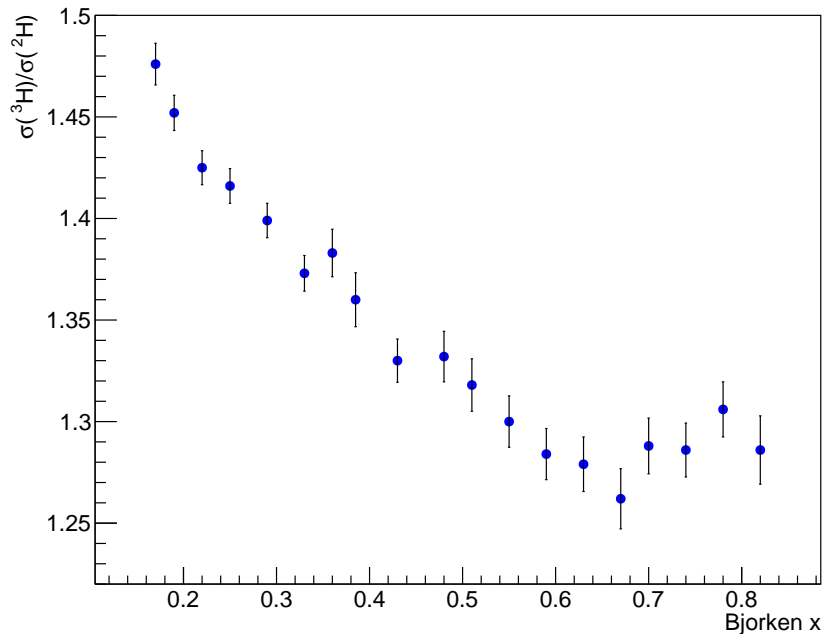


Figure 4.26: $\sigma(^3\text{H})/\sigma(^2\text{H})$ as a function of x . The claimed 1.12% normalization uncertainty is not included.

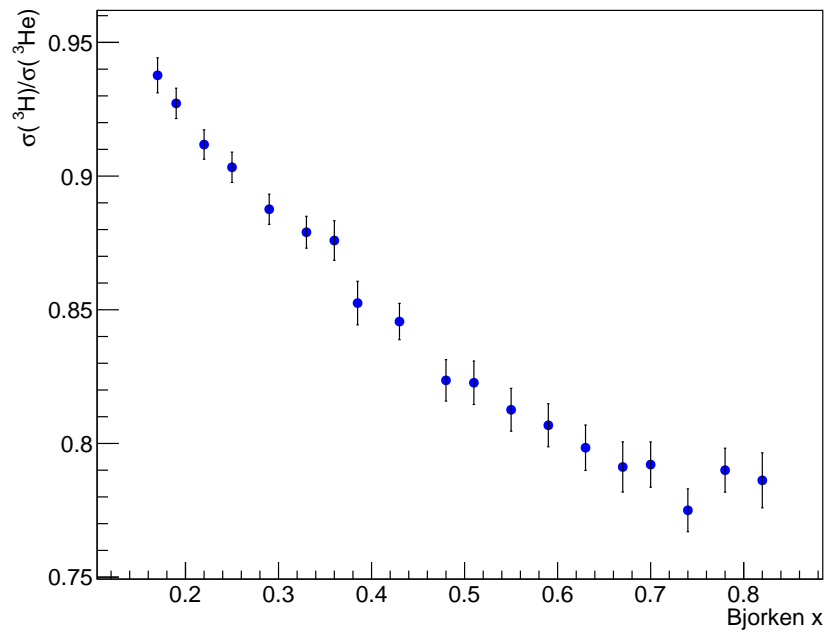


Figure 4.27: $\sigma(^3\text{H})/\sigma(^3\text{He})$ as a function of x . The claimed 1.44% normalization uncertainty is not included.

Chapter 5: Results

5.1 F_2^n/F_2^p results

The nuclear structure function F_1 in Eq.(2.20) is related to F_2 by the expression:

$$F_1 = \frac{F_2(1 + Q^2/\nu^2)}{2x(1 + R)}, \quad (5.1)$$

where $R = \sigma_L/\sigma_T$ is the ratio of the virtual photoabsorption cross sections for longitudinally and transversely polarized photons. Replacing F_1 in the cross section formula Eq.(2.20) by Eq.(5.1) gives:

$$\sigma = \frac{4\alpha^2 E_p^2}{Q^4} \cos^2\left(\frac{\theta}{2}\right) F_2 \left[\frac{1}{\nu} + \frac{1 + Q^2/\nu^2}{xM(1 + R)} \tan^2\left(\frac{\theta}{2}\right) \right]. \quad (5.2)$$

The measurements of R by SLAC, NMC and HERMES using multiple nuclear targets show no A dependence in the MARATHON kinematics [77][78][79][80]. So we assume that R is equal for different nuclei. Then the ratio of the F_2 structure functions between nuclei is equal to their cross section ratios, for example:

$$\frac{F_2^{3\text{H}}}{F_2^{3\text{He}}} = \frac{\sigma(^3\text{H})}{\sigma(^3\text{He})}. \quad (5.3)$$

5.1.1 F_2^n/F_2^p extraction

If the distributions of proton and neutron remain the same inside different nuclei, then F_2^n/F_2^p could be extracted directly from the ratio of the nuclei structure functions. However, the EMC effect demonstrates that the nucleon structure functions are modified by the nuclear medium and vary between different nuclei. In order to extract the free nucleon structure function ratio F_2^n/F_2^p ,

firstly let's define a EMC-type ratio for a nucleus [12], A_ZX , as:

$$R_{AZ} = \frac{F_2^{AZ}}{ZF_2^p + (A-Z)F_2^n}, \quad (5.4)$$

where F_2^{AZ} is the nuclear structure function measured from the experiment, and F_2^n and F_2^p are the free neutron and proton structure functions. This ratio effectively characterizes how large the nuclear effect is inside the nucleus, and it can only be found from theory calculations (see Fig.5.1). Once the EMC-type ratio is known, it can be used to extract the F_2^n/F_2^p ratio from the nuclei structure function ratios.

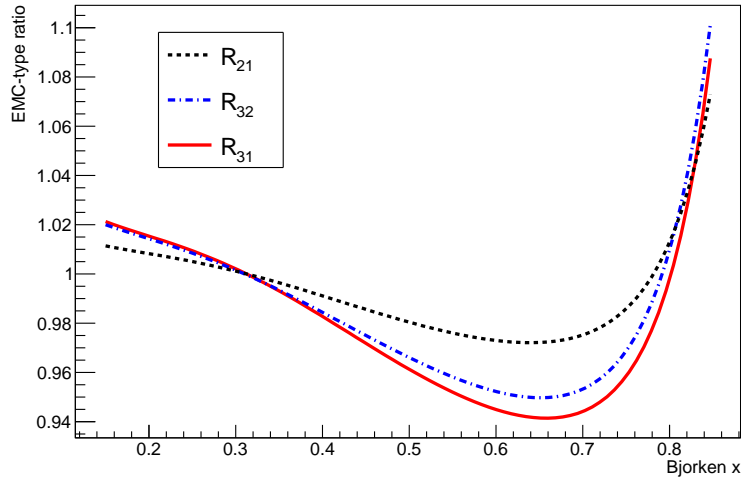


Figure 5.1: The EMC-type ratios for ${}^2\text{H}$, ${}^3\text{He}$ and ${}^3\text{H}$ from the KP model

For the MARATHON experiment, the goal is to find F_2^n/F_2^p from the tritium over helium-3 cross section ratio, as the difference in nuclear corrections for the two mirror nuclei should be small. But before doing that, we would like to extract the F_2^n/F_2^p from the deuteron over proton ratio at low x ($x < 0.6$), where the nuclear effect is well understood, in order to check the overall systematic uncertainty.

F_2^n/F_2^p from F_2^d/F_2^p

The EMC-type ratio for the deuteron is expressed by:

$$R_{21} = \frac{F_2^d}{F_2^n + F_2^p}. \quad (5.5)$$

From Eq.(5.5), F_2^n/F_2^p is extracted from F_2^d/F_2^p by:

$$\frac{F_2^n}{F_2^p} = \frac{F_2^d/F_2^p}{R_{21}} - 1 \quad (5.6)$$

The result is shown in Fig.5.2. It agrees well with the KP model.

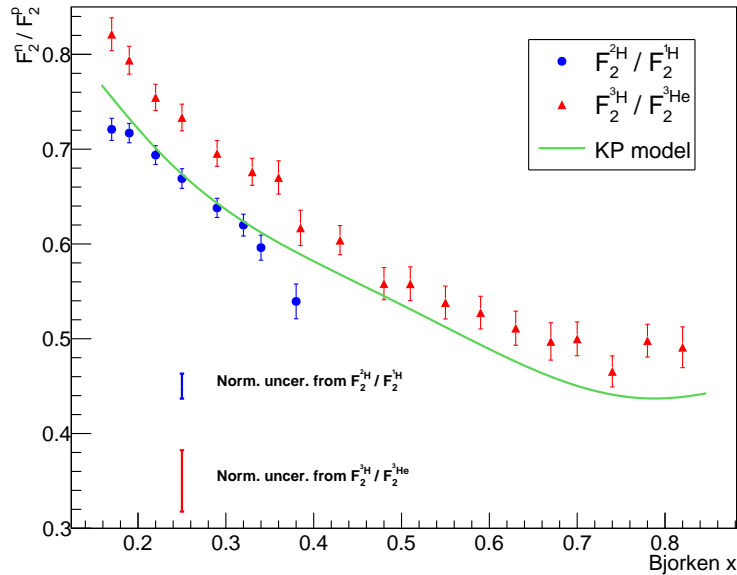


Figure 5.2: F_2^n/F_2^p extracted from F_2^{3H}/F_2^{3He} and F_2^{2H}/F_2^{1H}

F_2^n/F_2^p from F_2^{3H}/F_2^{3He}

The EMC-type ratio for ^3H and ^3He are defined as:

$$R_{31} = \frac{F_2^{3H}}{F_2^p + 2F_2^n}, \quad R_{32} = \frac{F_2^{3He}}{2F_2^p + F_2^n}. \quad (5.7)$$

From Eq.(5.7), the F_2^n/F_2^p is found from $F_2^{3\text{H}}/F_2^{3\text{He}}$ by:

$$\frac{F_2^n}{F_2^p} = \frac{1/\mathcal{R} - 2F_2^{3\text{H}}/F_2^{3\text{He}}}{F_2^{3\text{H}}/F_2^{3\text{He}} - 2/\mathcal{R}}, \quad (5.8)$$

where \mathcal{R} is R_{32}/R_{31} , called ‘‘super-ratio’’. It represents the nuclear effects difference between ^3H and ^3He , which should be small for the mirror nuclei [81]. As can be seen in Fig.5.3, \mathcal{R} calculated by K&P is indeed around 1, and only goes up to 1.01 at the highest x point. The nuclear corrections considered in the KP model include the off-shell correction, the target mass correction, higher-twist correction, and nuclear meson-exchange current correction which only produces a small correction when $x < 0.2$.

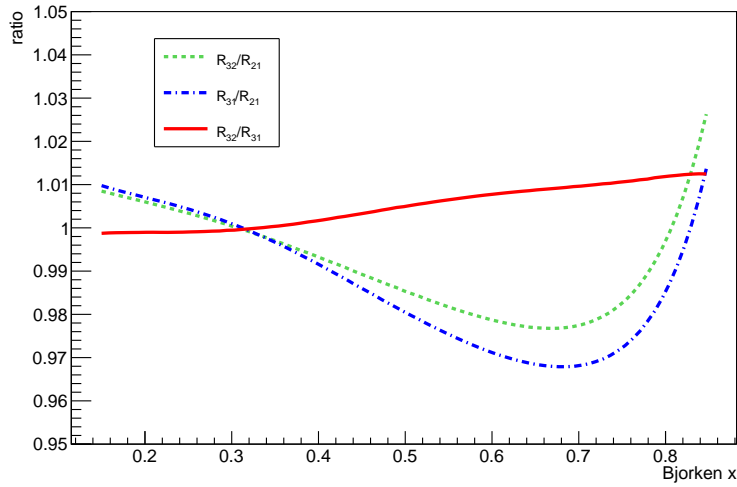


Figure 5.3: The ratios between EMC-type ratios from KP model

The F_2^n/F_2^p results are given in Fig.5.2. The F_2^n/F_2^p ratio obtained from ^3H and ^3He cross section ratio is higher than that from the deuteron and proton ratio, but they seem to match after a vertical shift, and have a similar shape as the KP model. This normalization difference is discussed in the following section.

5.1.2 Normalization

Since nuclear effects for different nuclei are similar near $x = 0.3$, the ratio F_2^n/F_2^p extracted from different nuclear structure function ratios should be same in that range. The difference between the ratio F_2^n/F_2^p extracted from ${}^3\text{H}/{}^3\text{He}$ and d/p likely comes from a normalization uncertainty induced by a target density mismeasurement (at the two standard deviations level). Unlike other systematic uncertainties which are measured during the experiment, the uncertainty in the target density measurement is found by an engineering procedure during the cell filling, using the ideal gas law. The systematic uncertainties induced by the target densities provided by the target group are dominant (1.0% – 1.5%) in the total systematic uncertainties. In order to find the origin of this normalization difference, we extract F_2^n/F_2^p from $F_2^{3\text{H}}/F_2^{2\text{H}}$ and $F_2^{3\text{He}}/F_2^{2\text{H}}$ near $x = 0.3$.

F_2^n/F_2^p from $F_2^{3\text{H}}/F_2^{2\text{H}}$

From the EMC-type ratios for ${}^3\text{H}$ and ${}^2\text{H}$ given in Eq.(5.7) and Eq.(5.5), the F_2^n/F_2^p is extracted from $F_2^{3\text{H}}/F_2^{2\text{H}}$ by:

$$\frac{F_2^n}{F_2^p} = \frac{F_2^{3\text{H}}/F_2^{2\text{H}} - R_{31}/R_{21}}{2R_{31}/R_{21} - F_2^{3\text{H}}/F_2^{2\text{H}}}. \quad (5.9)$$

The result is shown in Fig.5.4. It agrees with the F_2^n/F_2^p extracted from the deuteron to proton ratio near $x = 0.3$.

F_2^n/F_2^p from $F_2^{3\text{He}}/F_2^{2\text{H}}$

From the EMC-type ratios for ${}^3\text{He}$ and ${}^2\text{H}$ given in Eq.(5.7) and Eq.(5.5), the F_2^n/F_2^p is extracted from $F_2^{3\text{He}}/F_2^{2\text{H}}$ using:

$$\frac{F_2^n}{F_2^p} = \frac{F_2^{3\text{He}}/F_2^{2\text{H}} - 2R_{31}/R_{21}}{R_{31}/R_{21} - F_2^{3\text{He}}/F_2^{2\text{H}}}. \quad (5.10)$$

As shown in Fig.5.4, the F_2^n/F_2^p obtained from $F_2^{3\text{He}}/F_2^{2\text{H}}$ is larger than the others. While the result from $F_2^{3\text{H}}/F_2^{2\text{H}}$ agrees with the F_2^n/F_2^p from $F_2^{2\text{H}}/F_2^{1\text{H}}$, we attribute the normalization difference for the result from the tritium over helium-3 ratio comes from the ${}^3\text{He}$ target density uncertainty.

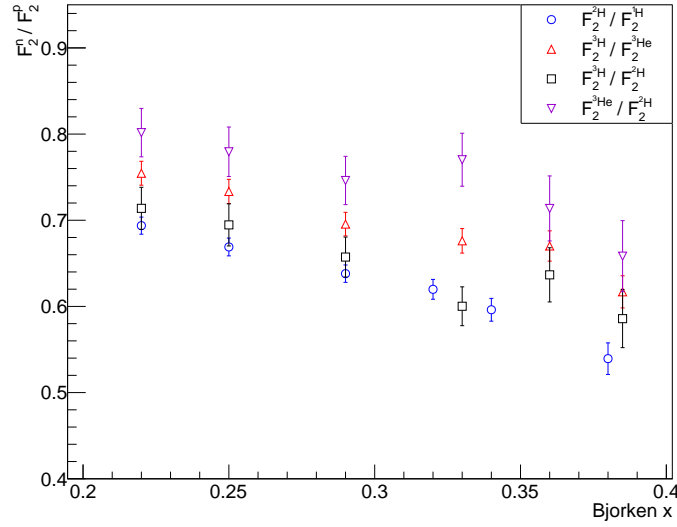


Figure 5.4: F_2^n/F_2^p extracted from F_2^{3H}/F_2^{3He} , F_2^{2H}/F_2^{1H} , F_2^{3H}/F_2^{2H} and F_2^{3He}/F_2^{2H} at low x

Based on the assumption that the nuclear effect cancels around $x = 0.3$, the normalization for each nuclear structure function ratio is decided by comparing the ratio F_2^n/F_2^p from data (R^{data}) to the KP model (R^{KP}) between $x = 0.2$ to $x = 0.4$ and minimizing the χ^2 -like quantity:

$$\sum_i \left(\frac{R^{data}(x_i) - R^{KP}(x_i)}{\delta R^{data}(x_i)} \right)^2. \quad (5.11)$$

The normalization results are shown in Table 5.1, and the ratio F_2^n/F_2^p after normalization is shown in Fig.5.5. The normalization needed for F_2^{2H}/F_2^{1H} and F_2^{3H}/F_2^{2H} are well within their total uncertainties, while F_2^{3He}/F_2^{2H} and F_2^{3H}/F_2^{3He} need to be scaled by 2.4% and -2.6%, respectively. This effectively implies that the target densities for 1H , 2H and 3H require no normalization factor, but the 3He target density requires a 2.4% correction factor.

The uncertainty in the normalization comes from the model dependence on F_2^n/F_2^p and the statistical uncertainty of the data. The model dependence can be determined by comparing the normalization found using different F_2^n/F_2^p models, and to be consistent, all EMC-type ratios should come from same model. However, except for the KP model, the other available model CJ15 [48] has a different F_2^n/F_2^p shape compared to the data, shown in Fig.5.6. In order to use CJ15 model,

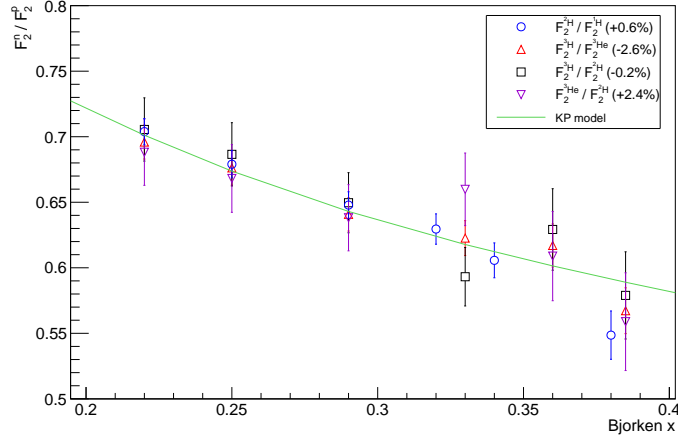


Figure 5.5: F_2^n/F_2^p after normalizing the nuclei structure function ratios

Ratio	Normalization
F_2^{2H}/F_2^{1H}	+0.6%
F_2^{3H}/F_2^{2H}	-0.2%
F_2^{3He}/F_2^{2H}	+2.4%
F_2^{3H}/F_2^{3He}	-2.6%

Table 5.1: The normalization on nuclei structure function ratios

an iteration would have to be applied to eliminate the F_2^n/F_2^p difference on the super-ratio \mathcal{R} calculation [12]; this may be done in a future analysis.

5.1.3 F_2^n/F_2^p results

The ratio F_2^n/F_2^p extracted from F_2^{3H}/F_2^{3He} (presumably) has a small nuclear model dependence. The F_2^{3H}/F_2^{3He} is scaled by a factor of 0.976. The resulting F_2^n/F_2^p ratio is shown in Fig.5.7 together with the KP model. The KP model describes the data fairly well. As can be seen in Eq.(5.8), the uncertainties in the ratio F_2^n/F_2^p come from the tritium over helium-3 structure function ratio and the super-ratio \mathcal{R} . The ratio F_2^{3H}/F_2^{3He} uncertainty is the same as their cross sections ratio uncertainty given in Section 4.8. The uncertainty in the super-ratio \mathcal{R} from the KP model is not available yet. As a reference from [81], the theoretical uncertainty in \mathcal{R} can increase linearly from

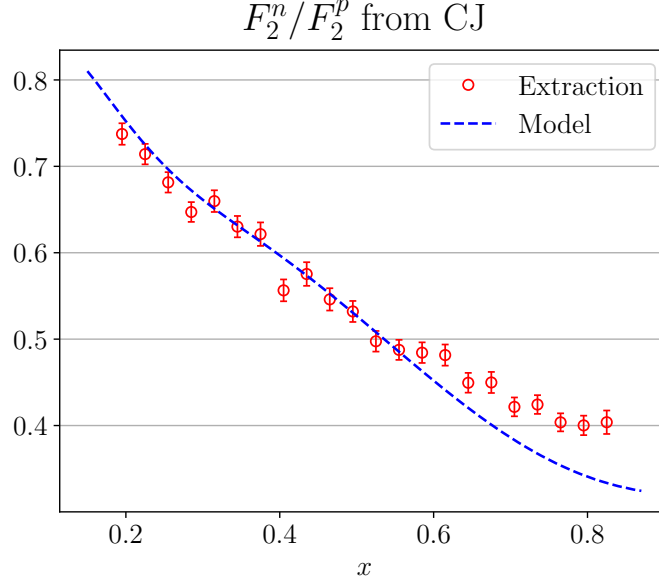


Figure 5.6: F_2^n/F_2^p extracted from renormalized ${}^3\text{H}/{}^3\text{He}$ using CJ15 model. [82]

0% at $x = 0$ to 1% at $x = 0.82$. By neglecting the theoretical uncertainty on \mathcal{R} , the total uncertainty in F_2^n/F_2^p is less than 4.5%, and given in Appendix C Table C.1.

A comparison between the ratio F_2^n/F_2^p from the MARATHON experiment and previous SLAC deuteron experiments which are at similar kinematics are shown in Fig.5.8. In the global reanalysis of the SLAC deuteron and proton DIS data, Whitlow *et al.* [21] included the Fermi smearing in the F_2^n/F_2^p extraction, and studied the model dependence by using three different deuteron wave functions (Paris[83], Reid[84], Bonn[85]). The results start to diverge when $x > 0.65$. At $x = 0.85$, using the Bonn wave function gives a 20% higher ratio than using the Paris wave function, and using the Reid soft core wave function is 15% lower. As mentioned in Section 2.1.2, Melnitchouk and Thomas[20] reanalyzed SLAC data by including more nuclear corrections in the deuteron model, such as binding effects and off-shell corrections, which leads to another different SLAC result shown in Fig.5.8. The ratio F_2^n/F_2^p extracted from $F_2^3\text{H}/F_2^3\text{He}$ is similar to that from Melnitchouk and Thomas[20]. However, no conclusion can be made at this time since higher twist and target mass corrections might change the results significantly.

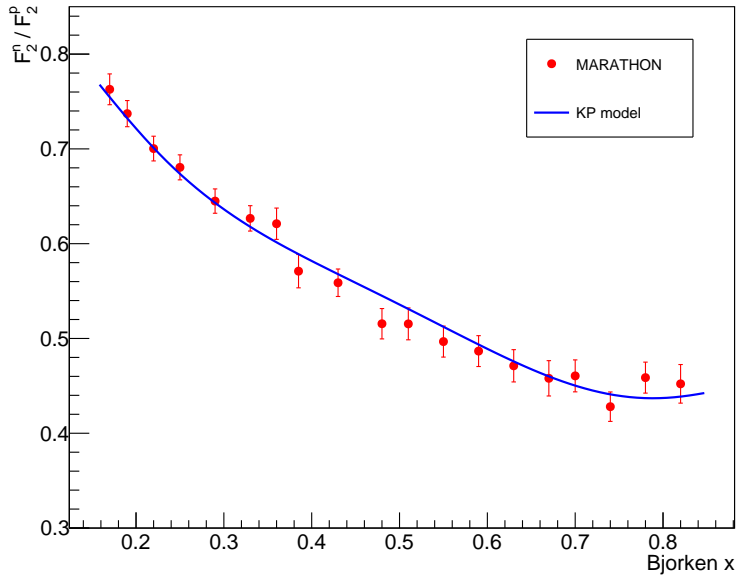


Figure 5.7: F_2^n/F_2^p result after normalization

5.2 EMC effect

The purpose of EMC effect study is to compare the average nucleon structure function inside a nucleus versus inside a deuteron. If a nucleus has an equal number of protons and neutrons, the observable for the EMC effect is the ratio of the nuclear structure function per nucleon to that of the deuteron:

$$\frac{F_2^A/A}{F_2^d/2} \quad (5.12)$$

Since the neutron has a “softer” (lower) distribution than the proton, nuclei with different numbers of protons and neutrons require an isoscalar correction.

5.2.1 Isoscalar correction

An isoscalar correction is applied and uses the measurements of free nucleon structure functions to eliminate the proton excess or neutron excess inside a nucleus. An isoscalar nucleus, with an equal number of protons and neutrons, is constructed after applying the correction. The EMC

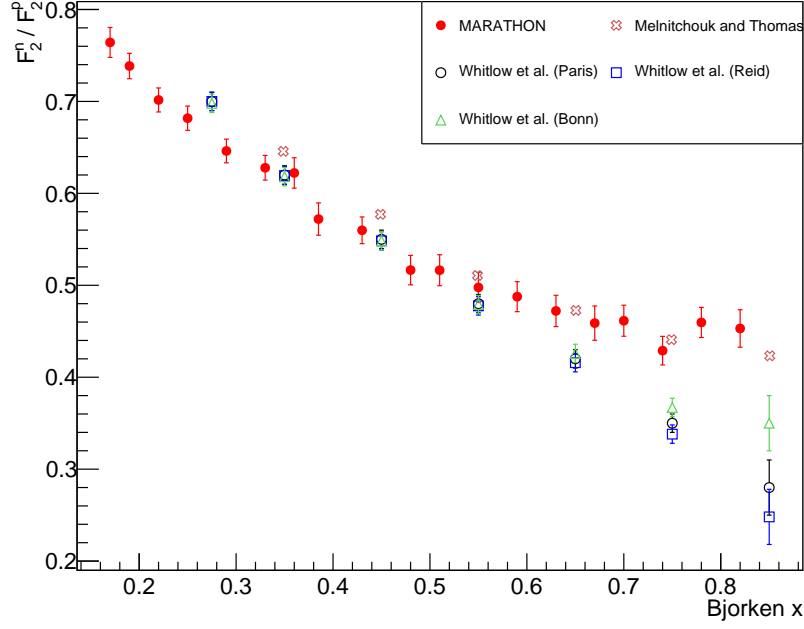


Figure 5.8: Comparison between the F_2^n/F_2^p from the MARATHON experiment and the SLAC experiments (see text).

ratio on the nucleus with the isoscalar correction applied is expressed by:

$$\left(\frac{F_2^A/A}{F_2^d/2} \right)_{iso} = \left(\frac{F_2^A}{F_2^d} \right) \cdot \frac{F_2^p + F_2^n}{ZF_2^p + (A-Z)F_2^n} \quad (5.13)$$

$$= \left(\frac{F_2^A}{F_2^d} \right) \cdot \frac{1 + F_2^n/F_2^p}{Z + (A-Z)F_2^n/F_2^p} \quad (5.14)$$

As can be seen in Eq.(5.14), the isoscalar correction depends on the F_2^n/F_2^p ratio. The ratio F_2^n/F_2^p given in Fig.5.7 has only a small model dependence at large x . Therefore, it is used to make the isoscalar correction on the MARATHON EMC data.

5.2.2 ^3He EMC effect

The EMC effect on helium-3, before and after isoscalar correction, are shown in Fig.5.9. The 2.4% normalization on $F_2^{^3\text{He}}$ is applied. The ^3He EMC ratio crosses 1 around $x = 0.3$, which is consistent with the measurements of the EMC effect on other nuclei. The uncertainties of the

helium-3 EMC ratio come from the uncertainties of $F_2^{3\text{He}}/F_2^{2\text{H}}$ and the isoscalar correction. The ratio $F_2^{3\text{He}}/F_2^{2\text{H}}$ has the same uncertainties as the cross section ratios given in Section 4.8. The isoscalar correction has a F_2^n/F_2^p model dependence; a detailed study can be found in [86]. The study shows that the difference between models can lead to a 2.8% uncertainty on the ^3He EMC ratio and 3.9% on the ^3H EMC ratio at the highest x point. However, some of the F_2^n/F_2^p models are surely not correct at high x . For example, the NMC fit does not include any deuteron nuclear corrections. So in this thesis work, only the experimental uncertainties on the F_2^n/F_2^p given in Table C.1 are included. The results of the helium-3 EMC effect is given in Table C.2, where the systematic uncertainties are probably underestimated.

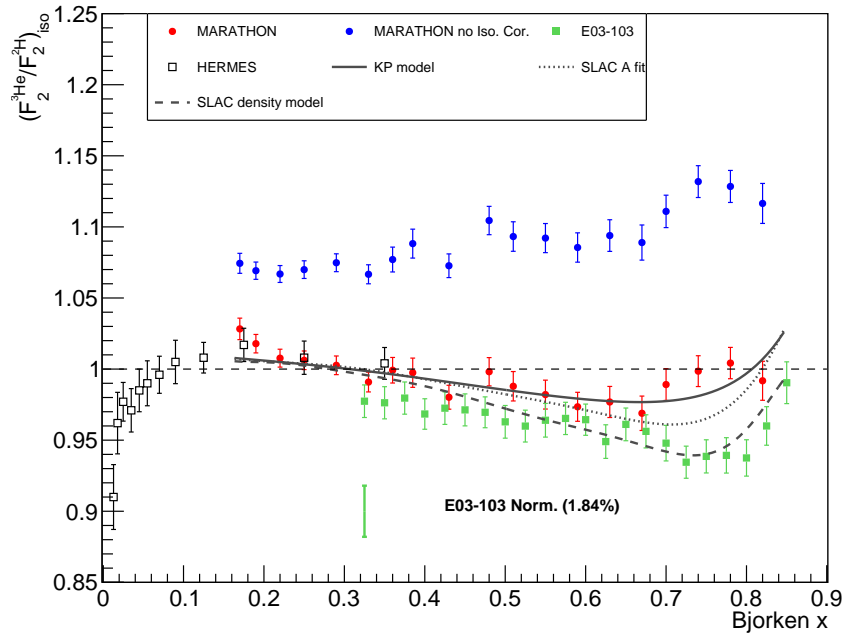


Figure 5.9: ^3He EMC ratio result from the MARATHON experiment compared with the KP model, the SLAC A -dependent fit and the SLAC average nuclear density fit [27]. HERMES [76] and JLab E03-103 [33] ^3He EMC results are also shown. The 2.4% normalization on $\sigma(^3\text{He})$ is applied. The isoscalar correction uncertainty is not included.

The data is compared with the KP model, the SLAC A -dependent fit and the SLAC average nuclear density model [27]. The root-mean-squared radius used for ^3He is 1.88 fm. Both the KP model and the SLAC A -dependent fit [27] are able to describe the slope of the ^3He EMC effect,

but in the range $x > 0.7$, the minimum predicted from the SLAC A -dependent fit is more than 3% lower than the minimum in the data. On the other hand, the average nuclear density model fails to describe the data and gives a lower prediction.

Previous ^3He EMC data from HERMES and JLab E03-103 with isoscalar corrections are also shown. The result from the MARATHON experiment agrees with the HERMES measurement in the overlap region. The result from E03-103 has a similar slope to the MARATHON data, but is lower. S. Kulagin and R. Petti argue that in order to match the F_2^n/F_2^p from the NMC experiment, a 3% normalization is required for the JLab E03-103 ^3He EMC data [87]. If we include this normalization, the data from E03-103 agrees well with the MARATHON result. Note that the W^2 for E03-103 in the range $x > 0.76$ is less than 2 GeV^2 , which corresponds to the resonance region.

5.2.3 ^3H EMC effect

The ^3H EMC effect before and after isoscalar correction is shown in Fig.5.10. This represents

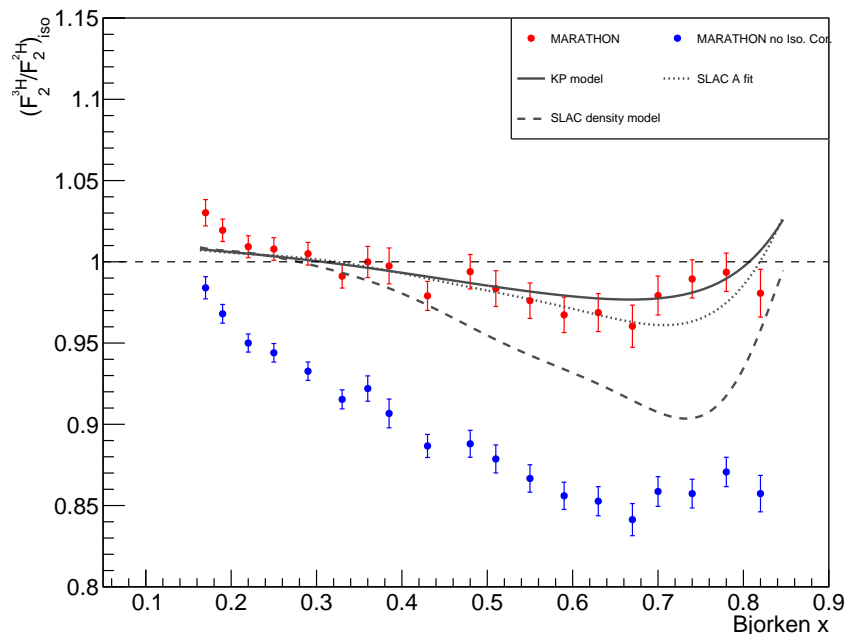


Figure 5.10: ^3H EMC ratio result from the MARATHON experiment compared with the KP model, the SLAC A -dependent fit and the SLAC average nuclear density fit [27]. The 1.12% normalization uncertainty on $\sigma(^3\text{H})/\sigma(^2\text{H})$ and the isoscalar correction uncertainty are not included.

the first measurement of the tritium EMC effect. The isoscalar corrected ${}^3\text{H}$ EMC ratio crosses unity around $x = 0.3$. The uncertainties are calculated in the same way as the ${}^3\text{He}$ EMC ratios. The prediction for the tritium EMC ratios from the KP model and two SLAC fits [27] are also shown in Fig.5.10. The SLAC A -dependent fit describes well the slope for the ${}^3\text{H}$ EMC effect, except when $x > 0.7$, the SLAC fit is 2% lower than the data. The KP model is also able to reproduce the ${}^3\text{H}$ EMC effect. However, the average nuclear density model from SLAC indicates a much lower tritium EMC effect. The root-mean-squared radius used for ${}^3\text{H}$ is 1.68 fm.

The comparison between the EMC effect on ${}^3\text{H}$ and ${}^3\text{He}$ is shown in Fig.5.11. They are similar, which supports the assumption that the difference in the nuclear corrections between tritium and helium-3 is small.

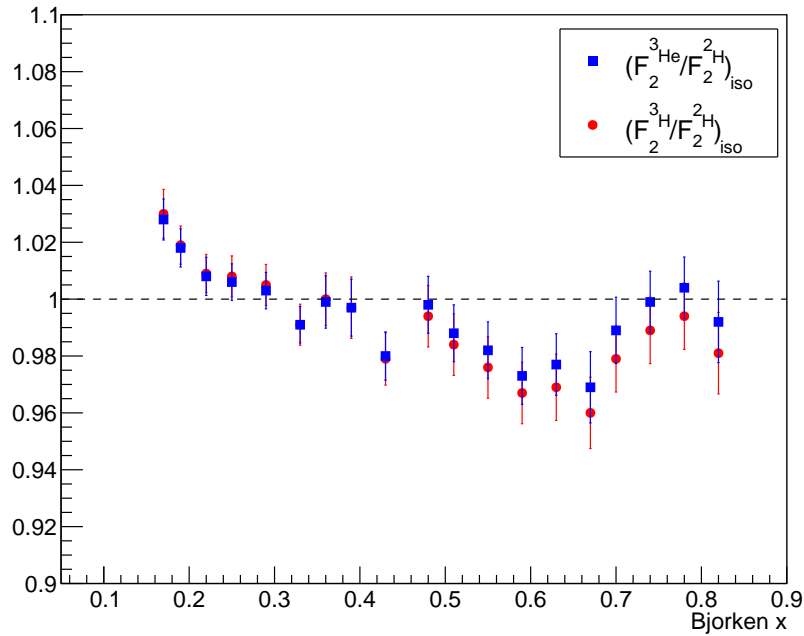


Figure 5.11: Comparison between ${}^3\text{H}$ EMC ratio and ${}^3\text{He}$ EMC ratio. The 2.4% normalization on $\sigma({}^3\text{He})$ is applied.

5.3 Conclusions

In the MARATHON experiment, the ratio F_2^n/F_2^p is extracted from the ratio $F_2^{3\text{H}}/F_2^{3\text{He}}$. Because tritium and helium-3 are mirror nuclei, the nuclear correction difference between them is expected to be small. Therefore, the extracted F_2^n/F_2^p has much smaller nuclear model dependence than previous extractions from deuteron and proton DIS data. The F_2^n/F_2^p obtained from the MARATHON experiment agrees with the F_2^n/F_2^p extracted by Melnitchouk and Thomas[20] using the SLAC deuteron and proton DIS data, which is close to the pQCD predictions for F_2^n/F_2^p as $x \rightarrow 1$. However, no conclusion can be made at this time. In order to extract the leading order F_2^n/F_2^p , the higher order pQCD corrections, high twist effects and the target mass corrections have to be considered, which could have a large effect at large x . This requires additional theoretical calculations.

The EMC ratio for tritium and helium-3 are presented. We have performed the first measurement of the EMC effect in tritium. Both EMC ratios agree with the predictions from the KP model and the SLAC A -dependent fit, while the SLAC average nuclear density model fails to reproduce the data. This supports the concept that the EMC effect is unlikely to be related to the average nuclear density.

One thing to note is that in order to make the F_2^n/F_2^p extracted from tritium and helium-3 agree with that from deuteron and proton around $x = 0.3$, a 2.4% normalization is applied to the helium-3 structure function. The interesting thing is that a 3% normalization is also required in the JLab E03-103 ^3He EMC ratio to match the NMC F_2^n/F_2^p [87]. Including the normalization factor, the KP model describes well the MARATHON data. Their model appears to provide a good reference for the nuclear effects in future study.

Chapter 6: Future project and experiments

Even though nuclear effects largely cancel out when taking the ratio between ${}^3\text{H}$ and ${}^3\text{He}$, the super-ratio \mathcal{R} used in the F_2^n/F_2^p extraction (e.g. Eq.(5.8)) still has model dependence. An alternative method has been put forward [88] to parameterize the free neutron and proton structure functions by analyzing proton, deuteron and $A = 3$ nuclear data. In this way, nuclear effects can be studied. Furthermore, with the upgraded 12 GeV electron beam at JLab, the spectator tagging method will be used in the BONUS12 experiment to directly measure the nearly free neutron structure function [89]. The SoLID collaboration aims to extract the d/u ratio at large x by performing parity-violating deep inelastic scattering (PVDIS) on the proton [90].

6.1 An alternative data analysis method

In the last chapter, the ratio F_2^n/F_2^p is extracted from $F_2^{3\text{H}}/F_2^{3\text{He}}$ following the method given in the MARATHON proposal [12], which uses a theoretical calculation for the super-ratio \mathcal{R} . In the super-ratio \mathcal{R} calculation, the nuclear structure functions are built from free nucleon structure functions by including multiple nuclear corrections, such as nuclear binding effects, Fermi smearing, and the off-shell corrections. The off-shell corrections are determined from parameterization of DIS data, where isospin independence for neutron and proton is assumed. However, if isospin dependence from off-shell effects does occur, it could have a large effect on the super-ratio \mathcal{R} . Tropiano *et al.* [88] tried to fit the isospin dependent off-shell corrections based on the isoscalar off-shell functions obtained from the CJ15 and the KP model using the JLab E03-103 $F_2^{3\text{He}}/F_2^{2\text{H}}$ data. The isoscalar off-shell functions obtained from the CJ15 and the KP model are quite different, which result in dramatically different super-ratio \mathcal{R} predictions at large x , as shown in Fig.6.1. But since the $F_2^{3\text{He}}/F_2^{2\text{H}}$ data used in the fit is only between $0.33 \lesssim x \lesssim 0.58$, the resulting isospin

dependent off-shell functions are not considered reliable.

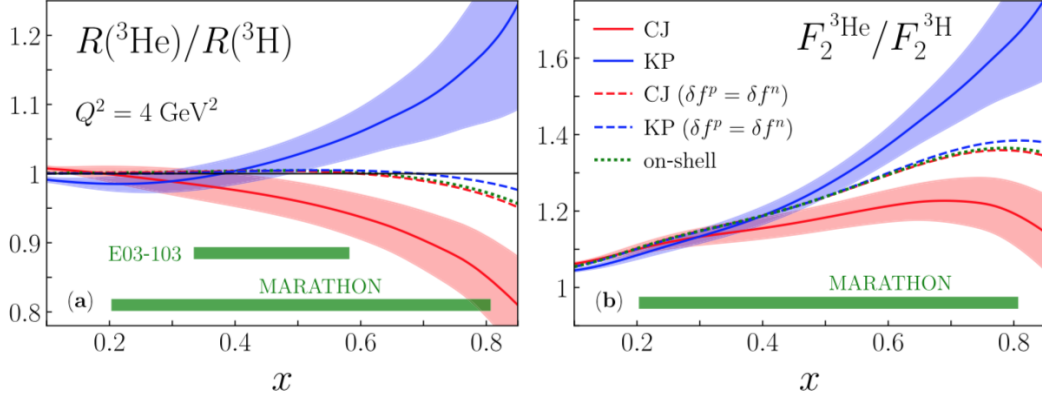


Figure 6.1: Comparison on (a) Super-ratio \mathcal{R} , (b) the ratio $F_2^{^3\text{H}}/F_2^{^3\text{He}}$, between the model with isoscalar off-shell corrections and isospin dependent off-shell corrections. The isoscalar off-shell function is obtained from the CJ15 and the KP model. [88]

An alternative method to extract the ratio F_2^n/F_2^p that avoids the nuclear model dependence is to do a global fit at the structure function level [88]. The nuclear structure function can be expressed as the sum of the on-shell and off-shell contributions:

$$F_2^A(x, Q^2) = F_2^{A(\text{on})}(x, Q^2) + F_2^{A(\text{off})}(x, Q^2). \quad (6.1)$$

The on(off)-shell contributions can be written as:

$$F_2^{A(\text{on})}(x, Q^2) = \sum_N \int dy \left[f_{22}^N(y, \gamma) F_2^N\left(\frac{x}{y}, Q^2\right) \right], \quad (6.2)$$

$$F_2^{A(\text{off})}(x, Q^2) = \sum_N \int dy \left[\widetilde{f}_{22}^N(y, \gamma) F_2^N\left(\frac{x}{y}, Q^2\right) \right] \delta f^N\left(\frac{x}{y}, Q^2\right), \quad (6.3)$$

where f_{22}^N and \widetilde{f}_{22}^N are the on-shell and off-shell smearing functions computed using non-relativistic nucleon spectral functions. The on-shell nucleon structure functions F_2^N and the off-shell functions δf^N can be extracted from data. There are four unknowns: F_2^p , F_2^n , δf^p , δf^n , and we have the global proton and deuteron DIS data together with the $F_2^{^3\text{He}}/F_2^{^2\text{H}}$ and $F_2^{^3\text{H}}/F_2^{^2\text{H}}$ from the

MARATHON experiment which are four available observables. Therefore, the four unknowns can be determined by a global fit.

In this alternative method, not only the free neutron and proton structure functions are parameterized, but also the isospin dependent off-shell functions can be extracted. This method removes potential uncertainties coming from the nuclear effects, and characterizes the isospin dependence from the off-shell corrections.

6.2 The BONUS12 experiment

The BONUS12 experiment [89] is an extension of the JLab 6 GeV experiment E03-012 (BONUS, “Barely Off-shell NUCleon Structure”) [91] at the upgraded 12 GeV CEBAF. It performs semi-inclusive electron scattering off the deuterium target. A recoil detector surrounding the deuterium target is installed to detect the slow protons emitted in the backward direction, and the coincidence electrons will be detected by the CEBAF Large Acceptance Spectrometer in Hall B. The restriction to a low momentum proton ensures that the electron scattering takes place on a nearly on-shell neutron. The BONUS12 experiment is scheduled to run in the spring of 2020. The neutron structure function will be measured in the DIS region up to $x \approx 0.8$ with small nuclear model uncertainties. The projected uncertainties on F_2^n/F_2^p are shown in Fig.6.2.

6.3 d/u from proton PVDIS

The SoLID collaboration at JLab Hall A aims to measure the parity-violating asymmetry (A_{PV}) with a solenoidal large intensity device (SoLID), which has a large acceptance and operates under high luminosity conditions. The parity-violating asymmetry from hydrogen is sensitive to the ratio d/u and is completely decoupled from any nuclear corrections [90]. In QCD, the asymmetry A_{PV} can be written as:

$$A_{PV} = \frac{G_F Q^2}{\sqrt{2}\pi\alpha} [a_1(x) + f(y)a_3(x)], \quad (6.4)$$

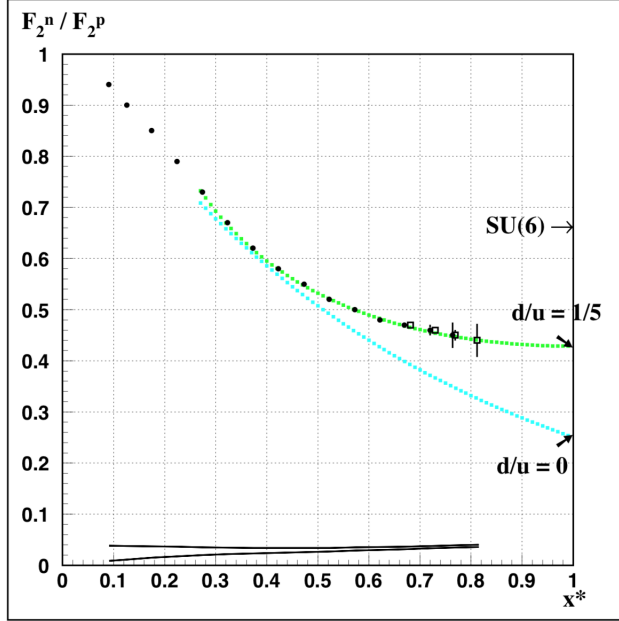


Figure 6.2: The BONUS12 projected F_2^n/F_2^p results. The filled circle points indicate the data points with $W^* > 2$ GeV with statistical uncertainties. The open squared points show the data with a loose cut $W^* > 1.8$ GeV. The black curves at the bottom indicate the estimated systematic uncertainties. The upper curve combines the experimental and theoretical uncertainties, while the lower curve represents the systematic uncertainties after normalization at low x to the world data. [92]

where $y = \nu/E$. The dominant term in the asymmetry of the proton, a_1^p , is related to the PDFs and is given by:

$$a_1^p(x) = \frac{12C_{1u}u(x) - 6C_{1d}d(x)}{4u(x) + d(x)} \quad (6.5)$$

$$\sim \frac{u(x) + 0.912d(x)}{u(x) + 0.25d(x)} \quad (6.6)$$

With PVDIS on the hydrogen target, the SoLID collaboration estimates that a 2% uncertainty on d/u can be reached over a large range of x bins, with the highest being at $x = 0.7$ after averaging.

The projected d/u results from the MARATHON experiment, the BONUS12 experiment and the SoLID PVDIS experiment are shown in Fig.6.3.

A global analysis of data from all these new experimental results will shed light on our under-

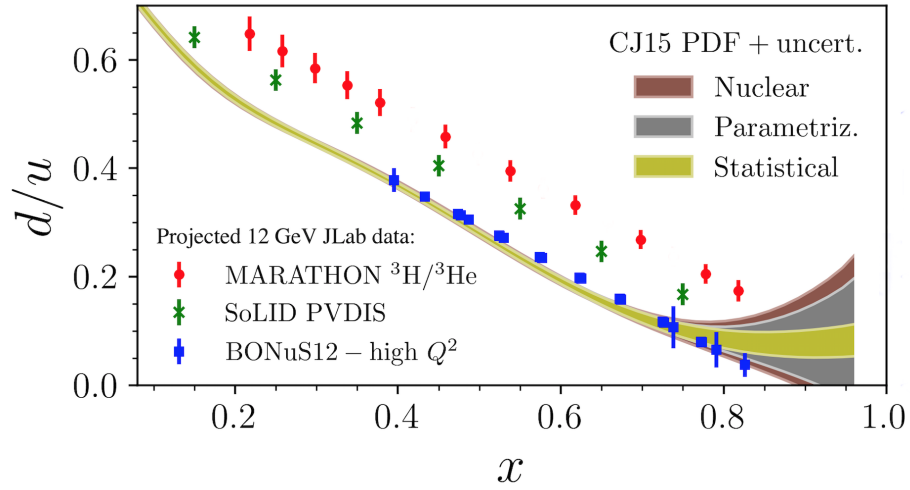


Figure 6.3: Projected d/u results from the MARATHON experiment, the BONuS12 experiment and the SoLID PVDIS experiment.

standing of the quark dynamical distributions at large x .

References

- [1] R. E. Taylor, H. W. Kendall, and J. I. Friedman. *Rev. Mod. Phys.* 63 (1991), p. 573.
- [2] E.D. Bloom *et al.* *Phys. Rev. Lett.* 23 (1969), p. 930.
- [3] G. T. Garvey *et al.* *Phys. Rept.* 580 (2015), pp. 1–45.
- [4] S. D. Drell and J. D. Walecka. *Annals of Physics* 28 (1964), pp. 18–33.
- [5] J. Kuti and V. F. Weisskopf. *Phys. Rev. D* 4 (1971), p. 3418.
- [6] R. K. Ellis, W. J. Stirling, and B. R. Webber. *QCD and Collider Physics*. Cambridge University Press, 1996.
- [7] M. Tanabashi *et al.* (Particle Data Group). *Phys. Rev. D* 98 (2018), p. 030001.
- [8] Robin Devenish and Amanda Cooper-Sarkar. *Deep Inelastic Scattering*. Oxford University Press, 2004.
- [9] Roy J. Holt and Craig D. Roberts. *Rev. Mod. Phys.* 82 (2010), p. 2991.
- [10] S. A. Kulagin and R. Petti. *Nucl. Phys. A* 765 (2006), pp. 126–187.
- [11] J. Aubert *et al.* *Phys. Lett. B* 123 (1983), p. 275.
- [12] The MARATHON collaboration. *The proposal for the MARATHON experiment*. 2010. URL: <https://hallaweb.jlab.org/collab/PAC/PAC37/C12-10-103-Tritium.pdf>.
- [13] F.E. Close. *Phys. Lett. B* 43 (1973), p. 422.
- [14] R. Carlitz. *Phys. Lett. B* 58 (1975), p. 345.
- [15] N. Isgur. *Phys. Rev. D* 59 (1999), p. 034013.
- [16] G.R. Farrar and D.R. Jackson. *Phys. Rev. L* 35 (1975), p. 1416.
- [17] S.J. Brodsky, M. Burkardt, and I. Schmidt. *Nucl. Phys. B* 441 (1995), p. 197.
- [18] U. K. Yang and A. Bodek. *Phys. Rev. L* 82 (1999), p. 2467.

- [19] A. Bodek *et al.* *Phys.Rev.* D20 (1979), pp. 1471–1552.
- [20] W. Melnitchouk and A.W. Thomas. *Phys. Lett. B* 377 (1996), p. 11.
- [21] L.W. Whitlow *et al.* *Phys. Lett. B* 282 (1992), p. 475.
- [22] J.J. Aubert *et al.* *Nucl. Phys. B* 293 (1987), p. 740.
- [23] L.L. Frankfurt and M.I. Strikman. *Phys. Rep.* 160 (1988), p. 235.
- [24] J. Arrington *et al.* *Phys. G* 36 (2009), p. 025005.
- [25] J. Arrington, J.G. Rubin, and W. Melnitchouk. *Phys. Rev. Lett* 108 (2012), p. 252001.
- [26] P.R. Norton. *Rept. Prog. Phys.* 66 (2003), p. 1253.
- [27] J. Gomez *et al.* *Phys. Rev.* D49 (1994), pp. 4348–4372.
- [28] J. Ashman *et al.* *Z. Phys. C* 57 (1993), p. 211.
- [29] A.C. Benvenuti *et al.* *Phys. Lett. B* 189 (1987), p. 483.
- [30] P. Amaudruz *et al.* *Nucl. Phys. B* 441 (1995), p. 3.
- [31] S.V. Akulinichev *et al.* *JETP Lett* 42 (1985), p. 127.
- [32] G.L. Li, K.F. Liu, and G.E. Brown. *Phys. Lett. B* 213 (1988), p. 531.
- [33] J. Seely *et al.* *Phys. Rev. Lett.* 103 (2009), p. 202301.
- [34] D.F. Geesaman, K. Saito, and A.W. Thomas. *Annu. Rev. Nucl. Part. Sci.* 45 (1995), p. 337.
- [35] L.L.Frankfurt and M.I.Strikman. *Phys. Lett. B* 183 (1987), p. 254.
- [36] C. Ciofi degli Atti and S. Liuti. *Phys. Rev. C* 41 (1990), p. 1100.
- [37] D.M. Alde *et al.* *Phys. Rev. Lett.* 64 (1990), p. 2479.
- [38] R.P. Bickerstaff and A.W. Thomas. *J. Phys. G: Nucl. Part. Phys.* 15 (1989), p. 1523.
- [39] D. de Florian *et al.* *Z. Phys. A* 350 (1994), p. 55.
- [40] R. Blankenbecler and S.J. Brodsky. *Phys. Rev. D* 10 (1974), p. 2973.
- [41] C.E. Carlson and T.J. Havens. *Phys. Rev. Lett.* 51 (1983), p. 261.

- [42] K.E. Lassila and U.P. Sukhatme. *Phys. Lett. B* 209 (1988), p. 343.
- [43] F.E. Close *et al.* *Phys. Rev. D* 31 (1985), p. 1004.
- [44] B. Schmookler *et al.* *Nature* 566 (2019), p. 354.
- [45] O. Hen *et al.* *Int. J. Mod. Phys. E* 22 (2013), p. 1330017.
- [46] L. Weinstein *et al.* *Phys. Rev. Lett* 106 (2011), p. 052301.
- [47] J. Arrington and N. Fomin. *Phys. Rev. Lett* 123 (2019), p. 042502.
- [48] A. Accardi *et al.* *Phys. Rev. D* 93.11 (2016), p. 114017.
- [49] Michael Spata. *CEBAF Overview*. 2015. URL: <https://www.jlab.org/indico/event/98/contribution/18/material/slides/0.pdf>.
- [50] C.W. Leemann, D.R. Douglas, and G.A. Krafft. *Annu. Rev. Nucl. Part. Sci.* 51:413 (2001).
- [51] J. Alcorn *et al.* *Nucl. Instrum. Meth. A* 522, 294 (2004).
- [52] Longwu Ou. “Precision Measurements of Electron-Proton Elastic Scattering Cross Sections at Large Q^2 ”. *Ph.D. Thesis, MIT* (2019).
- [53] D. Mack. *Hall A Beam Current Monitoring Infrastructure*. 2015. URL: <https://hallaweb.jlab.org/news/talks/2015/2015-07-21-Mack.pdf>.
- [54] Hall A Collaboration. *Hall A Standard Equipment Manual*. 2017. URL: <https://hallaweb.jlab.org/github/halla-osp/version/Standard-Equipment-Manual.pdf>.
- [55] P. Zhu *et al.* “Beam Position Reconstruction for the g2p Experiment in Hall A at Jefferson Lab”. *arXiv:1509.03510* (2015).
- [56] D. Meekins. *TGT-RPT-17-003: Tritium Target System Design Report*. 2017. URL: https://wiki.jlab.org/jlab_tritium_target_wiki/index.php/Reports.
- [57] D. Meekins. *TGT-CALC-17-020: Determination of solid and fluid target thickness from measurements*. 2018. URL: <https://logbooks.jlab.org/entry/3619916>.
- [58] J.J. LeRose. “Absolute Calibration of the Central Momentum”. *JLAB TN 97-042* (1997).
- [59] N. Liyanage. “Spectrometer constant determination fro the Hall A HRS pair”. *JLAB-TN-01-049* (2001).

- [60] N. Liyanage. “Optics calibration of the Hall A high resolution spectrometers using the new optimizer”. *JLAB-TN-02-012* (2002).
- [61] K.G. Fissum *et al.* *Nucl. Instr. and Meth. A* 474 (2001).
- [62] M. Iodice *et al.* *Nucl. Instr. and Meth. A* 411 (1998).
- [63] J. William Gu. *Trigger Supervisor Manual*. 2017. URL: <https://coda.jlab.org/drupal/filebrowser/download/856969>.
- [64] R. Cruz-Torres and F. Hauenstein. *Tritium DAQ Schematics*. 2018. URL: https://wiki.jlab.org/tegwiki/images/5/51/Tritium_DAQ_schematics.pdf.
- [65] S. N. *et al.* Santiesteban. *Nucl. Instrum. Meth. A* 940 (2019), pp. 351–358.
- [66] D. Meekins. *TGT-RPT-17-007: Hall A Tritium Target Configuration for December 2017*. 2017. URL: <https://logbooks.jlab.org/files/2017/12/3501699/TGT-RPT-17-007.pdf>.
- [67] L.L. Lucas and M.P. Unterweger. *Journal of Research of the National Institute of Standards and Technology* 105(4) (2000), pp. 541–549.
- [68] Aji Daniel. “Precise Measurement of the Nuclear Dependence of the EMC Effect at Large x ”. *Ph.D. Thesis, University of Houston* (2007).
- [69] L.W. Mo and Y.S. Tsai. *Rev. Mod. Phys.* 41 (1969), pp. 205–235.
- [70] Y.S. Tsai. “Radiative Corrections to Electron Scatterings”. *SLAC-PUB-848* (1971).
- [71] R. Cruz-Torres. *Beam energy and energy loss corrections*. 2018. URL: <https://wiki.jlab.org/tegwiki/images/4/43/ElossClasses.pdf>.
- [72] L.W. Whitlow. “Deep Inelastic Structure Functions from Electron Scattering on Hydrogen, Deuterium, and Iron at $0.6 \text{ GeV}^2 \leq Q^2 \leq 30.0 \text{ GeV}^2$ ”. *Ph.D. Thesis, Stanford University* (1990).
- [73] S. A. Kulagin and R. Petti. Private communication.
- [74] A. Camsonne *et al.* *Phys. Rev. Lett.* 119 (2017), p. 162501.
- [75] New Muon Collaboration (M. Arneodo *et al.*) *Phys. Lett.* B364 (1995), pp. 107–115.
- [76] A. Airapetian *et al.* *Phys. Lett.* B567 (2003), pp. 339–346.
- [77] S. Dasu *et al.* *Phys. Rev. D* 49 (1994), p. 5641.

- [78] New Muon Collaboration Collaboration (M. Arneodo *et al.*) *Nucl. Phys. B* 481 (1996), p. 23.
- [79] New Muon Collaboration Collaboration (P. Amaudruz *et al.*) *Phys. Lett. B* 294 (1992), p. 120.
- [80] HERMES Collaboration Collaboration (K. Ackerstaff *et al.*) *Phys. Lett. B* 475 (2000), p. 386.
- [81] I.R. Afnan *et al.* *Phys. Rev. C* 68 (2003), p. 035201.
- [82] Tyler Kutz. “Deep inelastic scattering from $A = 3$ nuclei: Nucleon structure and the EMC effect”. *Ph.D. Thesis, Stony Brook University* (2019).
- [83] M. Lacombe *et al.* *Phys. Lett. B* 101 (1981), p. 139.
- [84] R.V. Reid. *Ann. Phys. (NY)* 50 (1968), p. 411.
- [85] R. Machleidt, K. Holinde, and C. Elster. *Phys. Rep.* 149 (1987), p. 1.
- [86] Jason Bane. “The EMC Effect in $A=3$ Nuclei”. *Ph.D. Thesis, The University of Tennessee* (2019).
- [87] S. A. Kulagin and R. Petti. *Phys. Rev. C* 82 (2010), p. 054614.
- [88] A.J. Tropicano *et al.* *Phys. Rev. C* 99 (2019), p. 035201.
- [89] Jefferson Lab Experiment E12-06-113 [BONUS12]. *The Structure of the Free Neutron at Large x -Bjorken (PAC30)*. URL: https://www.jlab.org/exp_prog/proposals/06/PR12-06-113.pdf.
- [90] Jefferson Lab Experiment E12-10-007 [SoLID PVDIS]. *Precision Measurement of Parity-violation in Deep Inelastic Scattering Over a Broad Kinematic Range*. URL: <https://hallaweb.jlab.org/collab/PAC/PAC34/PR-09-012-pvdis.pdf>.
- [91] N. Baillie *et al.* *Phys. Rev. Lett.* 108 (2012), p. 199902.
- [92] Jefferson Lab Experiment E12-06-113 [BONUS12]. *The Structure of the Free Neutron at Large x -Bjorken (PAC36)*. URL: https://www.jlab.org/exp_prog/proposals/10/PR12-06-113-pac36.pdf.
- [93] New Muon Collaboration (P. Amaudruz *et al.*) *Nucl. Phys.* B371 (1992), pp. 3–31.
- [94] New Muon Collaboration (P. Amaudruz *et al.*) *Phys. Lett.* B295 (1992), pp. 159–168.

Appendix A: Cross Section Model Comparison

The systematic error induced by the cross section model is studied by comparing the results of cross section ratios extracted using different models. Besides the Bodek fit, the other available F_2^p and F_2^d model is from the NMC collaboration, which fits the SLAC and BCDMS DIS data, as well as NMC data [75]. The comparison between the structure functions from the two models are shown in Fig.A.1. This NMC fit does not include the resonance region, as compared to their first fit [93], while the difference resulting from neglecting the resonance is negligible everywhere except in the lowest x bin where difference approaches 2% [94]. But it is useful for comparing how the resonance will affect the MARATHON results. A global fit of $R = \sigma_L/\sigma_T$ is utilized in the NMC model to build the cross section.

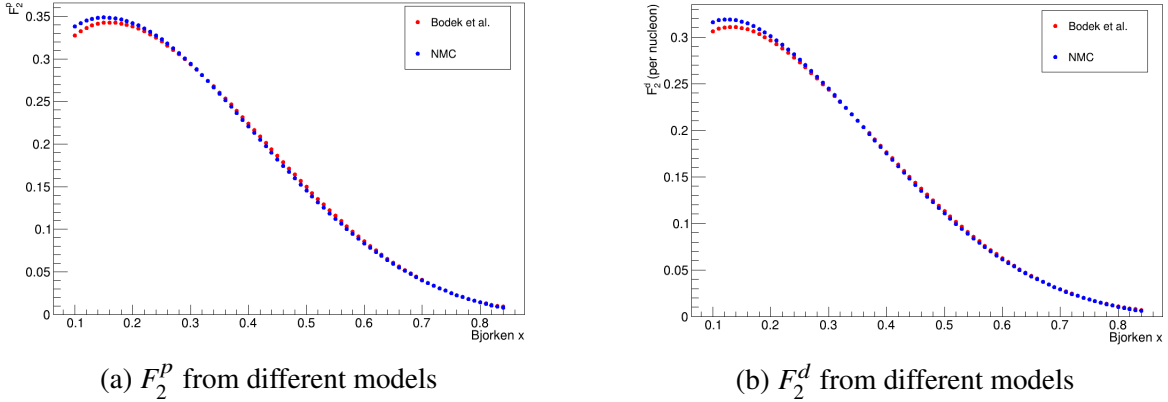


Figure A.1: F_2 Structure functions from different models

A good empirical parametrization of the EMC data by J. Gomez *et al.* [27] can also be used to build the ^3H and ^3He EMC ratio. However, the parametrization is for isoscalar nuclei. A F_2^n/F_2^p model is required to account for the differences in non-isoscalar targets. Three F_2^n/F_2^p models with different shapes are applied (see Fig.A.2). The F_2^n/F_2^p from SLAC is linear with Fermi motion taken into consideration [19]. The NMC F_2^n/F_2^p is simply equal to $(F_2^d/F_2^p - 1)$ with no nuclear

effects considered [93], which is not valid at large x ($x > 0.6$). The F_2^n/F_2^p from CJ15 [48] includes Fermi motion, binding, and nucleon off-shell effects. The resulting EMC ratios of ^3H and ^3He are shown in Fig.A.3.

Neglecting the results at large x from utilizing NMC F_2^n/F_2^p , the changes in the radiative correction factors using different models are no more than 0.35%.

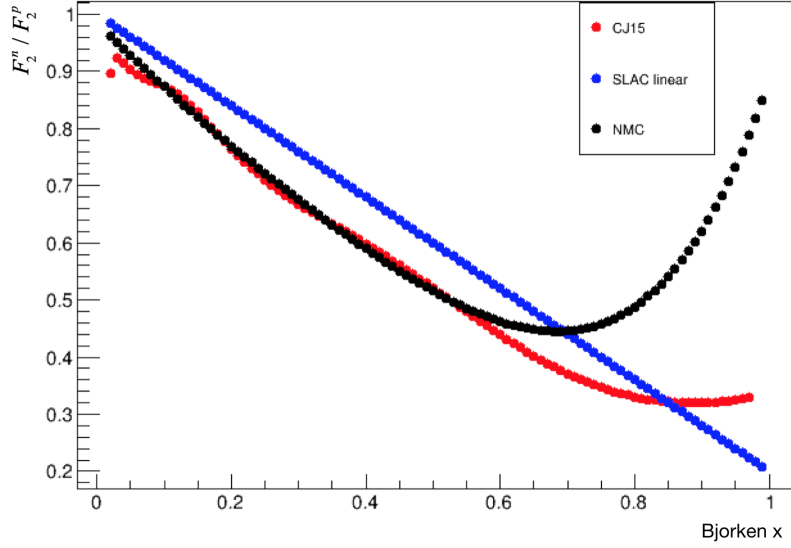
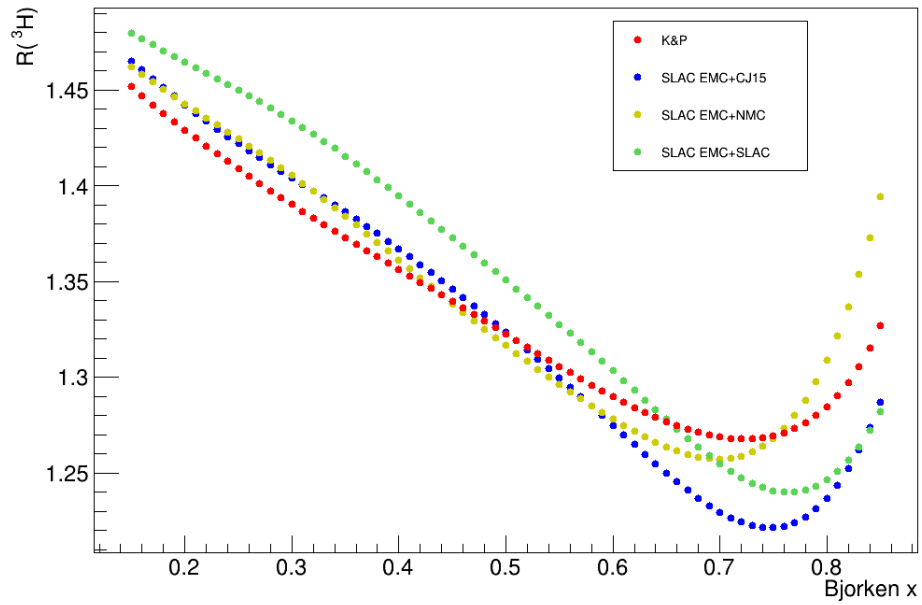
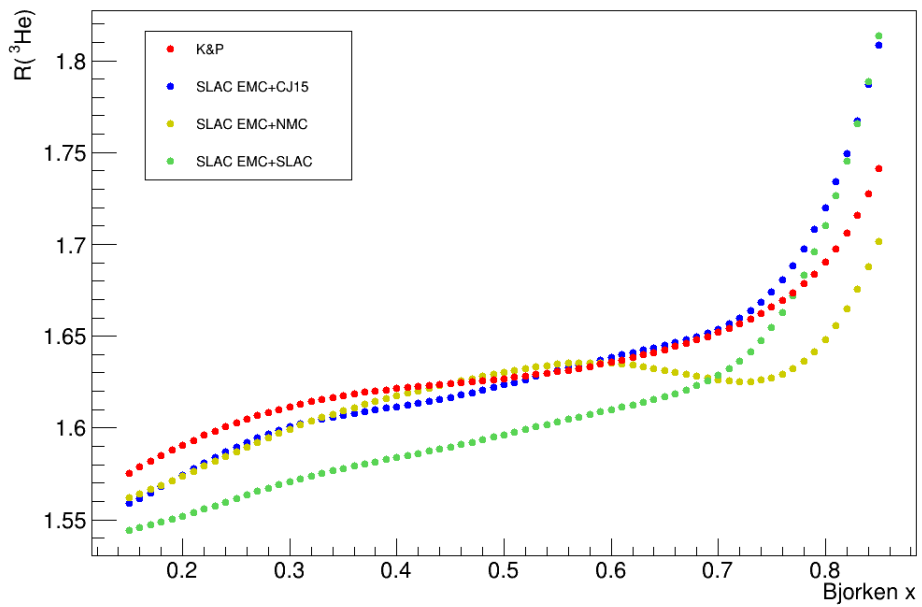


Figure A.2: F_2^n/F_2^p from different models with $Q^2 = 14x \text{ GeV}^2$ (similar to the MARATHON kinematic settings)



(a) ^3H EMC ratio from different models without isoscalar correction



(b) ^3He EMC ratio from different models without isoscalar correction

Figure A.3: EMC ratio from different models

Appendix B: Cross Section Ratio Data

The data for the cross section ratios are listed in the tables below. The tables include the relative statistical uncertainties and systematic uncertainties.

x	Q^2 (GeV ²)	$R(\frac{\sigma(^2\text{H})}{\sigma(^1\text{H})})$	$\delta R_{stat}/R$	$\delta R_{sys}/R$
0.17	2.42	1.7383	0.0039	0.0056
0.19	2.72	1.7322	0.0027	0.0053
0.22	3.10	1.7056	0.0030	0.0050
0.25	3.48	1.6774	0.0038	0.0049
0.29	4.02	1.6413	0.0038	0.0049
0.32	4.50	1.6188	0.0048	0.0053
0.34	4.91	1.5920	0.0063	0.0055
0.38	5.32	1.5290	0.0102	0.0061

Table B.1: $\sigma(^2\text{H})/\sigma(^1\text{H})$ results. The 0.79% normalization uncertainty is not shown in the table.

x	Q^2 (GeV ²)	$R(\frac{\sigma(^3\text{He})}{\sigma(^2\text{H})})$	$\delta R_{stat}/R$	$\delta R_{sys}/R$
0.17	2.42	1.5738	0.0037	0.0054
0.19	2.72	1.5662	0.0026	0.0050
0.22	3.10	1.5628	0.0028	0.0048
0.25	3.49	1.5673	0.0034	0.0047
0.29	4.01	1.5744	0.0034	0.0047
0.33	4.55	1.5625	0.0040	0.0048
0.36	5.00	1.5777	0.0061	0.0054
0.385	5.39	1.5941	0.0077	0.0054
0.43	6.02	1.5713	0.0059	0.0051
0.48	6.75	1.6179	0.0073	0.0052
0.51	7.22	1.6014	0.0078	0.0054
0.55	7.78	1.5998	0.0078	0.0052
0.59	8.32	1.5901	0.0079	0.0053
0.63	8.93	1.6024	0.0087	0.0052
0.67	9.38	1.5952	0.0100	0.0054
0.70	9.91	1.6273	0.0089	0.0052
0.74	10.50	1.6580	0.0085	0.0050
0.78	11.13	1.6530	0.0086	0.0051
0.82	11.75	1.6355	0.0115	0.0051

Table B.2: $\sigma(^3\text{He})/\sigma(^2\text{H})$ results. The 2.4% normalization on $\sigma(^3\text{He})$ is not applied.

x	Q^2 (GeV ²)	$R(\frac{\sigma(^3\text{H})}{\sigma(^2\text{H})})$	$\delta R_{stat}/R$	$\delta R_{sys}/R$
0.17	2.42	1.4758	0.0041	0.0056
0.19	2.72	1.4519	0.0028	0.0053
0.22	3.10	1.4250	0.0029	0.0051
0.25	3.50	1.4160	0.0033	0.0050
0.29	4.00	1.3991	0.0033	0.0050
0.33	4.54	1.3731	0.0039	0.0051
0.36	5.01	1.3827	0.0063	0.0056
0.385	5.39	1.3598	0.0080	0.0056
0.43	6.03	1.3298	0.0060	0.0053
0.48	6.75	1.3324	0.0076	0.0055
0.51	7.22	1.3176	0.0080	0.0056
0.55	7.78	1.3001	0.0080	0.0055
0.59	8.32	1.2835	0.0081	0.0055
0.63	8.93	1.2791	0.0090	0.0054
0.67	9.38	1.2621	0.0103	0.0056
0.70	9.91	1.2882	0.0092	0.0054
0.74	10.50	1.2856	0.0089	0.0053
0.78	11.13	1.3065	0.0089	0.0053
0.82	11.75	1.2858	0.0119	0.0054

Table B.3: $\sigma(^3\text{H})/\sigma(^2\text{H})$ results. The 1.12% normalization uncertainty is not shown in the table.

x	Q^2 (GeV ²)	$R\left(\frac{\sigma(^3\text{H})}{\sigma(^3\text{He})}\right)$	$\delta R_{stat}/R$	$\delta R_{sys}/R$
0.17	2.42	0.9377	0.0038	0.0058
0.19	2.72	0.9272	0.0026	0.0055
0.22	3.10	0.9118	0.0028	0.0054
0.25	3.48	0.9033	0.0034	0.0053
0.29	4.00	0.8876	0.0036	0.0053
0.33	4.56	0.8790	0.0042	0.0053
0.36	5.02	0.8759	0.0062	0.0057
0.385	5.40	0.8525	0.0076	0.0058
0.43	6.01	0.8456	0.0059	0.0055
0.48	6.75	0.8236	0.0075	0.0056
0.51	7.22	0.8227	0.0080	0.0058
0.55	7.78	0.8126	0.0081	0.0056
0.59	8.32	0.8068	0.0082	0.0056
0.63	8.93	0.7984	0.0091	0.0056
0.67	9.38	0.7912	0.0104	0.0058
0.70	9.91	0.7921	0.0091	0.0056
0.74	10.49	0.7750	0.0088	0.0055
0.78	11.12	0.7900	0.0088	0.0055
0.82	11.75	0.7862	0.0118	0.0055

Table B.4: $\sigma(^3\text{H})/\sigma(^3\text{He})$ results. The 2.4% normalization on $\sigma(^3\text{He})$ is not applied.

Appendix C: F_2^n/F_2^p and EMC results

The F_2^n/F_2^p extracted from tritium over helium-3 is given in Table C.1. The ^3He EMC effect result with isoscalar correction is given in Table C.2. Both results are with the 2.4% normalization applied on $F_2^{^3\text{He}}$. The ^3H EMC effect result with isoscalar correction is given in Table C.3. The discussions on the uncertainties can be found in Chapter 5. The normalization uncertainties are not included.

x	Q^2 (GeV ²)	$R(F_2^n/F_2^p)$	δR_{stat}	δR_{sys}
0.17	2.42	0.764	0.009	0.014
0.19	2.72	0.739	0.006	0.013
0.22	3.10	0.702	0.006	0.012
0.25	3.48	0.682	0.007	0.011
0.29	4.00	0.646	0.007	0.011
0.33	4.56	0.628	0.008	0.011
0.36	5.01	0.622	0.012	0.011
0.385	5.40	0.572	0.014	0.011
0.43	6.01	0.560	0.011	0.010
0.48	6.75	0.517	0.013	0.010
0.51	7.22	0.516	0.014	0.010
0.55	7.78	0.498	0.013	0.009
0.59	8.32	0.488	0.013	0.009
0.63	8.93	0.472	0.015	0.009
0.67	9.38	0.459	0.016	0.009
0.70	9.91	0.461	0.014	0.009
0.74	10.49	0.429	0.013	0.008
0.78	11.12	0.460	0.014	0.009
0.82	11.75	0.453	0.018	0.009

Table C.1: F_2^n/F_2^p results. The 2.4% normalization on $\sigma(^3\text{He})$ is applied.

x	Q^2 (GeV ²)	R	δR_{stat}	δR_{sys}
0.17	2.42	1.028	0.004	0.006
0.19	2.72	1.018	0.003	0.006
0.22	3.10	1.008	0.003	0.006
0.25	3.49	1.006	0.004	0.005
0.29	4.01	1.003	0.004	0.005
0.33	4.55	0.991	0.004	0.005
0.36	5.00	0.999	0.007	0.006
0.385	5.39	0.997	0.008	0.006
0.43	6.02	0.980	0.006	0.006
0.48	6.75	0.998	0.008	0.006
0.51	7.22	0.988	0.008	0.006
0.55	7.78	0.982	0.008	0.006
0.59	8.32	0.973	0.008	0.006
0.63	8.93	0.977	0.009	0.006
0.67	9.38	0.969	0.011	0.006
0.70	9.91	0.989	0.010	0.006
0.74	10.50	0.999	0.009	0.006
0.78	11.13	1.004	0.009	0.006
0.82	11.75	0.992	0.013	0.006

Table C.2: The EMC ratio for ³He results with isoscalar correction. The 2.4% normalization on $\sigma(^3\text{He})$ is applied.

x	Q^2 (GeV ²)	R	δR_{stat}	δR_{sys}
0.17	2.42	1.030	0.005	0.007
0.19	2.72	1.019	0.003	0.006
0.22	3.10	1.009	0.003	0.006
0.25	3.50	1.008	0.004	0.006
0.29	4.00	1.005	0.004	0.006
0.33	4.54	0.991	0.004	0.006
0.36	5.00	1.000	0.007	0.006
0.385	5.39	0.997	0.009	0.006
0.43	6.03	0.979	0.007	0.006
0.48	6.75	0.994	0.009	0.006
0.51	7.22	0.984	0.009	0.006
0.55	7.78	0.976	0.009	0.006
0.59	8.32	0.967	0.009	0.006
0.63	8.93	0.969	0.010	0.006
0.67	9.38	0.960	0.011	0.006
0.70	9.91	0.979	0.010	0.006
0.74	10.50	0.989	0.010	0.006
0.78	11.13	0.994	0.010	0.006
0.82	11.75	0.981	0.013	0.006

Table C.3: The EMC ratio for ³H results with isoscalar correction. The 1.12% normalization uncertainty of $\sigma(^3\text{H})/\sigma(^2\text{H})$ is not included.